DISSERTATION

QUANTUM EFFICIENCY AS A DEVICE-PHYSICS INTERPRETATION TOOL FOR THIN-FILM SOLAR CELLS

Submitted by

Timothy J. Nagle

Department of Physics

In partial fulfillment of the requirements
for the Degree of Doctor of Philosophy
Colorado State University
Fort Collins, Colorado
Fall 2007

COLORADO STATE UNIVERSITY

September 14, 2007

WE HEREBY RECOMMEND THAT THE DISSERTATION PREPARED UNDER OUR SUPERVISION BY TIMOTHY J. NAGLE ENTITLED QUANTUM EFFICIENCY AS A DEVICE-PHYSICS INTERPRETATION TOOL FOR THIN-FILM SOLAR CELLS BE ACCEPTED AS FULFILLING IN PART REQUIREMENTS FOR THE DEGREE OF DOCTOR OF PHILOSOPHY.

Graduate Committee

Stuart Field

Advisor James R. Sites

Department Head Raymond A. Robinson

ABSTRACT OF DISSERTATION

QUANTUM EFFICIENCY AS A DEVICE-PHYSICS INTERPRETATION TOOL FOR THIN-FILM SOLAR CELLS

Thin-film solar cells made from CdTe and $CuIn_{1-x}Ga_xSe_2$ p-type absorbers are promising candidates for generating pollution-free electricity. These devices have band gaps which are well-suited for absorption of sunlight. Most importantly, the materials used in these devices can be deposited in a variety of industry-friendly ways, so that the cost associated with manufacturing is generally lower than for competing technologies such as crystalline silicon. The challenge faced by the thin-film photovoltaics (PV) community is to improve the electrical properties of devices, without straying from low-cost techniques that are amenable to industry. This dissertation will focus on the use of quantum-efficiency (QE) measurements to deduce the device physics of thin-film devices, in the hope of improving electrical properties—and efficiencies—of PV materials.

While photons are the source of the energy required for creating electron-hole pairs which produce PV power, photons can also have secondary effects, such as modifying the band structure of the solar cell. Under illumination, photoconductivity in the commonly-used CdS window layer can result in band profiles which differ from those present in the dark. By investigating the effect of bias light during QE measurements, one can determine whether photoconductivity plays a role in device operation, in which case QE measurements performed under non-standard conditions may be in error. QE data is presented here which was taken under a variety of light-bias conditions, from dark to 0.40 sun intensity. These results suggest that in most cases, 0.10 sun of white-light bias incident on the CdS layer is sufficient to achieve accurate results. Effects are observed in the short-wavelength region and the near-bandgap region if no conduction-band offset is present. If

a large conduction-band offset results in an electron energy barrier, effects are observed throughout the entire spectrum.

QE results can be described by simple models which are based on carrier collection by drift and diffusion, and photon absorption. These models are sensitive to input parameters such as carrier mobility and lifetime, which are difficult to measure directly. One model, referred to as the "Simple-drift model", accurately predicts QE results in the thin-film devices studied. By comparing calculated QE curves with experimental results, it was determined that minority-carrier (electron) lifetimes in CdTe are the order of 0.01–0.1 ns. Lifetime determinations for CdTe devices with varying amounts of copper in the back-contact show that increasing amounts of copper correlates with shorter electron lifetimes. This supports the hypothesis that copper serves as a recombination center in CdTe.

The spatial uniformity of QE results has been investigated with the LBIC apparatus, and several individual experiments are described which investigate the effect of device processing conditions on cell uniformity. Virtually every electrical variation that can occur in a solar cell can occur in a nonuniform fashion, and can often be detected with the LBIC apparatus. LBIC was used to directly show that the presence of copper reduces photocurrent, likely due to Cu serving as a recombination center in CdTe. Additionally, the use of a highly-resistive TCO layer is demonstrated to improve cell uniformity, due to mitigating shunt-paths and weak diodes. Optical effects are shown to be a cause of nonuniformity in non-thin-film devices, but are not usually dominant in thin-film devices. Forward biased LBIC measurements indicate that conduction-band barriers which cause voltage-dependent collection in some CIGS devices are spatially nonuniform.

Devices with transparent back contacts have been suggested by others as a novel device structure for thin-film PV devices. Light-beam-induced current (LBIC) results on ITO back-contact devices show that with front illumination, a significant portion of long-wavelength photons are reflected back into the device from the ITO/air interface, improving long-wavelength QE. CdTe devices which received different back contact surface treatments were studied; including those that received a strong bromine/dichrol/hydrazine

(BDH) etch and those that received a weak bromine in methanol etch. While front-side LBIC showed similar uniformity, back-side results showed improved uniformity in BDH-etched devices, attributed to better (more ohmic) back contacts in these devices. In thin-absorber devices, the uniformity trend would likely extend to front-side measurements as well.

Timothy J. Nagle
Department of Physics
Colorado State University
Fort Collins, CO 80523
Fall 2007

Acknowledgements

> "If I have seen farther than others, it is because I was standing on the shoulders of giants."
>
> -Isaac Newton

This work would not have been possible without the help and encouragement of friends, family, and colleagues.

First, I want to thank my parents who have supported and encouraged me in whatever I have chosen to do. My mother never let me get away with giving less than my best, and never, *ever* let me get away with not doing my homework. My father encouraged me to ask questions and sparked my interest in science, and taught me the inner workings of any mechanical or electrical device we could take apart. With such a combination of role-models, I was well-prepared for graduate school in physics.

Thanks to my advisor Jim, whose advice and expertise is always appreciated. I am indebted to my colleagues in the CSU Photovoltaic Laboratory, past and present, including Pam Johnson, Alex Pudov, Markus Gloeckler, Caroline Corwine, Sam Demtsu, Ana Kanevce, Jun Pan, Alan Davies, Galym Koishiyev, and Lei Chen. I have learned much more about photovoltaics during conversations with my peers than I have from any textbook, and I have you to thank.

I am grateful to my committee members: Professors Stuart Field, Marty Gelfand and Kevin Lear for reviewing this manuscript.

This work was made possible by helpful collaborations with several researchers including Brian McCandless at IEC, Tim Gessert at NREL, Scott Feldman at CSM, Alan Fahrenbruch, and the research group of W. S. Sampath in the department of Mechanical Engineering at CSU. This research was funded through the NREL thin-film partnership program.

Thanks also, to friends outside the lab for fun times including (in no particular order): Kevin, Rob, Margo, Erica, Tony, “the other Tim”, Rebecca, Heidi, and Dennis.

Finally, thank you to Katie, whose love and support was most valuable. Thank you for your unconditional support, and for helping me to work when it was time to work and to relax when it was time to rest. I could not have done this without you.

Contents

List of Figures

List of Tables

Chapter 1

Motivation

1.1 The Energy Supply in Context

One of the most important ingredients for continued human progress is an ample supply of energy. It is sensible, then, to concern ourselves with the sources of this energy. At present, approximately 40% of the world's energy comes from oil. Natural gas and coal each account for roughly one-quarter of the world's energy supply. The remaining energy is supplied by wood, nuclear fission, and hydroelectric, in that order. At this time, renewable sources account for an inconsequential portion of the world's energy supply [1].

If we examine only the electricity supply in the United States (and ignore the oil-dominated transportation sector), renewable sources still make up an inconsequential portion of our supply. About 55% of our on-grid electricity comes from coal-burning power plants. The renewable forms biomass, wind, and photovoltaics (PV) combined account for less than 0.1% of the US electricity supply [2].

Despite this reliance on fossil fuels, the world will not run out of energy during this author's lifetime or soon thereafter. At the present rate of consumption, we have at least 500 years' worth of coal left to burn, if we choose to do so [3]. Another ample energy source is nuclear power through fission, although governments are persistently reluctant to commission new nuclear reactors in light of concerns about waste storage and terrorism.

At first glance then, it seems that the world is not experiencing an energy *crisis*. We can change nothing about our habits and continue to power our society at the present burn rate of 13 TW for hundreds of years. Even with the expected global energy consumption rate of $\sim$ 30 TW by the year 2050, problems of energy supply will not appear for several generations [4]. From purely a supply perspective, perhaps the perceived energy crisis might be best left to future generations (with future generations' technology) to solve. When environmental concerns are considered, however, "crisis" is an apt description of our current situation.

1.2 Energy Choices and the Environment

As shown in Section 1.1, the world has ample supplies of fossil fuels to continue for ten generations at current rates of energy use. The truly pressing concern for energy policy-makers should be the environmental effects of fossil-fuel use.

The Great Smoky Mountains National Park is a striking example of the effects of air pollution. The park, in Tennessee and North Carolina, suffers from the effects of distant coal-burning power plants and automobile emissions, and the result is air quality similar to that of Los Angeles, CA [5]. Fossil fuel burning also detracts from public health by contributing to ground-level ozone which has been found to significantly increase the risk of premature death [6]. These quality-of-life concerns, however, pale in comparison to the drastic damage greenhouse gases do to our environment.

Seemingly every new day brings news of another scientific study with evidence that global warming is occurring and human activities are to blame. Figure 1.1—the so-called "Hockey-stick Graph"—gives a striking picture of the link between global temperature and carbon dioxide. The same trend is observed in data going back 420,000 years [8]. While it is difficult to say with absolute certainty whether increased CO_2 has *caused* the warming or *vice-versa*, the prudent approach to the data is to reduce our impact on our environment.

The scientific community is largely in agreement that greenhouse gas emissions are the

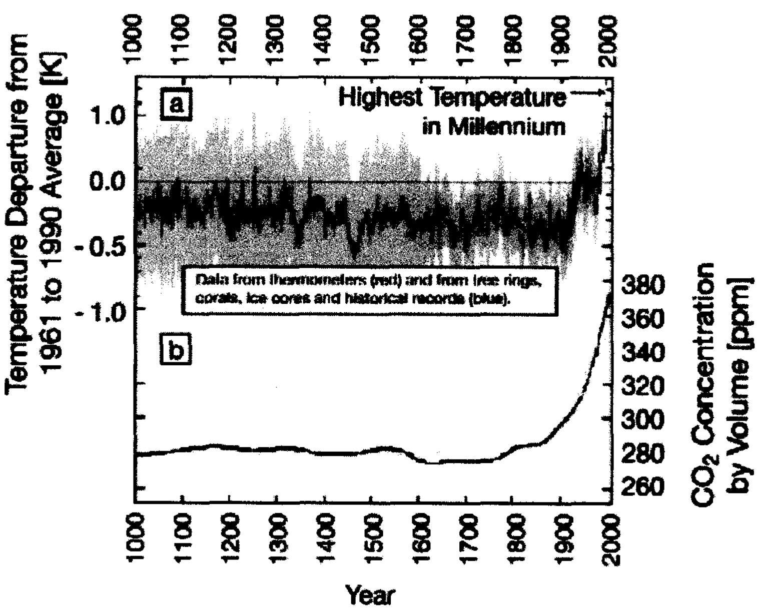

Figure 1.1: Correlation between global temperature and atmospheric CO_2. Temperature data from thermometers (recent) and tree rings, corals, ice cores and historical records. CO_2 data from Mauna Loa Observatory (recent) and ice core records. [Figure reproduced from [7]]

most probable cause of the warming [9], that the damage to the environment is irreversible on a timescale of hundreds of years [10], and that reducing CO_2 emissions should be a priority [11]. A careful survey of energy sources by Nathan Lewis reveals that *only* solar energy has a large enough resource base to meet the world's energy demands without contributing greenhouse gases to the atmosphere [4].

1.3 The Case for Thin-film Solar

With the exception of nuclear fission energy and geothermal energy, all the energy we use today at one time took the form of photons from the sun. Some of this energy evaporated water, which collects as rain in elevated reservoirs for us to exploit for hydroelectricity. Some of the solar energy conspires with local geography to cause uneven heating at the earth's surface, and we exploit the resulting air pressure differences with wind turbines.

Much of the solar energy is absorbed by plants to synthesize glucose ($C_6H_{12}O_6$) from CO_2 and H_2O, and to assemble the carbon-rich organisms on earth directly (plants) or indirectly (animals) [12]. The long-deceased carbon-rich organisms that make up the fossil fuel resource base are just a convenient storage bank for the earth's accumulated solar energy. Unfortunately, withdrawals from the storage bank require unraveling the carbon chains and re-releasing the CO_2 and H_2O. Fermentation of glucose into ethanol in fast-growing crops such as switchgrass or corn could in principle be "carbon-neutral" if the amount of CO_2 released by the combustion of ethanol from this year's crop is recaptured by next year's crop. If biofuels are to be part of the solution to the problem of increasing CO_2, then they must be utilized in this sustainable fashion. The ubiquity of solar energy in the chain of energy sources is a message that suggests that it is a good strategy to explore direct conversion of solar energy to electricity rather than rely on intermediate processes of photosynthesis and the water cycle.

Like virtually any technology, the use of photovoltaics for a substantial portion of grid-connected electricity generation has both advantages and drawbacks. Some of the advantages are obvious such as: (1) a nearly pollution-free energy source, (2) decentralized power generation that should be less vulnerable to catastrophic accident or sabotage, and (3) low-maintenance power plants with inexhaustible fuel supplies. The most obvious drawbacks are that the energy supply is intermittent (the sun does not shine at night), and that *at present* the cost of solar electricity is several times that of conventional power. The former could be addressed through storage batteries or a worldwide electricity grid, although some backup supply would probably remain necessary under all but the most optimistic scenarios. The latter is addressable by further research and development, and by the economies of scale that have made products like cellular telephones and personal computers cheap and ubiquitous.

The modern solar cell was first realized at Bell Laboratories in 1954 in the form of a 6%-efficient crystalline-silicon (c-Si) device [13], although a 1%-efficient device had been patented more than ten years earlier and the photovoltaic effect had been observed more

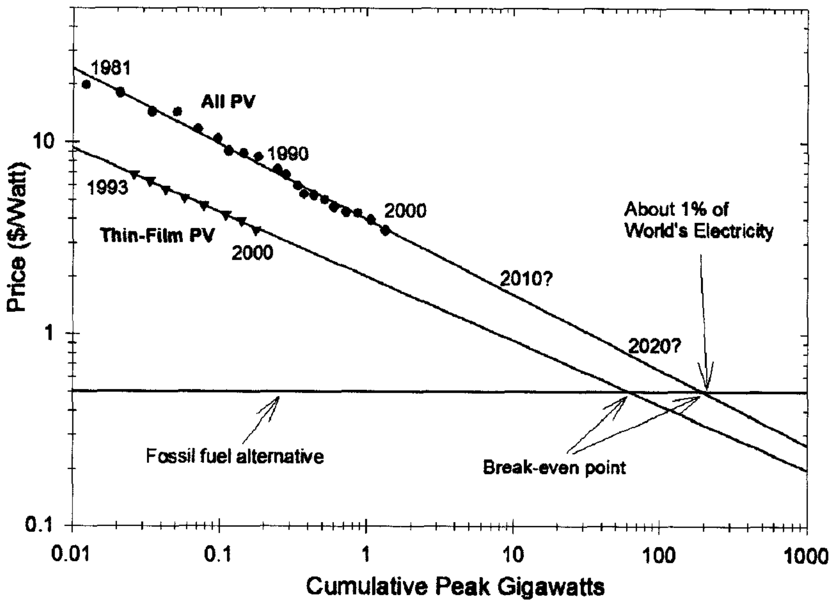

Figure 1.2: Learning curves for photovoltaics suggest that thin-film devices may become price-competitive sooner that their c-Si counterparts. [Data reproduced from [15]]

than 100 years before the patent. To this day, production of c-Si photovoltaics dominates over thin films (CdTe, Cu(In,Ga)Se_2, and amorphous silicon) worldwide, because crystalline silicon devices are well-understood and the manufacturing process is mature. In the US, however, thin-film solar cell production has now surpassed that of crystalline silicon. Recent studies suggest that thin films are also likely to dominate the worldwide terrestrial market in the near future, since they should be capable of reaching a lower price figure (in $/Watt) as our understanding of thin-film device physics improves [14, 15]. An examination of the learning curve for photovoltaics shows that although thin films are much less mature than the rest of the photovoltaics industry in terms of cumulative production, they achieved a $/W figure similar to that of c-Si a few years ago (see Figure 1.2). The manufacturing cost of CdTe PV panels (CIGS panels are not yet in large-scale production) is reputed to be a factor of two below the market price.

The basis for thin-film solar reaching a lower $/Watt figure comes from a few inherent advantages of thin films with respect to c-Si. Thin-film cells are typically 100 times thinner than silicon cells, since large thicknesses of c-Si must be used to absorb solar photons. Thinner devices need less raw materials, and also can tolerate lower-quality raw material since charge carriers only travel short distances in the semiconductor before collection by metallic contacts. Silicon devices rely on the silicon wafer itself for rigidity, while thin-film devices are typically deposited on low-cost substrates such as glass or foil. The large amount of high-quality silicon feedstock necessary for c-Si PV is expected to set a lower limit on module price at a level too high to compete with fossil fuel generated electricity [16]. Most c-Si approaches also require a labor-intensive module-assembly step, during which individual wafers are connected in series. Throughput for thin-film manufacturing can be very large with in-line processing, where continuous deposition and monolithic module interconnections turn glass and raw materials into a completed module [17]. With smart engineering, a factory can turn a plain piece of glass into a completed thin-film PV module in only a few hours, with minimal involvement of human hands [18].

Worries about the capability of solar power to meet the energy demands of society are unfounded. A careful comparison of the energy capacity of all known US domestic oil reserves with the realistic potential of solar power over the next 70 years reveals that these resources are of approximately equivalent size [19]. It is estimated that 10,000 square miles of land area would be required for solar power to meet the nation's electricity needs. This is a large area, but it is much smaller than the land-area that is currently covered with streets and highways [20]. This suggests that the land-area requirement is neither an unreasonable strain on our technological capabilities nor on the tolerance of the public.

1.4 Contributions of This Work

This dissertation contributes to the goal of widespread, economical use of solar power by investigating light-absorption and carrier collection in thin-film PV devices. The interpretation of quantum-efficiency measurements to reveal solar cell device physics will be investigated in depth. Chapter 2 discusses the device physics of solar cells, and offers a background on the particular technologies discussed in later chapters. Chapter 3 investigates the role of light bias in accurate measurements of device quantum efficiency. In Chapter 4, various models for collection of charge carriers are presented and compared, and used to determine the effect of lifetime on quantum efficiency. In Chapter 5, spatially nonuniform collection will be considered, and the use of the LBIC apparatus to identify device physics will be discussed. Finally, the important conclusions of this work will be summarized in Chapter 6.

Chapter 2

Background

2.1 Solar Cell Operation

2.1.1 Device Physics

A solar-cell is a p-n junction, transparent on one side, that is engineered for efficient separation and collection of charge carriers. In an n-type semiconductor, there exists a concentration of electrons which are only weakly associated with an ion core. At room temperature, these electrons are essentially free carriers. In a p-type semiconductor a similar argument holds true, although in this case it is a hole—the absence of an electron—which can be treated as a free charge carrier at room temperature. Neither the n- or p-type material need have any net charge. When the n-type material and p-type material are brought into contact, the free electrons diffuse towards the p-side because of the concentration gradient and recombine with the free holes, which diffuse in the opposite direction. Since the formerly neutral n-type material has lost those electrons which diffused away, it is said to have positive space-charge due to the remaining ion cores, and the p-type side is said to have negative space charge.

The positive space charge on the n-type side must be equal in magnitude to the negative space-charge on the p-type side. The adjacent positive and negative space-charge cause an electric field which tends to resist additional diffusion of electrons (or holes) towards the p-side (or n-side). This electric field is called the built-in electric field, and the potential difference between the front and back of the device is called the built-in voltage (V_{bi}). Within the space charge region, if an electron-hole pair is generated, the electric field sweeps the electron towards the n-side of the junction and the hole towards the p-side of the junction. It is this phenomenon that we exploit to extract power from incident sunlight.

In a one-sided junction, such as is typical in thin-film solar cells, the space-charge volume is much greater on the more weakly-doped side, which for the purposes discussed here will be the p-side. The p-type material has a bandgap tuned to absorb most solar radiation (for this reason, we call it the absorber layer—see Figure 2.1), so by design most electron-hole-pair generation occurs in this layer. The photogenerated electrons and holes are immediately swept in opposite directions. After charge separation, the electron finds itself in a heavily n-type material. In the n-type material there are very few holes with which to recombine, and the electrons can be collected by the front electrode. A similar argument holds for photogenerated holes which exit the device through the back-contact electrode.

If the photogenerated electron completes its journey to the front electrode, *and* the hole completes its journey to the back electrode, then 1.602×10^{-19} coulombs would pass through the circuit between the front and back electrodes. For a constant flux of photons, due for example to Air-Mass 1.5 illumination (AM1.5), a constant flux of charge would pass through the short circuit, and an ammeter in series with the device would measure I_{SC}, the short-circuit current. By convention, $I_{SC} < 0$ for a device under illumination, since if we forward-bias the diode, electrons move from front to back within the device—that is, opposite the direction of photocurrent. The short-circuit current is approximately linear with photon flux. The usual parameter used to describe photocurrent is short-circuit current density J_{SC}, measured in mA/cm^2.

If the external circuit is disconnected on an illuminated device, we can speak of electrons "piling up" at the front electrode and holes "piling up" at the back electrode. As

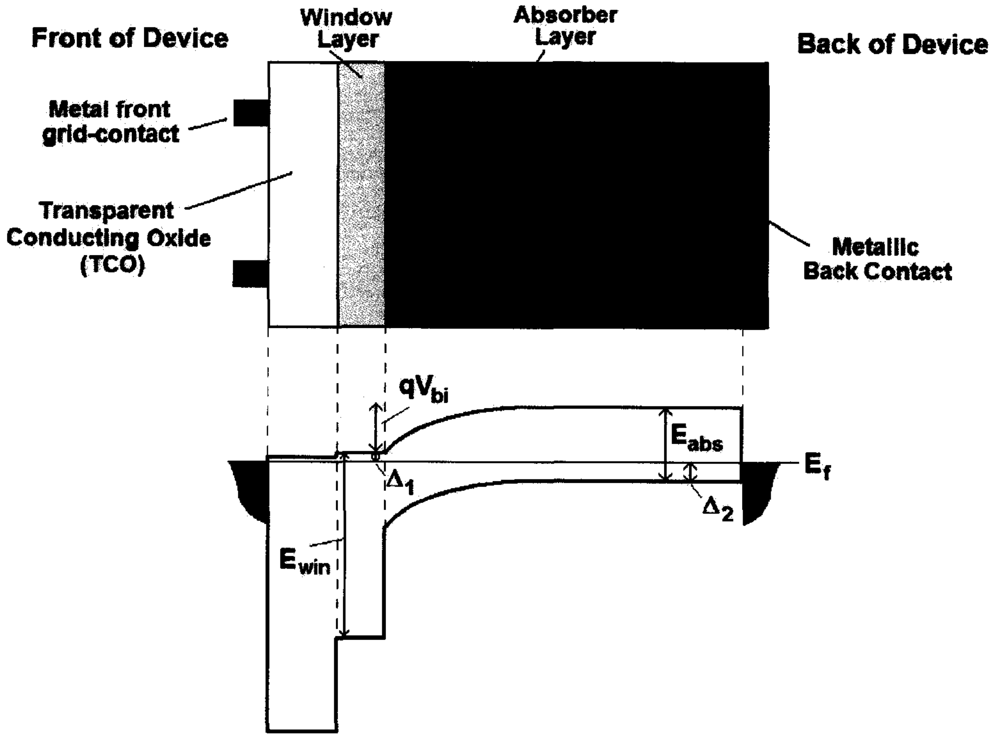

Figure 2.1: A schematic diagram of solar cell layers (top), and an energy band diagram for the same device (bottom). Some layers are common to nearly all thin-film devices, including a heavily n-type TCO, n-type CdS window layer and a metallic back contact. Since the semiconductor layers can be very thin (< 10 μm) the layers are usually deposited on a rigid substrate, which can be either at the front or the back of the device. The energy band diagram shows typical band alignments and denotes V_{bi}, E_f, and E_g in the window and absorber layers. V_{bi} is less than E_g/q by $(\Delta_1 + \Delta_2)/q$, which depends on carrier concentrations in the n- and p-type materials.

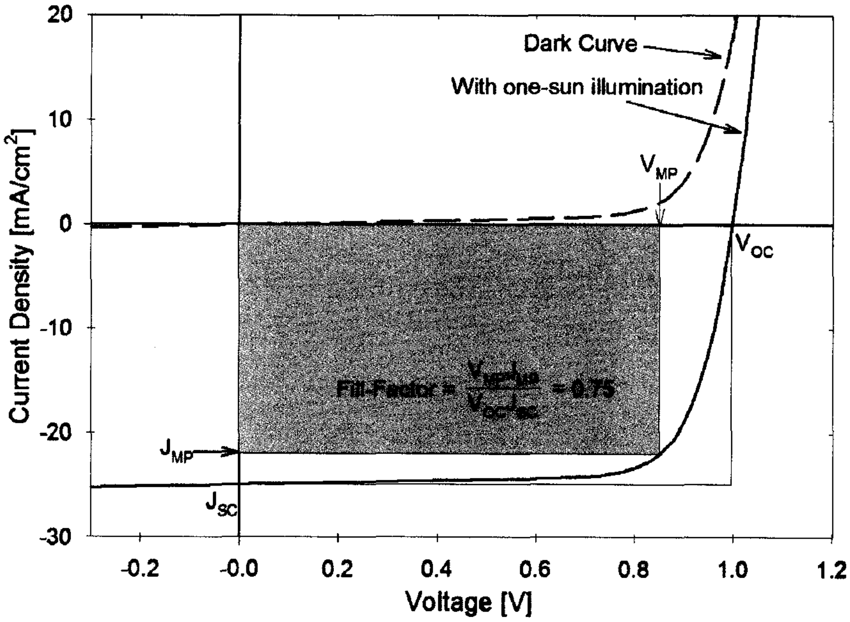

Figure 2.2: Simulated current-voltage curves for a hypothetical device in the dark (dashed) and under one-sun illumination (solid). The photovoltaic parameters J_{SC} and V_{OC}, as well as a graphical representation of the fill-factor are also shown.

charge accumulates at the front and back, the built-in field is canceled and electron-hole pairs are no longer swept away. If we connect a voltmeter to the device, we measure the voltage generated by the accumulation of charge at the front and back. This voltage is called the open-circuit voltage, V_{OC}. The open-circuit voltage is somewhat less than the built-in voltage of the diode V_{bi}, the curvature in the bands shown in Figure 2.1. V_{bi} itself is somewhat less than E_g/q, where E_g is the absorber bandgap, although increasing E_g does in general increase V_{bi} and V_{OC}.

Although device operation at J_{SC} and V_{OC} is instructive, a solar cell is not intended to be operated at either of these points. At J_{SC}, $V = 0$ since the device is short circuited, so $P = I \times V = 0$. At V_{OC}, $P = 0$ since $J = 0$, so at neither of these points has any of the sun's power been converted into electricity. If the load on the illuminated device is varied from $R = 0$ (short circuit) to $R = \infty$ (open circuit), a curve of current density vs. voltage (J-V) is traced in the fourth quadrant as shown in Figure 2.2. The parameters J_{SC} and V_{OC} are shown where the solid curve crosses the horizontal and vertical axes. The voltage at which the power is maximum is the maximum-power voltage, V_{MP}, and the corresponding current density is J_{MP}. The fill-factor (FF) is the ratio of the maximum power (MP) to the product of open-circuit voltage V_{OC} and short-circuit current J_{SC},

$$FF = \frac{V_{MP} \cdot J_{MP}}{V_{OC} \cdot J_{SC}}. \tag{2.1}$$

The fill-factor is best thought of as the "squareness" of the J-V curve. The illuminated curve in Figure 2.2 has a fill factor of 75%, a V_{OC} of 1.0 V, and a J_{SC} of 25 mA/cm^2. Graphically, the fill-factor is the ratio of the area of the shaded rectangle in Figure 2.2 to the outer, unshaded rectangle. The efficiency (η) of a device is defined as

$$\eta = \frac{P_{out}}{P_{in}} = \frac{V_{OC} \cdot J_{SC} \cdot FF}{P_{in}}. \tag{2.2}$$

Shown in Figure 2.3 is the output power and illuminated J-V curve of the generic device of Figure 2.2. Since the input power density is 100 mW/cm^2, the efficiency of this device is 19%. It follows from Equation 2.2 that by increasing any one of J_{SC}, V_{OC}, or FF independently of the other two, we can increase the efficiency of the device. This is an important point to keep in mind as various strategies for improving device structures are considered in this dissertation.

The shape of the J-V curve comes from the exponential nature of the Shockley equation—in its simplest form:

$$J = J_0(e^{\frac{qV}{kT}} - 1). \tag{2.3}$$

Here, J_0 is the reverse saturation current, V is the applied voltage and J is the current density. The Shockley equation relies on an assumption that no recombination occurs in the space-charge region. If this assumption is false and the forward current is in fact dominated by the recombination current rather than thermionic emission, the forward current will have a somewhat weaker voltage dependence $J \propto (e^{\frac{qV}{2kT}} - 1)$. When forward current is a combination of thermionic emission current and recombination current, the forward current

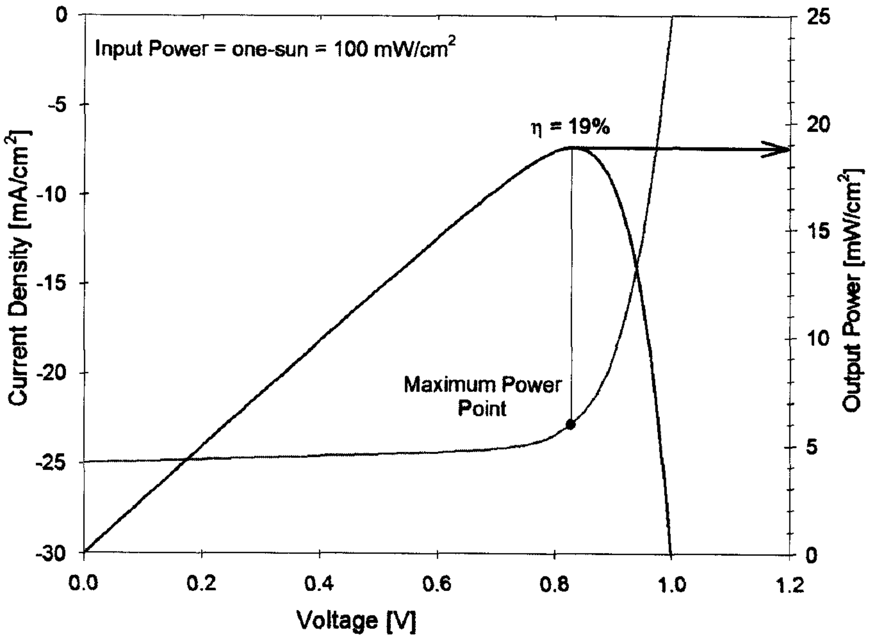

Figure 2.3: The light J-V curve is the same as that shown in Figure 2.2. The output power, as determined by $\mathbf{P} = \mathbf{I} \cdot \mathbf{V}$ is plotted on the right-hand axis. This device has $\eta = 19\%$.

takes on the empirical form

$$J = J_0(e^{\frac{qV}{AkT}} - 1), \tag{2.4}$$

where A is known as the diode-quality factor ($1 < A < 2$, usually). The empirical value of A suggests whether the dominant forward-current mechanism is thermionic emission or recombination current [21].

Under illumination, the current density is shifted downwards by the light-generated current J_L (usually J_L=J_{SC}),

$$J = (J_0(e^{\frac{qV}{AkT}} - 1)) - J_L. \tag{2.5}$$

Additional corrections to this simplified diode equation are discussed in Section 2.2.1.

2.2 Experimental Techniques

The following techniques were used to characterize and compare the different thin-film devices discussed in this dissertation.

2.2.1 Current-Voltage

Measurement of the J-V curve is the most basic way to characterize a solar cell. In addition to η, an accurate J-V measurement yields J_0 and A, as defined in Section 2.1.1. A real-world device has an associated series resistance R_S due to layer and contact resistances, and shunt resistance r_{sh} usually due to small shunt paths through or around device layers. The effect of the shunt and series resistances on the diode equation are a reduction of the applied voltage by the quantity JR_S, and a reduction of the measured current by an amount V'/r_{sh} where $V' = V - JR_S$ is the actual junction voltage (rather than the applied voltage). With these corrections, Equation 2.5 becomes

$$J = J_0(e^{\frac{q(V-JR_S)}{kT}} - 1) + \frac{V - JR_S}{r_{sh}} - J_L. \tag{2.6}$$

Standard current-voltage curves are measured at 25 °C in the dark and under one-sun illumination. Under illumination, active cooling with cold N_2 gas is used to maintain 25 ± 1°C, since without cooling the device temperature would increase by approximately 10°C during a sixty-second measurement. The use of cold N_2 gas allows data to be taken in the temperature range of -45 to $+45$°C, a useful range for extracting barrier heights in the device band structure. Data is routinely taken starting at -0.5 V in small voltage-steps (0.02 V) until the current density reaches 60–80 mA/cm^2 in the first quadrant. It is possible to take data at more-negative voltages without damaging most devices (as low as -2.0 V), but there is little additional information to be gained from measurements at these voltages. Current is electronically limited to protect the device from excess forward currents.

The schematic diagram for a J-V measurement is shown in Figure 2.4. A four-point Kelvin-probe contact scheme is used to minimize the effects of contact resistances. A pro-

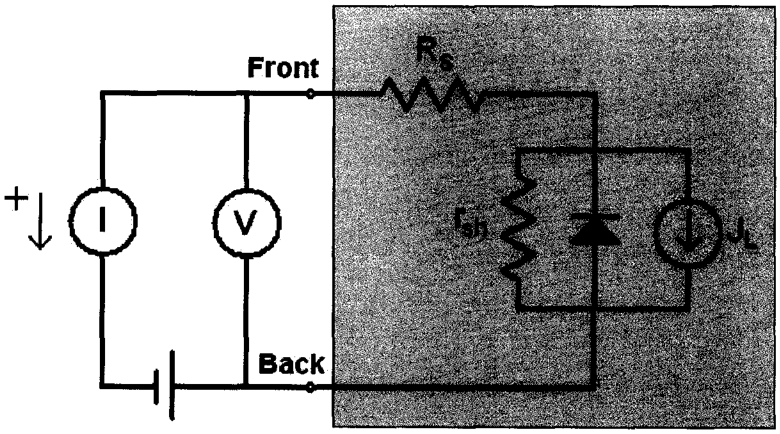

Figure 2.4: Schematic diagram for J-V measurement. The shaded region is internal to the device.

grammable power supply (Keithley 230) is connected in series with an ammeter (HP 34401A). The device is also connected in parallel with a voltmeter (HP 34401A). The current-voltage experiment is computer-controlled with LabVIEW software. Typical J-V data is shown in Figure 2.5.

2.2.2 Quantum Efficiency

Quantum-efficiency measurements (QE) quantify the spectral response of a device. The photocurrent response to a monochromatic probe beam is measured, with QE defined as

$$QE(\lambda) = \frac{\#\ of\ electrons\ collected}{\#\ of\ incident\ photons}. \tag{2.7}$$

If QE is obtained under true J_{SC} conditions (AM1.5 illumination, $V = 0$), then QE measurements can be related to the photovoltaic parameter J_{SC} by

$$J_{SC} = q \int \Phi_{AM1.5}(\lambda) QE(\lambda) d\lambda, \tag{2.8}$$

where $\Phi_{AM1.5}$ is the photon flux of AM1.5 illumination. It is usually impractical to perform QE measurements under true J_{SC} conditions, and fortunately Equation 2.8 generally holds

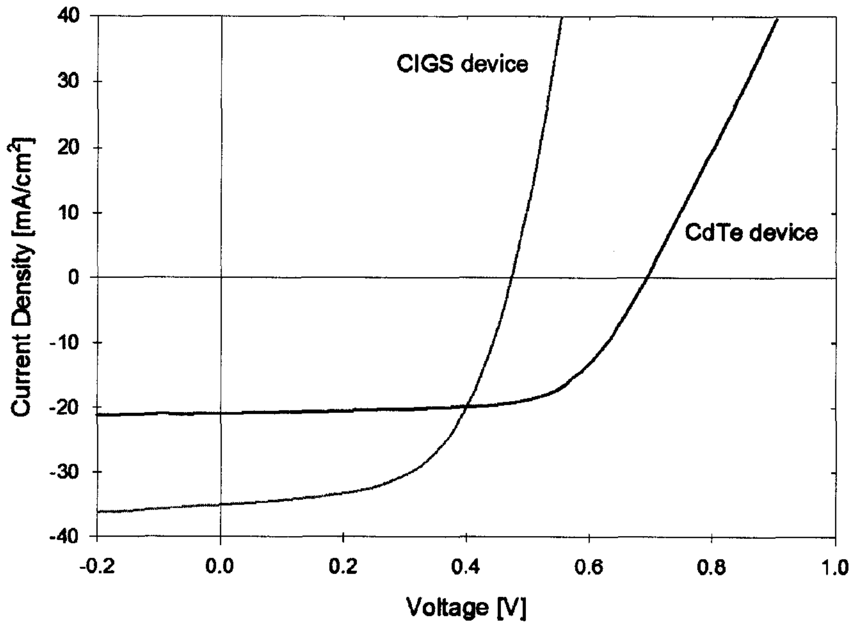

Figure 2.5: Examples of JV data for a CdTe cell and a CIGS cell manufactured by industrial processes. Note that the higher bandgap CdTe cell has higher open-circuit voltage, but lower short-circuit current. Both devices have efficiency = 9.5%.

true for white-light illumination intensities of less than one sun.

QE measurements require a calibrated reference device. Results presented here use a crystalline silicon solar cell calibrated at the U.S. National Renewable Energy Laboratory (NREL). Its QE is referred to as $QE_{ref}(\lambda)$. After several minutes for the probe-beam light source to stabilize, the current response of the reference device is measured ($I_{ref}(\lambda)$), and the current response of the device-under-test is measured ($I_{test}(\lambda)$). The QE of the test device is obtained from

$$QE_{test}(\lambda) = QE_{ref}(\lambda)\frac{I_{test}(\lambda)}{I_{ref}(\lambda)}. \tag{2.9}$$

It is necessary to distinguish between *internal* quantum-efficiency and *external* quantum-efficiency. External QE is the more commonly published result, and can be affected by factors 'external' to the diode, such as reflections, and absorption in glass layers. Internal QE considers only the collection of those photons which are incident on the junction (rather than the device). Since internal QE is not reduced by reflection/glass absorption, it always

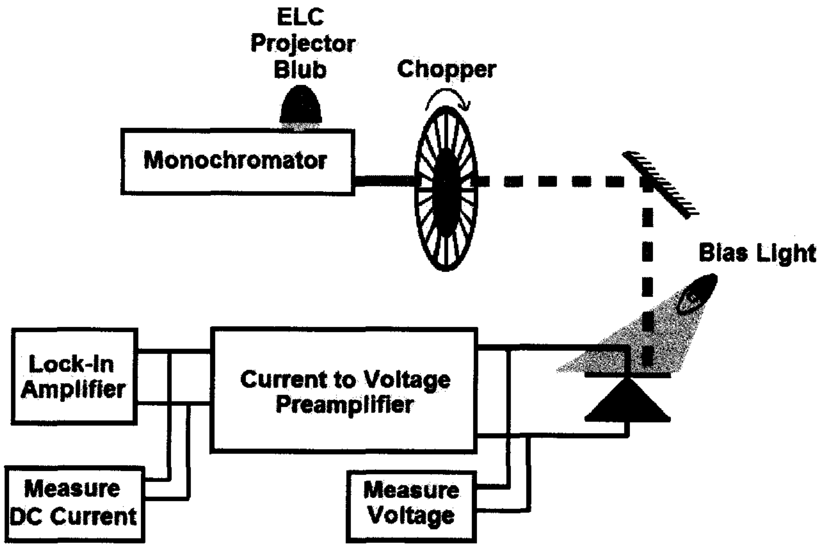

Figure 2.6: Schematic diagram for QE measurement.

exceeds external QE, and is often close to unity over a significant spectral range.

A schematic diagram for the QE measurement is given in Figure 2.6. An ELC projector bulb operated at 24 V, 10 A DC is used as the white light source at the input slit of the monochromator. The monochromator is a dual-grating 150-mm monochromator manufactured by Acton (SpectraPro-150). The spectral width of the probe-beam at the output of the monochromator is 4 nm. A mechanical chopper controlled by a Stanford Research chopper controller (SR 540) modulates the probe beam at 151 Hz, the beam is then collimated and focussed into a 1×2 mm spot on the test device. A Krypton flashlight bulb connected to a DC power supply is used as the source of DC white light bias. The solar cell is connected to a voltmeter for voltage monitoring. In parallel with the voltmeter, a current-to-voltage preamplifier (Stanford Research: SR 570) converts the AC photocurrent into an oscillating voltage.

The preamplifier allows for adjustment of the voltage bias, and also sinks away up to 5 mA of DC current due to white-light bias or forward voltage bias. This 5-mA limit for the preamplifier places a limit on the amount of white-light bias that may be tolerated in a measurement, as well as on the forward voltage. The oscillating voltage output of the

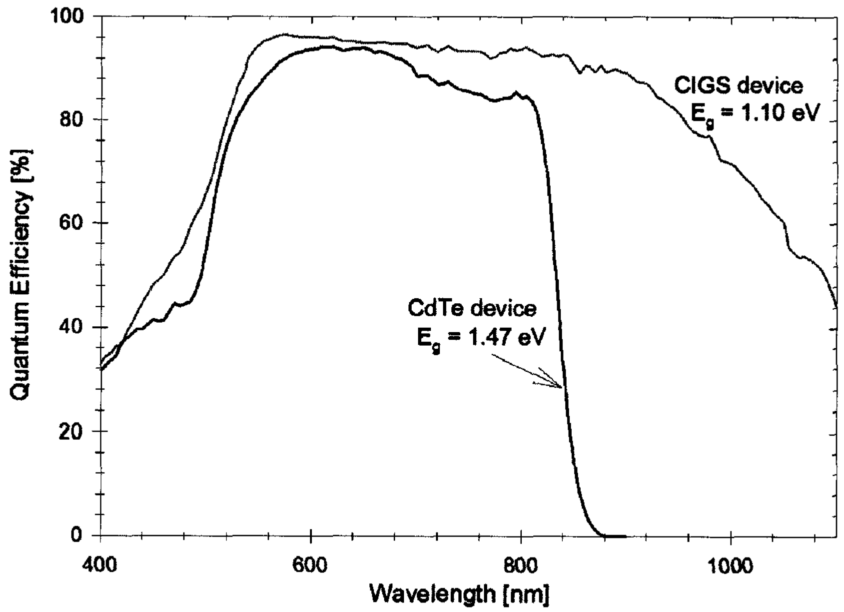

Figure 2.7: Examples of external QE measurements on the CdTe and CIGS devices shown in Figure 2.5. Absorber bandgaps are inferred from the long-wavelength QE cutoff for each device.

preamplifier is measured by a lock-in amplifier (SR 810). The lock-in reference frequency comes directly from the chopper controller, and a time-constant of 100 ms is generally used for data acquisition.

The DC component of the preamplifier output is monitored by an additional HP 34401A voltmeter. This DC current is minimized to reduce the risk of overloading the preamplifier or lock-in amplifier during measurement. The quantum-efficiency measurement is computer controlled with LabVIEW software, although the voltage-bias and current offsets on the preamplifier must be set manually before each measurement. Typical external QE data for a CdTe device and a CIGS device is shown in Figure 2.7.

QE data is taken in the range 350–1100 nm at 5-nm increments. Temperature control during QE measurement is not necessary, since with monochromatic illumination and relatively weak bias light, devices stay at room temperature during measurement, and QE results are insensitive to small temperature fluctuations. A probe-beam shutter is included between the output slit of the monochromator and the chopper, so that the probe beam can be blocked while the remainder of the system remains undisturbed to allow for background correction. A filter which cuts off light with $\lambda < 630$ nm is inserted at probe beam wavelengths greater than 650 nm to block second-order light from the measurement (e.g. 500 nm, $n = 2$ light during a measurement with $\lambda = 1000$ nm). QE results are accurate to within 2% based on comparison with reflection data in regions where reflection is the only loss mechanism.

Quantum-efficiency measurements will form the central theme of this dissertation. In later chapters, I will describe novel techniques that reveal details of device operation that would otherwise be inaccessible. For example, since different wavelengths are absorbed on different length scales, one can contrast collection due to shallow-penetrating photons with collection due to deep-penetrating photons. Collection depends strongly on such parameters as electric field strength, mobility of carriers, carrier lifetimes, etc. By making careful measurements of QE and using standard assumptions for the form of drift and diffusion currents, we can deduce the device band structure and carrier properties indirectly, and we can fine tune our models to account for diverse experimental conditions, including light bias and voltage bias.

2.2.3 Light-Beam-Induced Current

Light-Beam-Induced Current (LBIC) measurements characterize the spatial uniformity of a solar cell. A schematic of the LBIC apparatus is shown in Figure 2.8. The apparatus used for LBIC measurements is thoroughly described elsewhere by Hiltner and Sites [22, 23, 24]. Others use a similar approach [25, 26], which is a logical extension of early two-dimensional uniformity measurements [27, 28].

The photocurrent measurement circuit used with the LBIC technique is identical to that described above for the standard QE measurement. A device is scanned in two dimensions with a focussed laser beam, and photocurrent is measured at each position. A portion of the beam is split off for intensity monitoring by a calibrated photodiode. The ratio of the monitored beam intensity to scanning beam intensity is known, so that the photon flux

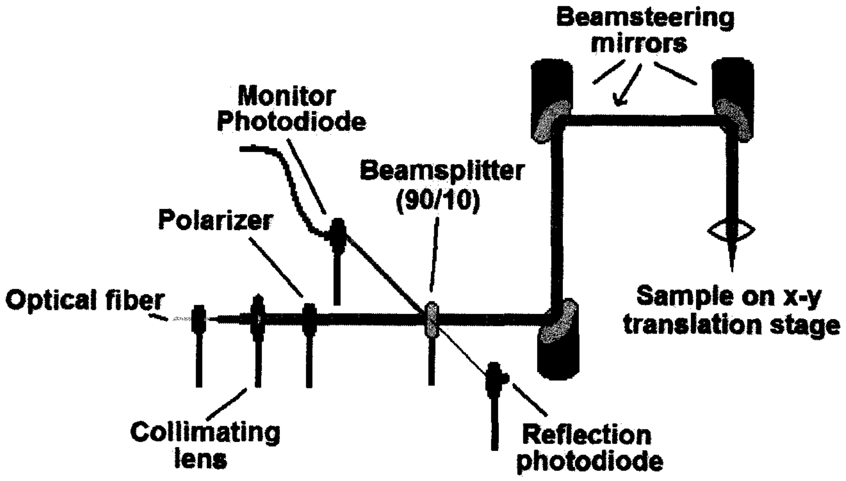

Figure 2.8: Schematic diagram for LBIC measurement.

on the device can be accurately determined. The result is a spatially-resolved quantum efficiency measurement. The capabilities of the CSU measurement system are probe-beam wavelengths of 638 nm, 688 nm, 788 nm, and a continuous range of 825–860 nm with a temperature-controlled diode laser. The measurement optics allow for focussing the laser to a spot size ($1/e^2$ radius) of 1 μm.

Three measurement scenarios are considered 'standard', these are: Low-resolution—a 100-μm spot with 50-μm steps between data points, usual area is 5000×5000 μm or whatever area encompasses the entire device, output power of the laser diodes limits light intensity to 0.2 sun; Mid-resolution—a 10-μm spot, 5-μm steps between data points, 500×500 μm area, one-sun intensity; High-resolution—a 1-μm spot, 0.5-μm steps between data points, 50×50 μm area, one-sun intensity. An example of medium-resolution data is shown in Figure 2.9. It is convenient to distinguish between observed nonuniformities caused by optical features and those caused by electrical features. Examples of optical features include scratches, dust, grid fingers, and otherwise nonuniform reflection. Examples of electrical features which could cause nonuniform collection include grain boundaries, variations in film thickness, and variations in interlayer alloying.

LBIC measurements will be used extensively in Chapter 5, and additional details will be given there.

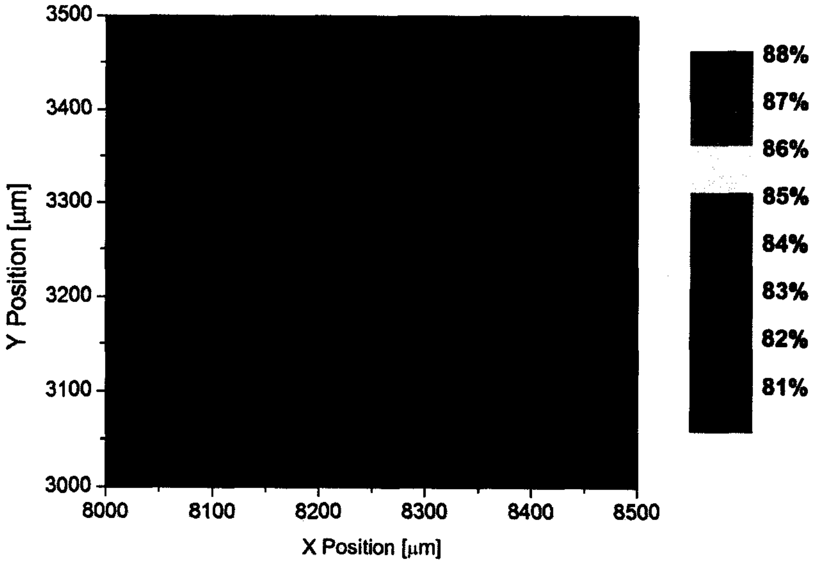

Figure 2.9: This graph shows medium-resolution LBIC data from a CIGS device. Laser wavelength is 638 nm, and intensity is one-sun. A 10 μm spot, with 5 μm steps between data-points results in 10,201 points in this measurement. This scan takes approximately 30 minutes to acquire.

2.2.4 Capacitance Measurements

Capacitance measurements are used to determine the carrier concentration in the absorber layer. In general, for a one-sided junction, capacitance measurements give the carrier concentration on the less-heavily doped side of the junction. In the specific case of thin-film solar cells, the hole concentration in the absorber is determined. In a p-n junction, the depletion width (W) is given by

$$W = \sqrt{\frac{2\varepsilon}{qN_A}(V_{bi} - V)}, \tag{2.10}$$

where ε is the permittivity in the absorber, N_A is the carrier concentration in the absorber, V is the applied voltage and V_{bi} is the built-in voltage. If the device is modeled as a parallel-

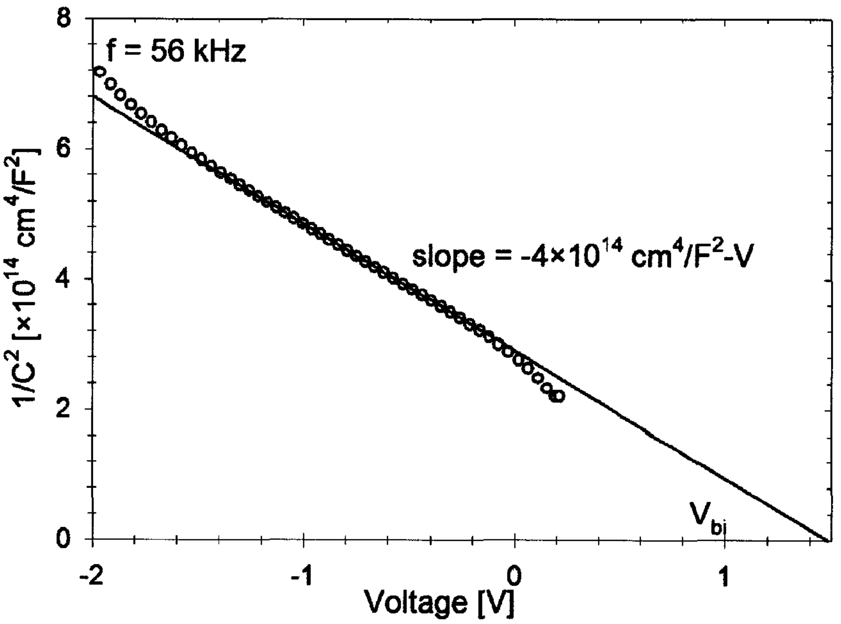

Figure 2.10: A capacitance-voltage graph for a $CuIn_{1-x}Ga_xSe_2$ device, with a straight-line fit to reverse-bias data. Using the analysis discussed in Section 2.2.4 the carrier concentration is determined to be 2–3 × 10^{16} cm^{-3}, which is common for CIGS devices.

plate capacitor, the capacitance per unit area (C) is given by

$$C = \frac{\varepsilon}{D}, \tag{2.11}$$

where D is the separation between the charge on the capacitor's "plates". Substituting W for D gives

$$C = \sqrt{\frac{q\varepsilon N_A}{2(V_{bi} - V)}}. \tag{2.12}$$

Plotting $1/C^2$ vs. V then, should yield a straight line with a slope of $2/q\varepsilon N_A$ and a voltage-axis intercept at $V = V_{bi}$ if carrier density is independent of distance into the absorber. Typical results on a CIGS device are shown in Figure 2.10, for which analysis suggests carrier concentration of 2–3 × 10^{16} cm^{-3}. The voltage-axis intercept in this data is somewhat larger than V_{bi}, probably due to a higher concentration layer close to the junction in the p-type absorber [29].

Capacitance measurements used an impedance analyzer (HP 4192A) to supply a DC voltage bias and a 20-mV AC signal in the frequency range of 1 kHz to 1 MHz. Capacitance measurements were usually performed between -2 V and $+0.2$ V. At more-negative diode voltages, the risk of reverse-voltage breakdown is significant. At forward voltages greater than $+0.2$ V, non-negligible forward currents are present and the diode impedance is more conductive than capacitive, making capacitance analysis difficult [29]. Since in general $V_{applied} \neq V_{diode}$, the actual diode voltage is monitored with a voltmeter, and a feedback loop is used to maintain the correct diode voltage during a measurement. A relay switch automatically switches the device between the impedance analyzer (voltage-bias supply) and the voltmeter so the voltmeter is not part of the circuit during capacitance measurement. Capacitance measurements are computer controlled with LabVIEW software, and at each data point the frequency, capacitance, conductance, applied voltage, and measured voltage are recorded.

The usual prescription for capacitance measurements involves first varying the frequency of the AC signal while holding the applied bias constant at several voltages in the -2 V to 0.2 V range. This is done so that a frequency can be chosen such that capacitance is insensitive to frequency throughout the voltage range. The selected frequency is usually the order of 100 kHz. The phase angle θ of the complex impedance at the selected frequency is checked against the requirement that $\theta > 20°$ for each voltage. The $\theta > 20°$ requirement ensures that the complex impedance is not so resistive that capacitance analysis is distorted. Finally, the capacitance-voltage measurement is performed, with voltage steps of approximately 0.02 V.

2.2.5 AMPS-1D Simulations

The numerical simulation package AMPS-1D is used to simulate device operation and band profiles. AMPS (Analysis of Microelectronic and Photonic Structures) was developed by Stephen Fonash *et al.* at Pennsylvania State University with support from the Electric Power Research Institute (EPRI). In a one-dimensional semiconductor device, the physics of device operation can be described by solving Poisson's equation, and the electron and hole continuity equations at each position throughout the device [21, 30]. AMPS-1D simulates device operation by solving these three coupled differential equations,

$$\nabla \cdot \varepsilon \nabla \phi(x) = -q[p(x) - n(x) + N_D^+(x) - N_A^-(x) + p_t(x) - n_t(x)] = -\rho(x), \tag{2.13}$$

$$q\frac{\partial n(x)}{\partial t} = q(G_n(x) - U_n(x)) + \nabla \cdot \vec{J}_n(x), \tag{2.14}$$

$$q\frac{\partial p(x)}{\partial t} = q(G_p(x) - U_p(x)) - \nabla \cdot \vec{J}_p(x), \tag{2.15}$$

at each point in a one-dimensional mesh throughout the device. In the above equations, G is the generation rate and U is the recombination rate of holes (subscript p) or electrons (subscript n). Free carrier concentrations are given by n and p; trapped holes (electrons) by p_t (n_t); and ionized donors (acceptors) by N_D^+ (N_A^-). The electrostatic potential is ϕ, and $\vec{J}$ is the current due to holes or electrons. AMPS considers steady-state solutions, so Equations 2.14 and 2.15 are slightly simplified, since $\frac{\partial n(x)}{\partial t} = 0$ and $\frac{\partial p(x)}{\partial t} = 0$. The total number of mesh points used is several hundred, and as a rule-of-thumb, a minimum of thirty points are used in any one device layer. The numerical solution of these coupled equations can serve as a guide to new models of device operation.

Since the calculations require input of device parameters, some of which may not be well-known, the usual goal of AMPS simulations is not to reproduce experimental results and conclude knowledge of all aspects of the device. Instead, AMPS is best used to determine the trends associated with variation of some parameter(s), and the sensitivity of device operation to these variations. A subset of the standard input parameters, selected by Gloeckler [31, 32] is given in Table 2.1. Additional parameters are discussed as needed in Chapter 3.

Table 2.1: The input parameters chosen for AMPS-1D simulations are called the *baseline case* and were selected by Gloeckler [32]. Device thickness is D, carrier concentrations are n and p, bandgap is E_g, and mobilities are μ.

	CdS	**CIGS**	**CdTe**
D [μm]	0.02–0.05	2.0	3.0
n, p [cm^{-3}]	n: 10^{17}	p: 2×10^{16}	p: 2×10^{14}
E_g [eV]	2.4	1.15	1.5
μ_e [cm^2/Vs]	100	100	320
μ_h [cm^2/Vs]	25	25	40

2.3 Thin-film Solar Cells

2.3.1 CdTe

Devices made from CdTe absorbers are attractive for commercialization because they use a relatively simple II-VI semiconductor that can be deposited in a variety of industry-friendly ways to yield high-efficiency devices. The present efficiency record for a CdTe device is 16.5% by Wu *et al.* [33]. CdTe devices are usually deposited in a superstrate configuration so that the back contact layers experience a minimum of high-temperature processing steps.

Common CdTe deposition methods include close-spaced sublimation (CSS), vapor-transport deposition (VTD), electrodeposition [34, 35], and sputtering [36]. CdS layers are often deposited by chemical-bath deposition (CBD) [37], although CSS is also used and should be a favorable approach on the industrial scale, since it is a 'dry' process that does not require high vacuum. SnO_2 is often used for the transparent front contact, and a high-resistivity layer between the low-resistance SnO_2 and CdS generally results in improved device performance, probably due to mitigation of nonuniformities [38]. Another processing step that is virtually always used is exposure of the film to chloride species, usually in the form of $CdCl_2$ salt, and usually in the presence of oxygen. A post-deposition anneal in the presence of $CdCl_2$ promotes the formation of larger grains in the film and results in improved device performance [39]. CdTe technology faces some challenge of overcoming public-perception problems due to the presence of the heavy-metal cadmium, although the CdTe compound is stable and not hazardous. The amount of Cd in a one-kW PV installation is less than that in ten size-C Ni-Cd batteries, and the PV panel is undoubtedly a much better use of material [40].

2.3.2 CIGS

Devices made from $\mathrm{CuIn}_{1-x}\mathrm{Ga}_x\mathrm{Se}_2$ absorbers are attractive for commercialization of thin-film PV because they have already achieved high efficiencies in laboratory-scale devices, including records of 19.5% by Contreras *et al.* [41] and Bhattacharya *et al.* [42]. The semiconductor layers in a CIGS device usually include the following: At the front of the device, a ZnO transparent contact. A thin CdS buffer layer serves as the n-type window layer in the p-n junction. The p-type absorber most commonly used is $\mathrm{CuIn}_{1-x}\mathrm{Ga}_x\mathrm{Se}_2$ with $x \simeq 0.3$, which results in $E_g \simeq 1.15$ eV. The extremes of the alloy have $E_g = 1.0$ eV (CuInSe_2) and $E_g = 1.7$ eV (CuGaSe_2). Sulfur can be substituted for Se to achieve higher bandgaps [43]. The expected optimal bandgap for the absorber layer is in the range 1.4–1.5 eV. In the case of CIGS, 1.15 eV is empirically optimal, due to poorer electrical properties in higher-Ga devices, where voltage-dependent current collection and increased recombination reduce the fill-factor and V_{OC}, respectively [44]. The metallic back contact most often used in CIGS devices is Mo on a glass substrate for structure, or sometimes on a stainless-steel foil for flexible devices.

CIGS layers are most often deposited by co-evaporation of the constituent elements or by selenization (heating in the presence of Se vapor) of precursor films. To date, the highest efficiency devices have been produced by NREL's patented 3-stage deposition process, where temperature and Ga content is tuned throughout deposition. The CdS layer is often deposited by chemical-bath deposition and the ZnO by sputtering. As in CdTe devices, inclusion of a high-resistance TCO layer often improves device performance.

Chapter 3

Role of Light Bias in Quantum Efficiency Measurements

3.1 Photoconductivity

A photovoltaic device converts the energy of an absorbed photon into an electron-hole pair which can be used for electrical energy. Not all absorbed photons contribute to the electrical output of the cell. These photons which do not contribute to the electrical output can have a variety of secondary effects. One such secondary effect sometimes seen in thin-film cells is photoconductivity, which is often observed in semiconductors with low free carrier concentrations (such as those at low temperatures), those that are lightly doped, or those with free carriers compensated by trap states [45]. In a thin-film solar cell, the CdS layer fits the last of those categories—n-type carriers are compensated by trap states. Under illumination, the trap occupation changes, resulting in higher n-type carrier concentration than in the dark. For this reason, when making measurements with varied illumination spectra, we must consider whether or not the trapping states in CdS are sensitive to the illumination used. The most common PV measurement which often uses non-AM1.5 illumination is the quantum-efficiency (QE) measurement. Interpretation of QE measurements are prone to errors if photoconductive effects are ignored.

3.2 The Need for Light Bias

Under standard conditions, QE measurements quantify the spectral sensitivity of a solar cell. The idealized QE measurement would hold the cell at zero voltage bias and use one-sun light-bias while a chopped monochromatic probe beam is used as an AC perturbation [46, 47]. These ideal conditions are virtually never used in practice, primarily because of the difficulty in measuring a small AC perturbation superimposed on a large DC bias-current. In addition to this technical limitation, we often choose to measure QE at non-zero voltages where light-bias effects are larger. When non-standard measurements (e.g. in the dark, under voltage bias) yield results that are clearly different from the idealized measurement, the term apparent quantum efficiency (AQE) has been adopted.

AQE results can differ significantly from the standard measurement, but they can also provide us with valuable information about the band structure of the device, such as the amount of photoconductivity in the window layer (CdS) and the change in space-charge width under illumination. By examining experimental curves taken under a variety of light-bias conditions, and comparing the results to numerical simulations, one can suggest which conditions are sufficient for valid results, and offer physical explanations for the non-ideal behavior. In this chapter, I will use the convention introduced by Gloeckler [48] and refer to distinct regions of the light spectrum as "CdS region" (350 nm $< \lambda <$ 550 nm) and "bandgap (E_g) region" (λ within 50 nm of λ_{gap}). I will choose my language here carefully: "CdS region" refers to a section of a QE curve, while "CdS layer" refers to the layer of material in a device.

Note that the two spectral regions mentioned above can be correlated with distinct positions within a device. Infrared light from the E_g region of the spectrum is only weakly absorbed in the device, and these photons may penetrate the entire thickness of the absorber to the back contact layer. Short-wavelength light from the CdS region of the spectrum is absorbed mostly in the CdS layer, though the CdS layer is engineered to be thin, so some of these photons are transmitted to the absorber layer adjacent to the CdS.

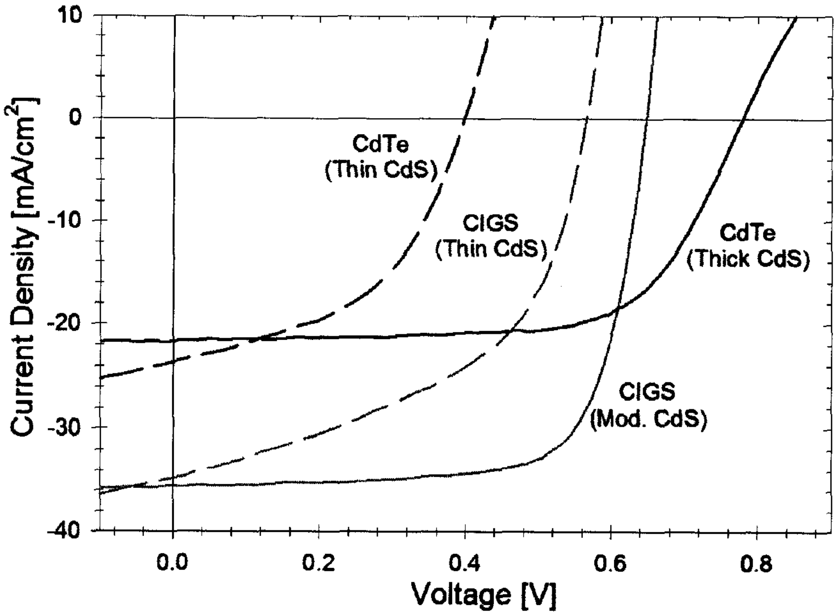

Figure 3.1: J-V curves of four devices. CdTe devices had thin and thick CdS layer thicknesses (5 nm and 230 nm), and CIGS devices had thin and moderate CdS layer thicknesses (10 nm and 40 nm).

3.3 Window-layer Photoconductivity

The following discussion will focus on four devices, which include CdTe devices with both thin (5 nm) and thick (230 nm) CdS layers and CIGS devices with thin (10 nm) and moderate (40 nm) CdS layers. CIGS devices with thicker CdS layers were not available. The J-V curves of these devices are shown in Figure 3.1. Devices with thin CdS layers typically have poor efficiency but were deliberately chosen to emphasize the AQE effects which occur when the shunt resistance is low.

3.3.1 Effects Observed in CdTe Cells

An examination of QE curves for the two CdTe devices offers clues to the role of the bias light. Figures 3.2 and 3.3 show QE curves for CdTe devices with thin and thick CdS layers. Curves were measured at 0 V and +0.3 V, in the dark and with 0.25 sun white light bias. DC light bias of 0.25 sun results in approximately 5 mA of DC photocurrent. Changes in

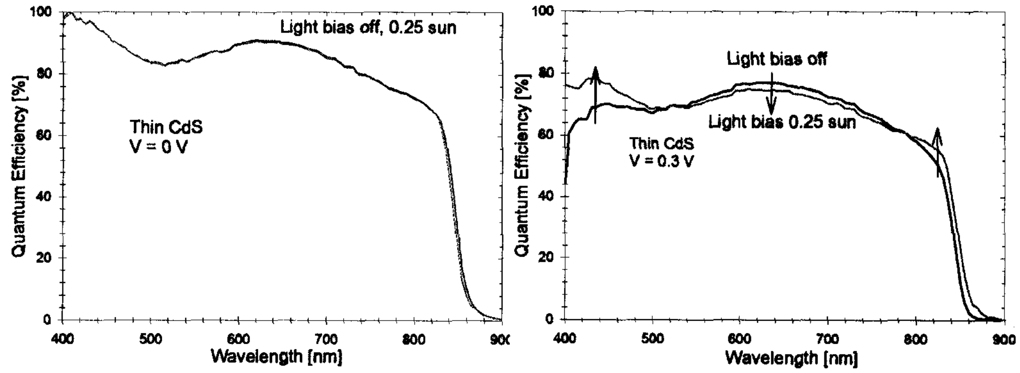

Figure 3.2: A CdTe device with a thin CdS layer shows little change with light bias at 0 V, but in forward bias, a significant effect in the CdS region and in the E_g region is observed.

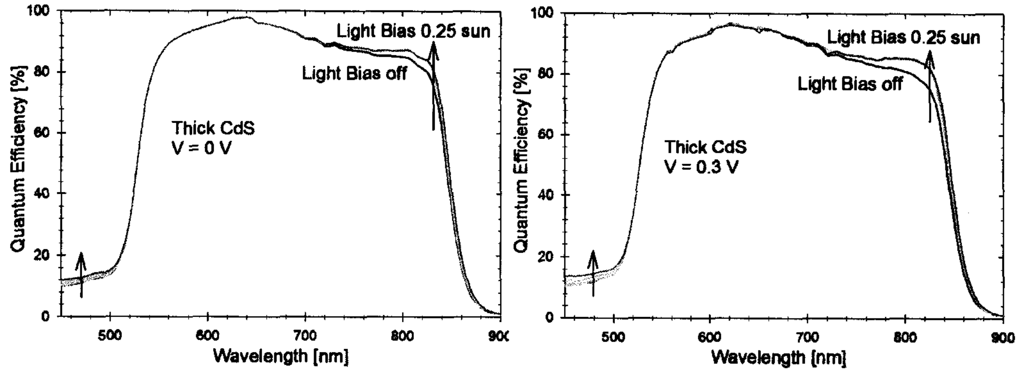

Figure 3.3: A CdTe device with a thick CdS layer shows a small change with light bias at 0 V, and a slightly larger effect in forward bias.

QE are generally observed only in the CdS region and the E_g region, consistent with the reporting of others [49, 50].

In the CdS spectral region, deep acceptor states in the CdS layer are occupied by light-generated holes, which makes the CdS more n-type and improves collection of carriers generated by short-wavelength photons. A secondary effect of the trapped holes is to increase the positive space-charge in the CdS layer. The resulting increase in the negative space-charge in CdTe improves the collection of electrons generated deeper into CdTe. This results in an apparent—*but not actual*—downward shift in the absorber bandgap energy. Since thick CdS layers have more capacity for space charge than thin CdS layers, devices with thick CdS layers exhibit larger depletion width changes in response to bias light, as shown in the zero bias curves (left-hand side) of Figures 3.2 and 3.3.

3.3.2 Forward-bias QE measurements

For each CdS layer thickness, the effect of light bias is much more prominent in the forward voltage data than at zero bias, as shown in the forward-bias curves (right-hand side) of Figures 3.2 and 3.3. Different electrical mechanisms are responsible for the effects seen in the different regions of these QE curves. In the E_g region: as voltage is increased, the high carrier concentration (n^+) in the photodoped CdS layer maintains the wide zero-voltage space-charge region in CdTe relative to the dark case. As in the 0 V situation, this should not be interpreted as a change in the absorber bandgap.

The effect observed in the CdS region is slightly different. When the 150 Hz ($\sim$ 6 ms cycle time) chopped probe beam is absorbed in the CdS layer in the absence of DC bias light, the device alternates between n-p and n^+-p regimes in-phase with the probe-beam. While the probe-beam is unblocked (for $\sim$ 3 ms) the forward-biased n^+-p device produces more forward current than the n-p device does during the 3 ms that the probe-beam is blocked. The result is a forward-current signal at the chopping frequency, which is opposite in direction to the photocurrent signal, and is proportional in size to the amount of photoconductivity in the CdS layer. This forward current subtracts from the photocurrent signal, leading to an apparently reduced QE in the CdS region. This effect is much larger in the thin CdS device, because it is a poorer device and has much higher forward current at +0.3 V (see Figure 3.1). With light bias the device is in a steady-state n^+-p condition, and the resulting forward current can be offset by the preamplifier. In this case, the measured photocurrent is not artificially reduced.

Notice that in the forward-bias curve in Figure 3.2, an inversion of the QE shift takes place in the wavelength range 550–800 nm, where QE is higher in the dark than in the light. This feature of forward-bias QE curves is reproducible in AMPS-1D simulations, as shown in Figure 3.4. Under white-light illumination, the absorber material (in this case:

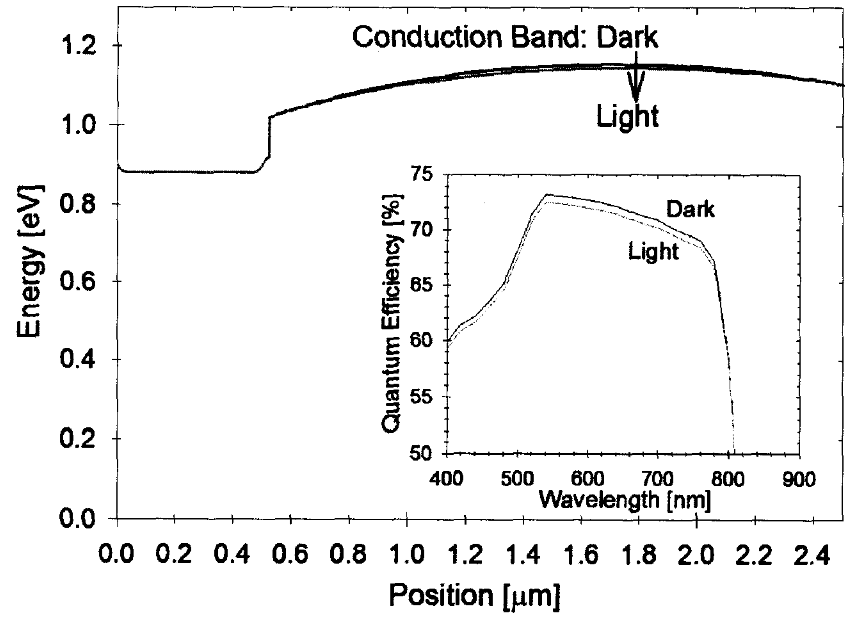

Figure 3.4: AMPS-1D simulation of a CdTe device near V_{OC}. This simulation uses the CdTe baseline parameters defined by Gloeckler [32], except that the CdTe layer is thinned to 2 μm, and the carrier concentrations in CdS and CdTe are reduced by factors of 10 and 2, respectively. The conduction band in the dark is slightly above the conduction band under illumination, leading to better collection in the dark (absence of bias light) as shown in the QE inset.

CdTe) becomes slightly less p-type due to the population of photogenerated electrons in the conduction band. Near J_{SC} this causes no difference in carrier collection, but near V_{OC} a stronger field exists in a non-illuminated device. A comparison of the J-V curves of the devices used (Figure 3.1) shows why only the device shown in Figure 3.2 demonstrates this behavior. The thin-CdS/CdTe device is the only one of the four shown in which QE was measured close to V_{OC}. This phenomenon presents a good example of the use of careful QE measurements and AMPS-1D simulations to reveal unusual device physics.

The J-V curves in Figure 3.1 and QE curves of Figures 3.2 and 3.3 also illustrate one of the most active areas of research in thin-film PV. It is a generally observed trend that devices with thick CdS layers have lower current densities than devices with thin CdS layers, as can be seen in the J-V and QE curves above. This reduction is due to photon absorption in the CdS layer, which does not contribute to current because photogenerated holes are immediately trapped in the CdS. The obvious solution to this problem is to make the CdS layer thin, or to omit it entirely. Devices with thin or absent CdS layers are empirically very low-performing, with voltage losses and fill-factor losses greater than the performance increase due to current gains [44, 51]. Weak performance for thin CdS is well demonstrated by the J-V curves in Figure 3.1. An additional strategy is to replace the CdS with another material with a wider bandgap (an “alternative buffer layer”), which has been done with mixed results (summarized by Pudov [52]). One result of this approach is discussed again in Section 3.3.4.

3.3.3 Effects Observed in CIGS Cells

Figure 3.5 shows analogous QE curves for CIGS devices with thin and average CdS. No change with bias light was observed in the QE curve for either of these devices at zero bias or in forward bias. This is in contrast with the observations made on CdTe devices. CIGS devices usually have higher carrier concentrations in the absorber than CdTe devices, therefore show less sensitivity to bias light conditions because space-charge widths are less susceptible to light modification. An exception is discussed in Section 3.3.4.

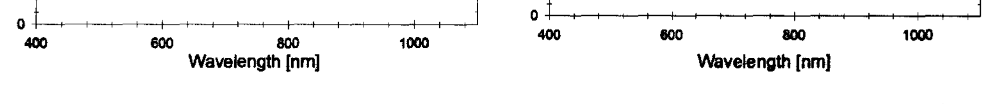

Figure 3.5: QE curves in the dark and with 0.25 sun light bias are shown for two CIGS devices. The effect of light bias on these devices is very small.

3.3.4 Conduction-band Offset at Window/Absorber Interface

The effects of bias light are not always as modest as those shown in Figures 3.2 and 3.3. As discussed in Section 3.3.1, alternative buffer layers are sought to improve current response without sacrificing voltage. This is most often done in CIGS devices. One possible problem associated with some high-E_g alternative buffer layers is the presence of a spike in the conduction band at the interface between the window and the absorber. The spike serves as a barrier to photogenerated electrons as they move from the p-type material to the n-type material [49, 53]. Figure 3.6 shows an example of a resulting QE curve when a photoconductive barrier is present. Note that in contrast to the effects seen in the CdTe curves of Section 3.3.1, the effects of a conduction-band barrier are not limited to the E_g and CdS regions.

In the case of Figure 3.6, a nominal ZnS layer was used as an alternative buffer (in place of CdS). Although ZnS has a high bandgap (E_g= 3.7 eV), it is known to form lower-bandgap secondary phases ZnO and $Zn(OH)_2$, so the notation ZnS(O,OH) is often used for this buffer layer [54]. The effective bandgap of the buffer layer is likely much closer to 3.3 eV (ZnO bandgap) since the ZnS(O,OH) layer has been shown to be photoactive within a CIGS device (Pudov [52]). The strong dependence of collection on bias light intensity seen in Figure 3.6 agrees with the J-V observations by Pudov. In this case, the effect of light bias on QE measurements has clearly not saturated and the AQE shift would likely continue to become larger with increased bias light intensity.

The use of ZnS as a buffer layer is not a requirement for the effects of a conduction-band barrier to be seen, but was used because of the clean experimental data available. Lightly-doped (or highly-compensated) CdS could have the same effect, as demonstrated in the AMPS-1D simulation summarized in Figure 3.7, which suggests a scenario where a low carrier concentration CdS layer could cause similar effects to those shown in Figure 3.6. A conduction band barrier blocks photogenerated electrons in the dark. When the CdS layer is photodoped, the barrier is lowered and the band alignment and QE results approach one-sun conditions. Since the primary mechanism in Figure 3.6 is a current barrier, the effects

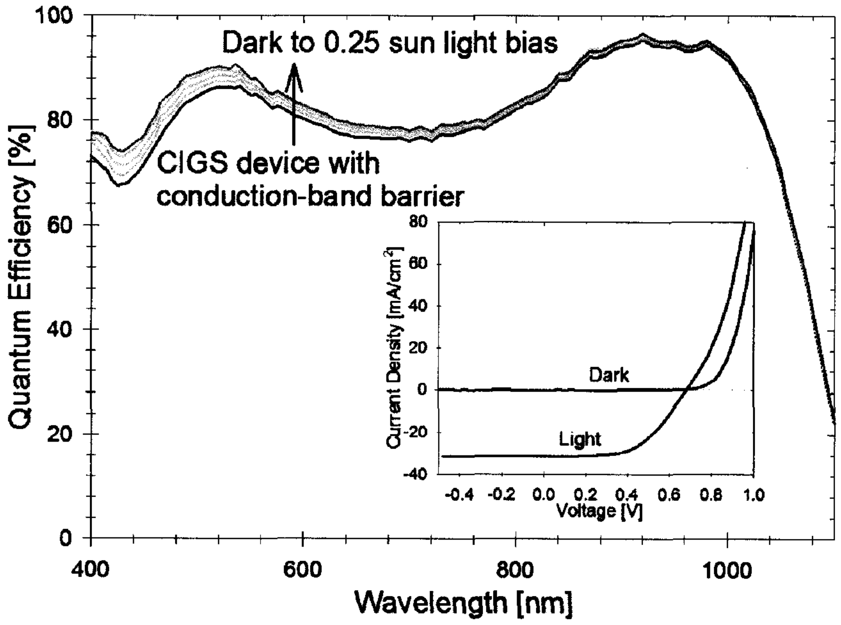

Figure 3.6: Strong QE dependence on bias light suggests a large secondary barrier in the conduction band. Note that the effect is not limited to the CdS region or the E_g region. The J-V curve for this device is inset in the figure.

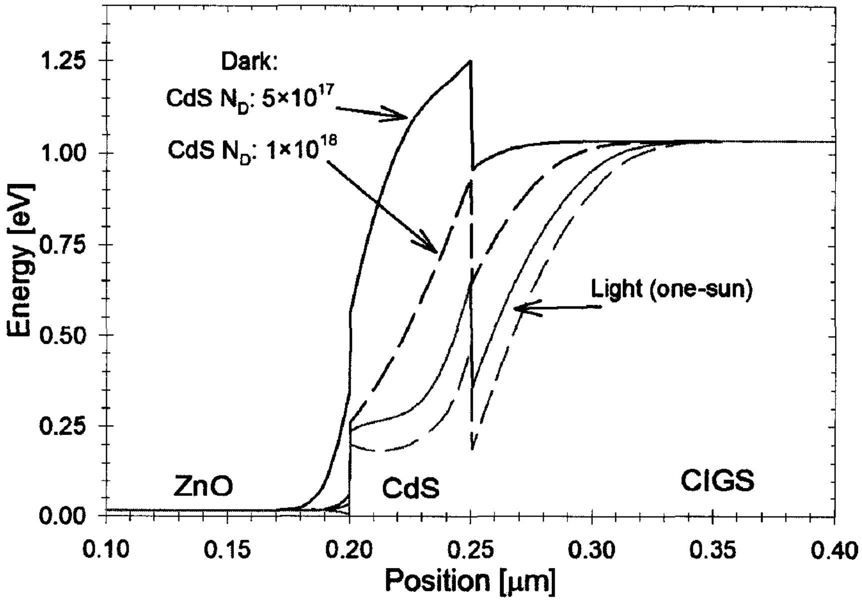

Figure 3.7: Calculated conduction bands in a CIGS device. For highly doped CdS layers (gray curves), light bias has little effect on current flow.

are observed at all wavelengths in contrast to the case of CdTe in Figures 3.2 and 3.3, where only the distinct CdS and E_g regions were affected.

3.3.5 Reliability Tests

Two convenient tests address the reliability of QE results. The first is a comparison of J_{SC} measured in one-sun J-V measurements with J_{SC} determined by integration of QE curves scaled to the one-sun spectrum (see Equation 2.8). For zero-voltage measurements on the CdTe and CIGS devices discussed here, J_{SC} results from these two independent measurements are in agreement to within 2mA/cm^2, which is interpreted as an indicator of valid results. Table 3.1 summarizes these results, which hold true in general. Note that integrating QE curves results in a J_{SC} value which corresponds to active area (semiconductor area minus grid coverage), while J-V measurements are often reported as total area values (thus somewhat less than the active-area J_{SC} for CIGS devices, which have grid coverage). For a valid comparison, J_{SC} values must use a consistent area was done in Table 3.1.

Table 3.1: A comparison of active-area J_{SC} from J-V measurements and as extracted from QE measurements shows good agreement, which suggests that the QE results are accurate.

Device	JV [mA/cm^2]	QE [mA/cm^2]
CdTe: Thin CdS	23.5	24.5
CdTe: Thick CdS	21.7	21.3
CIGS: Thin CdS	36.9	35.8
CIGS: Thick CdS	36.2	34.6

The second test is a comparison of results with measured reflection curves (R). In regions of the spectrum where electrical losses in the device are minimal (where internal quantum efficiency ≈ 1), plots of QE and $1-R$ are in good agreement over a significant range of wavelengths, as shown in Figure 3.8.

3.3.6 Saturation of Light-bias Effects

Although the intensity of bias light was limited to roughly 0.3 sun, the data at lower bias light intensity indicates that the light bias effects have saturated at much lower intensities. Figure 3.8 shows QE curves for a CdTe device with a thick CdS layer. The curves were measured in the dark and with 0.01, 0.03, and 0.06 sun light bias. Results converge as light intensity increases, and the curves with 0.03 sun and 0.06 sun intensity are identical. This suggests that the effect of light bias has saturated, and that higher intensities will not improve the accuracy of the results shown in Figure 3.8. We can also conclude that the 0.25 sun light bias used in Figure 3.3 was more than sufficient for accurate results. Despite this, since different devices contain different CdS thicknesses and different trap densities, one cannot make a general statement of the form "X fraction of a sun is sufficient for accurate QE results".

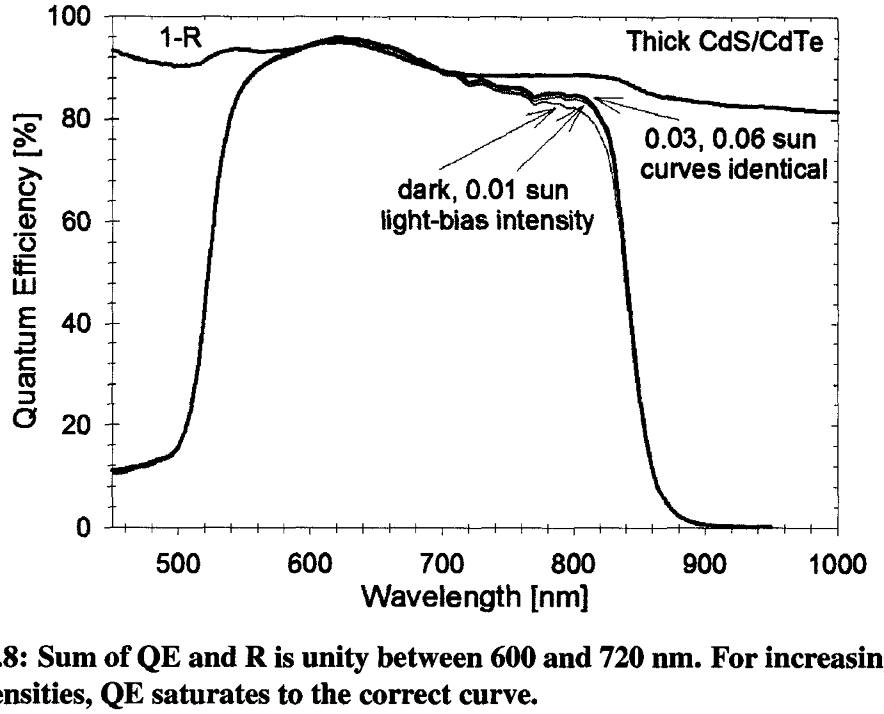

Figure 3.8: Sum of QE and R is unity between 600 and 720 nm. For increasing white-light intensities, QE saturates to the correct curve.

3.3.7 Summary of Photoconductive CdS Effects

The presence of blue bias light, either by itself or as a component of white light, generally forces the CdS window material to be a strongly n-type layer. This occurs because deep acceptor states are occupied by bias-light generated holes, while the free electrons remain in the conduction band. The depletion width in the absorber increases to balance the increased positive space-charge in the CdS layer. The result is a steady-state condition where the depletion layer is wider under light bias than in the dark. QE measurements made in the dark do not allow for the compensation of deep acceptors in the CdS layer since for most of the spectrum, no absorption takes place in the CdS layer.

Contrast the use of light bias with the situation where a chopped blue probe-beam is the only light absorbed by the photoconductive CdS layer. In this case the diode alternates between an n-p junction and an n^+-p junction in-phase with the probe beam, and in forward bias we can expect that the forward current will be modulated at the probe-beam chopping frequency, thus subtracting from the measured photocurrent. An extreme case occurs when forward currents are already on the order of the photocurrent generated by the probe beam, and the AQE becomes zero or negative [48].

The problem is particularly severe in CIGS cells with a "spike" in the conduction band at the window/absorber interface, as shown in Figure 3.7. In this case, the spike is an electron barrier which varies in-phase with the probe beam. The conduction-band spike is most likely to have an effect when CdS layer thicknesses are greater than 100 nm, and is not a concern in CdTe devices since the CdS/CdTe interface is a "Type-II" heterojunction without a spike [52].

3.4 Device Physics as Deduced from Quantum Efficiency Measurements

In seeking to understand the operation of a thin-film solar cells, the band structure of the device is generally the most important information to be learned. This information is not directly measurable in an operating device by any method, although some information is available indirectly by spectroscopic methods. Careful analysis of QE measurements can provide us with some of this information, and in particular can tell us if photoconductivity is present in device layers.

In Section 3.3.1, the effects of photoconductive CdS on QE measurements on CdTe devices were shown. In summary, effects are modest at zero bias and are characterized by improved collection in both the CdS and E_g spectral regions. In the E_g region, the increased collection efficiency for deep-generated electrons (by low-energy photons) could be mistaken for a reduction in the absorber's bandgap energy, when it is entirely a collection effect. In the CdS region, the effects are attributed to higher conductivity in the CdS layer under illumination. Observed effects were stronger in devices with thicker CdS, as thick CdS has more capacity for space charge and can more strongly affect the band structure.

Solar cell devices are much more sensitive to DC illumination conditions during QE measurements when they are in forward voltage bias. The major complication of forward-bias measurements with respect to zero-bias measurements is the presence of forward current (J_f). Since forward current depends strongly on carrier concentrations and band profiles, if these are modified by the probe-beam then, J_f could vary at the chopping frequency and thus be difficult to separate from the photocurrent. The best way to eliminate this concern during forward-biased measurements is to use sufficient light bias that any light-sensitive J_f effects saturate and time variations in J_f are insignificant compared with the probe-beam photocurrent. For most, but not all devices, this occurs with less-than 0.25 sun light bias.

When observed effects of light bias on QE curves are not confined to the CdS and E_g

regions, but instead affect the entire QE curve, the presence of a conduction-band barrier is a possible cause. This most often occurs in CIGS devices. Some cases where barriers are present include in devices with very low CdS carrier concentrations and those where alternative buffer layers are used, especially those such as ZnS which form large conduction-band offsets with CIGS.

Chapter 4

Effect of Lifetime on Quantum Efficiency

4.1 Collection and Quantum Efficiency

Quantum efficiency is a combination of the generation of electron-hole pairs and the effectiveness of carrier collection within the solar cell, given by the relation

$$QE = Collection \times Generation. \tag{4.1}$$

If increased J_{SC} is a chosen pathway to improving efficiency, then we must increase QE at some wavelengths. Equation 4.1 gives us two options to achieve this. We can (and do) increase *generation* by using more-transparent window layers and anti-reflection coatings, allowing more electron-hole pairs to be generated. We also can increase *collection* by fabricating devices with longer carrier diffusion lengths, fewer recombination centers, or band profiles engineered to reduce recombination (such as back electron reflectors).

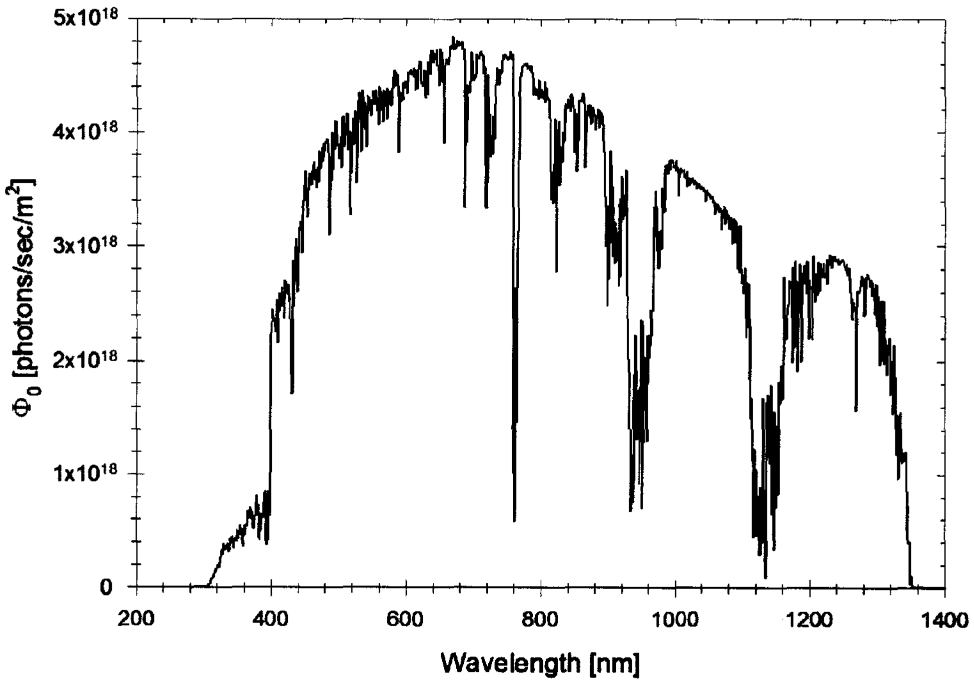

Figure 4.1: The photon flux of AM1.5 illumination shows the effects of atmospheric absorption.

4.1.1 Generation

The generation function ($Gen(x,\lambda)$) depends on the AM1.5 spectrum and the absorption coefficient of the material so that

$$Gen(x,\lambda) = (1-R(\lambda))\Phi_0(\lambda)\alpha(\lambda)e^{-\alpha(\lambda)x}, \tag{4.2}$$

where $R(\lambda)$ is the fraction of incident photons reflected by the cell, $\Phi_0(\lambda)$ is the photon flux shown in Figure 4.1, and $\alpha(\lambda)$ is the absorption coefficient of the material, shown in Figure 4.2. The depth within the absorber is x, where the metallurgical junction between the absorber layer and the CdS is defined as $x = 0$. The simple models discussed here assume that no absorption takes place in any window layers, and hence is generally valid for $\lambda > 500$ nm.

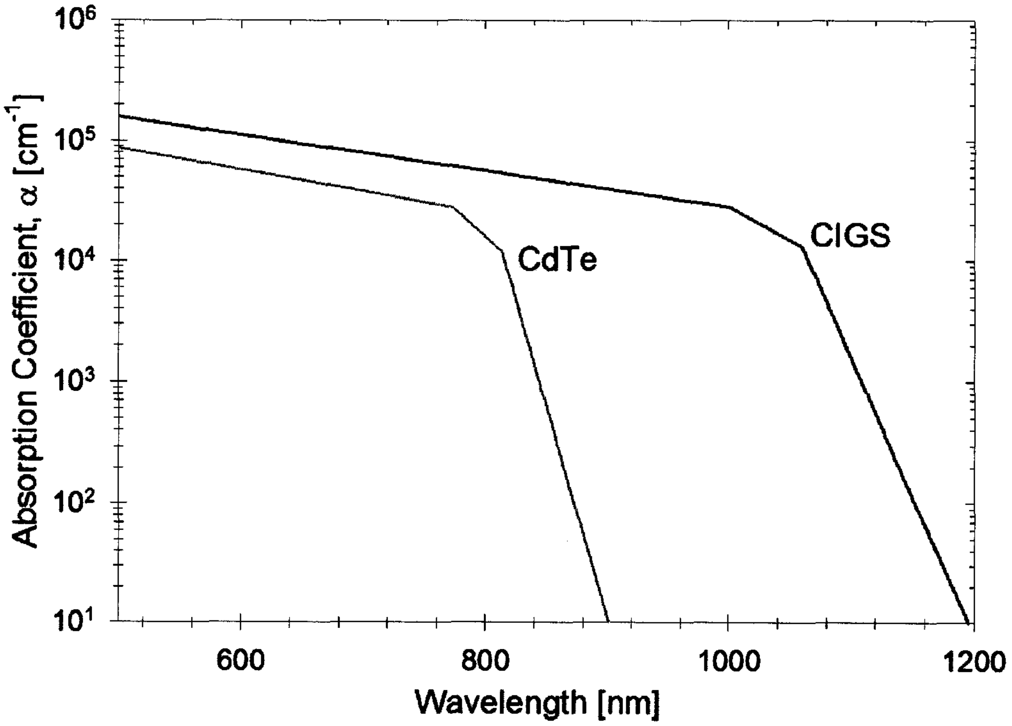

Figure 4.2: Simple models of absorption coefficients agree very well with experimental absorption curves for CIGS published by Albin *et al.* [55], and CdTe published by Myers *et al.* [56].

4.1.2 Collection

The generation function tells us the number of electron-hole pairs generated and how they are distributed throughout the thickness of the device. The collection function ($CE(x)$) tells us the probability that these charge carriers will be collected by the external circuit, and therefore contribute to J_{SC}. This is generally expressed as a fraction and referred to as collection efficiency. Depending on the depth within the device, different mechanisms are primarily responsible for photocurrent collection. Within the space-charge region (SCR) the built-in electric field sweeps electrons to the front of the device and holes towards the back, therefore collection is generally high. Outside of the SCR, carrier transport is limited by diffusion, and therefore collection is lower.

Table 4.1: For ease of input in numerical models, approximations were used for absorption coefficient inputs for the different absorbers. These approximations are plotted in Figure 4.2. The assumed bandgap of CIGS is 1.15 eV (30% Ga/(In+Ga)). For other compositions of Cu(In,Ga)Se$_2$ with different bandgaps, a simple shift (in wavelength) of the curve is a good approximation of α.

Absorber	$\log(\alpha)$ [α in cm^{-1}]	Wavelength range [nm]
CdTe	$5.84 - 0.0018\lambda$	$\lambda < 773$
	$11.40 - 0.0090\lambda$	$773 \leq \lambda < 813$
	$32.54 - 0.0350\lambda$	$\lambda \geq 813$
CIGS ($E_g = 1.15\ eV$)	$5.95 - 0.0015\lambda$	$\lambda < 1000$
	$9.95 - 0.0055\lambda$	$1000 \leq \lambda < 1060$
	$28.50 - 0.0230\lambda$	$\lambda \geq 1060$

4.2 SCR Collection Models

4.2.1 Standard Collection Model

The often-used (and often sufficiently-accurate) collection model that is referred to as 'standard' assumes 100% collection in the SCR. Since the electric field in this region is strong (10^6 V/m), charge separation happens quickly and complete collection is a reasonable assumption. The standard model of space-charge collection is

$$CE_{SCR} = 1. \tag{4.3}$$

4.2.2 The Hecht Equation

Recombination can occur within the SCR, in which case, the standard assumption of perfect collection in the SCR may be insufficient, and alternative treatments may be in order. The Hecht equation describes charge collection in a material with a uniform electric field and with known carrier drift lengths. The equation is used to describe collection in semiconductor X-ray spectrometers [57], and can also serve as an approximation for charge collection within the SCR of a thin-film solar cell [58, 59, 60]. The charge collection efficiency is given by the Hecht equation as

$$CE_{SCR}(x) = \frac{\ell_p}{W}[1 - exp(-\frac{W-x}{\ell_p})] + \frac{\ell_n}{W}[1 - exp(-\frac{x}{\ell_n})], \tag{4.4}$$

where $\ell_{n,p}$ is the mean drift length of electrons (n) or holes (p). Note that the mean drift length is the average distance traveled by a carrier before recombination occurs, not the mean distance between collisions (mean free path). The mean drift length is related to the electric field $\vec{E}$, mobility μ, and lifetime τ by

$$\ell = \mu|\vec{E}|\tau. \tag{4.5}$$

Time-resolved photoluminescence (TRPL) measurements by Metzger *et al.* indicate lifetimes in CdTe are in the range 0.01–1 ns [61]. For usual values of μ and $\vec{E}$, and τ, the drift length for electrons is on the order of 0.1–10 μm. The drift length for holes is approximately 100 times longer, due to differences in lifetimes and mobilities for electrons and holes.

Treatment of Hecht collection by Kosyachenko [59] neglects the different lifetimes of holes and electrons. Hole and electron lifetimes are likely to be different due to their different populations in the absorber and the different capture-cross-sections of donor-like defects for electrons and holes. The claim made in that work is that $\mu_n\tau_n > \mu_p\tau_p$ always, since $\mu_n > \mu_p$. This leads to hole-limited collection near the front of the device, and maximum collection efficiency near the space-charge edge (buried in the device). Using these assumptions to calculate QE curves results in curves unlike those measured experimentally. By increasing hole lifetime by a factor of 1000 relative to electron lifetime, I find that Hecht collection results in more realistic QE curves. The increased hole lifetime is consistent with what should be expected in the absorber of an operating device, where the concentration of holes greatly exceeds the concentration of electrons. Results are not sensitive to the exact factor by which hole lifetimes exceed electron lifetimes, since for hole lifetimes longer than 1 ns, hole drift lengths are the order of the device thickness or longer.

The electric field is not constant in the depletion region, but decreases linearly with depth into the absorber as

$$E(x,V) = \frac{2(V_{bi} - V)}{W}(1 - \frac{x}{W}). \tag{4.6}$$

At $V = 0$,

$$E(x) = \frac{qN_A}{\varepsilon_s}(W - x) \tag{4.7}$$

utilizing the one-sided abrupt junction approximation $V_{bi} = \frac{qN_A W^2}{2\varepsilon_s}$ from Equation 2.10. Here N_A is the carrier concentration in the absorber, V_{bi} is the built-in voltage and ε_s is the dielectric constant in the absorber. For carriers generated at position x within the SCR, the electron sees a larger average electric field than the hole. For simplicity, the electric field seen by each carrier is represented by the average value of the electric field in the region traversed by that carrier. So,

$$E_n(x) \simeq \frac{E(0) + E(x)}{2} = \frac{qN_A}{2\varepsilon_s}(2W - x) \; and \; E_p(x) \simeq \frac{E(x)}{2} = \frac{qN_A}{2\varepsilon_s}(W - x), \tag{4.8}$$

for the electron and hole generated at x. E_n is used when determining ℓ_n from Equation 4.5, and E_p is used for ℓ_p. In Figure 4.3, E_n and E_p are shown for an electron and hole generated at $x = 1.75$ μm within a 2.4 μm SCR in a CdTe device.

4.2.3 Simple Drift Model

Seeking an alternative to the Hecht collection model, first note that the probability that a photogenerated electron will travel a distance between x and $x + dx$ before recombining is $P(x) = (1/\ell)e^{-x/\ell}dx$, where ℓ is the mean drift length. The probability of a carrier traveling *at least* as far as x' is

$$P(x \geq x') = \int_{x'}^{\infty} \frac{1}{\ell} e^{-x/\ell} dx = e^{-x'/\ell}. \tag{4.9}$$

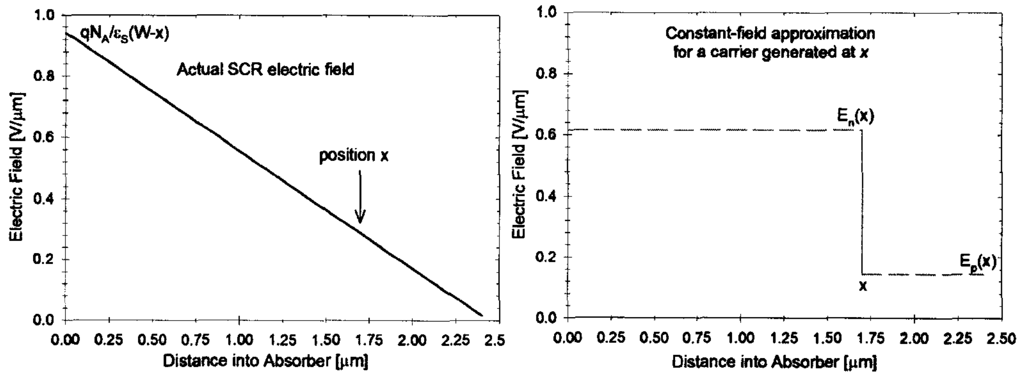

Figure 4.3: On the left, the actual electric field within the space-charge region $\mathrm{E(x)}$ is shown in a typical CdTe device with space-charge width $\approx 2.4\ \mu$m. An electron and hole generated at x see different average electric fields, shown at right. The electron sees an average field $\mathrm{E_n(x)}$, which is larger than the average hole field $\mathrm{E_p(x)}$. These fields are used with Equation 4.5 to determine the mean drift length of holes and electron generated in the SCR. Since the average field depends on the depth of generation, deep-generated carriers have shorter drift lengths than shallow generated carriers.

For an electron generated at x, the probability that it will travel as far as the metallurgical junction is

$$CE_{SCR}(x) = e^{-x/\ell_n}. \tag{4.10}$$

The simple drift model assumes perfect collection of holes throughout the device.

4.3 Neutral Region Collection Models

In devices that are not fully depleted, some absorption will occur in the neutral region. Collection is poorer in this region since no electric field is present to separate carriers. Neutral region collection is described by the following treatments.

4.3.1 Simple Diffusion

The absorber material in thin-film devices is p-type, so the diffusion current is limited by the diffusion of electrons to the SCR (and not limited by hole diffusion). For depletion thickness W, the probability of this occurring is

$$CE_{Neut.}(x) = e^{-(\frac{x-W}{L_n})}, \tag{4.11}$$

where L_n is the diffusion length of the electron and depends on temperature (T), mobility (μ) and lifetime (τ) as $L_n = \sqrt{\frac{k_B T \mu_n}{q}\tau_n}$. At room temperature, electron diffusion lengths for thin-film materials are typically less than one micron, and are usually shorter than the electron drift length ℓ_n.

4.3.2 Surface Recombination

A valuable correction to the simple diffusion model is the inclusion of back surface recombination. At the back surface of the absorber layer, the interface between semiconductor and metal results in dangling bonds. These dangling bonds introduce mid-gap states into the material which serve as recombination centers. The effect of these states is to impose a boundary condition on the collection function at the back contact [62]. The surface recombination velocity S describes recombination at the back contact. A typical value for S is 10^7 cm/s, the thermal velocity of carriers—that is to say all carriers which reach the back contact recombine. The consideration of back surface recombination changes the field-free collection function to

$$CE_{Neut.}(x) = \frac{\cosh\frac{D-x}{L_n} + \frac{SL_n}{D_n}\sinh\frac{D-x}{L_n}}{\cosh\frac{D-W}{L_n} + \frac{SL_n}{D_n}\sinh\frac{D-W}{L_n}}, \tag{4.12}$$

where D is the device thickness, and $D_n = \frac{k_B T \mu_n}{q}$ is the electron diffusion coefficient. The effect of including surface recombination is shown in Figure 4.4. For surface recombination velocity of 0 cm/s, Equation 4.12 approximates the simple diffusion relation in Equation 4.11. The inclusion of back surface recombination improves agreement of calculations with experimental results, most notably for illumination from the back side (as should be expected, since in that situation many carriers are present at the back contact). In most

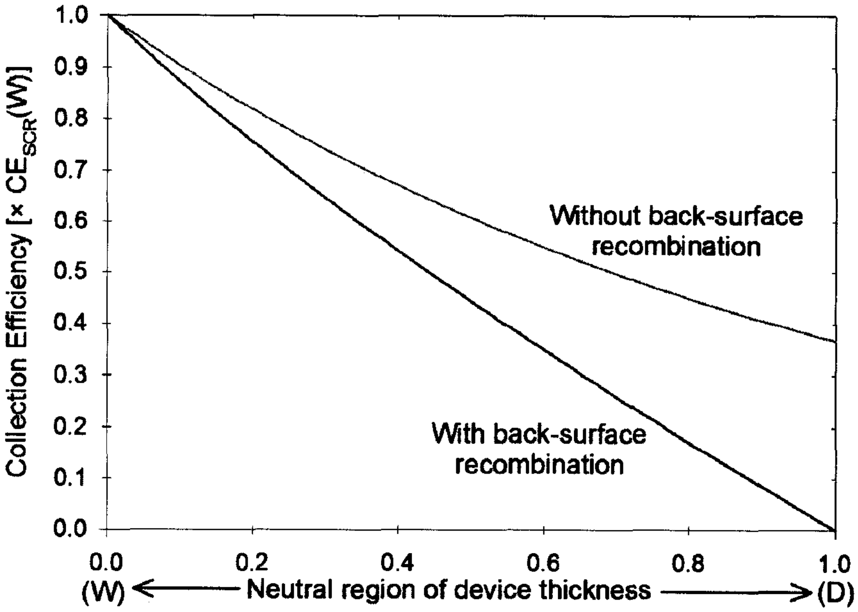

Figure 4.4: Back surface recombination reduces collection of carriers generated at the back contact. In this example, representative of a CdTe device: D = 5 μm, W = 4 μm, S = 10^7 cm/s, L_n = 1 μm, and D_n = 10 cm^2/s.

cases, back surface recombination does not strongly affect J_L for front illumination, since few carriers are generated near the back surface.

4.4 Evaluation of Collection Models

Calculation of QE from collection models is done by evaluating the expression

$$QE = \int_0^W Gen(x,\lambda)CE_{SCR}(x)dx + \int_W^D Gen(x,\lambda)CE_{SCR}(W)CE_{Neut.}(x)dx, \qquad (4.13)$$

for chosen collection models CE_{SCR} and $CE_{Neut.}$. Equation 4.13 is valid in the regime $\lambda > 500$ nm. For wavelengths shorter than 500 nm, CdS absorption must be considered. The entire QE curve could be evaluated by determining the fraction of incident short-wavelength photons transmitted through the CdS layer ($E_g = 2.4$ eV, $\lambda_g \approx 500$ nm) and applying the SCR collection model to those photons. It is generally assumed that due to the

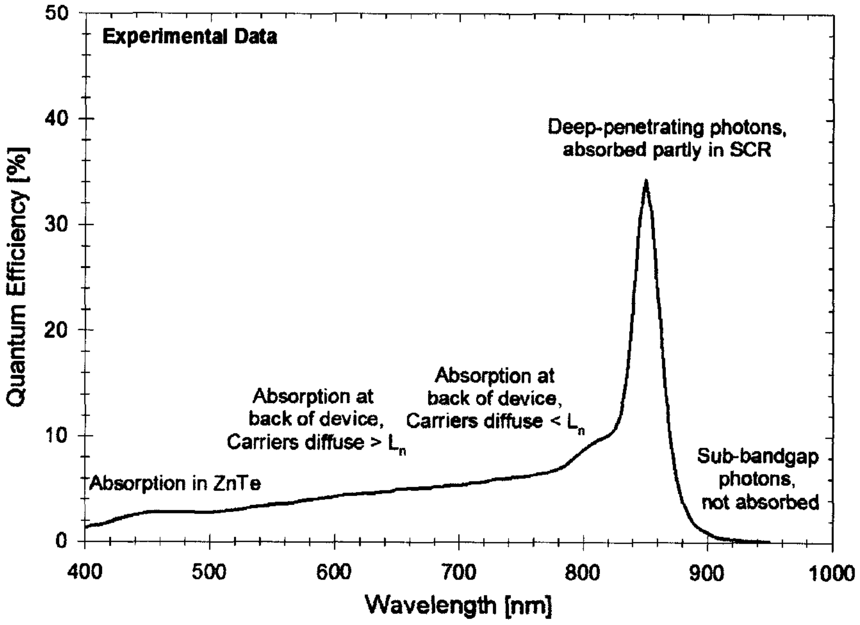

Figure 4.5: All back-side QE measurements show similar features, shown in this data from a CdTe device with an ITO back contact. In the limit of thin absorbers, back-side QE converges with the front-side result.

large number of hole traps in CdS (models suggest $\sim 10^{18}$ cm^{-3}), none of the holes generated in CdS contribute to the photocurrent. This is the fundamental reason we desire thin CdS layers. When Equation 4.13 is difficult to evaluate analytically (such as when using the Hecht equation and surface recombination function), numerical methods are used.

4.4.1 Introduction to Back-side QE

Quantum-efficiency measurements through the transparent back contacts of devices will be discussed in Chapter 5, although a brief introduction is in order here. QE through a transparent back contact is a useful tool for evaluating device physics, since it allows SCR collection and neutral-region collection to be studied separately. To investigate illumination from the back surface, make the substitution $x \rightarrow (D - x)$ in the generation function (Equation 4.2). Figure 4.5 shows typical features observed in QE measurements with back-side illumination on a CdTe device. As generation occurs closer to the front of the device (higher photon wavelengths), the collection efficiency improves. For photons which reach the SCR, collection improves dramatically, resulting in a peak in the QE curve for photon-energies just above the absorber bandgap. The exact shape of the curve depends on the width of the space-charge region and the diffusion length of carriers in the material.

4.4.2 Summary of Models

In Figure 4.6, QE curves are displayed which were calculated from the collection models in Table 4.2. Back-side QE curves are also shown here. Reflection is ignored in these curves, so it is internal quantum efficiency that is shown. Still, the Standard model produces unrealistically large quantum efficiencies, particularly for the deep penetrating photons near 800 nm, so this model will not be discussed further here. The Hecht and Simple Drift models result in more realistic QE curves. The curves in Figure 4.6 assume a CdTe absorber of thickness 2 μm, carrier concentration 5×10^{14} cm^{-3}, baseline mobilities as given in Table 2.1, electron lifetime 0.1 ns, and hole lifetime 100 ns.

Table 4.2: A summary of the collection models used in this work, and the names used to describe them.

Model	SCR Collection	Neutral Collection
"Standard"	1	$\frac{\cosh\frac{D-x}{L_n}+\frac{SL_n}{D_n}\sinh\frac{D-x}{L_n}}{\cosh\frac{D-W}{L_n}+\frac{SL_n}{D_n}\sinh\frac{D-W}{L_n}}$
"Hecht"	$\frac{\ell_p}{W}(1-e^{-\frac{W-x}{\ell_p}})+\frac{\ell_n}{W}(1-e^{-\frac{x}{\ell_n}})$	$\vdots$
"Simple Drift"	e^{-x/ℓ_n}	$\vdots$

In Figure 4.7, the realistic collection models from Figure 4.6 are compared for a range of lifetime values. Hole lifetimes are maintained 1000 times larger than electron lifetimes. The electron lifetime is varied from 0.01 ns to 1 ns. For long carrier lifetimes, the models nearly coincide. For short electron lifetimes the models differ significantly, with the Hecht model predicting higher collection than the Simple Drift model.

The models chosen here for comparison were chosen because of their prior use in literature (Standard [63], and Hecht [59]), and the need for an improved, intuitive description

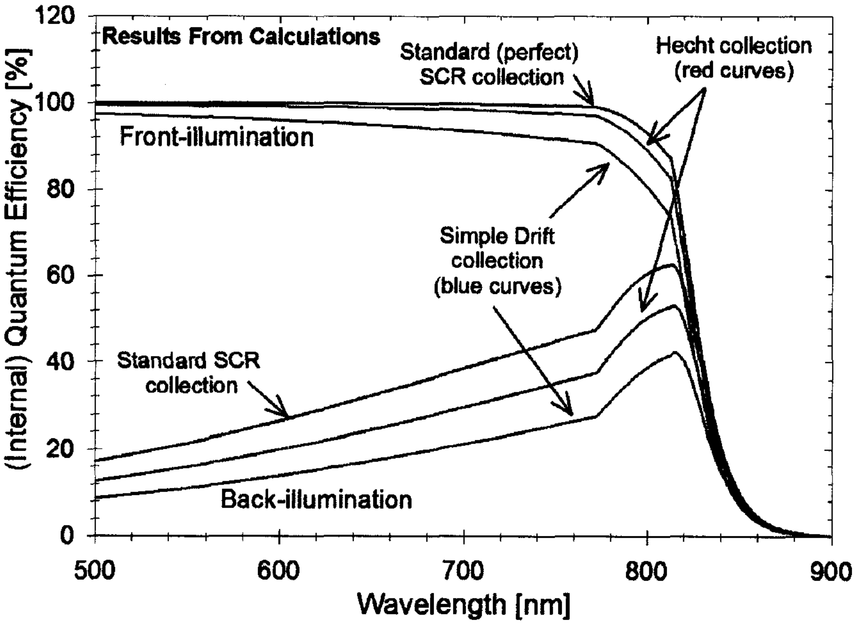

Figure 4.6: Front- and back-side QE curves are calculated based on the collection models discussed in Table 4.2. The following parameters are used in the collection models: Zero Reflection, D = 2 μm, p = 5×10^{14} cm^{-3}, $\mu_e = 320$ cm^2/Vs, $\mu_h = 40$ cm^2/Vs, $\tau_e = 0.1$ ns, and $\tau_h = 100$ ns.

of collection (Simple Drift). It is apparent after comparison with experimental results and numerical simulations that the Hecht equation overestimates carrier collection throughout the space-charge region, thus requiring unreasonably short minority carrier lifetimes are necessary to reproduce experimental data. For this reason, the Hecht model will not be used to explain results in this dissertation. Instead, the Simple Drift model will be used to describe QE results in the remainder of this chapter, and briefly in Chapter 5, as this model has a simple, intuitive form, and can accurately reproduce experimental QE data, given reasonable input parameters.

4.4.3 Comparison with Experiment

The Simple Drift model requires only a few properties of the absorber to be known for a complete calculation of the QE curve. These properties include thickness, carrier concentration, minority-carrier lifetime and minority-carrier mobility. The absorber thickness

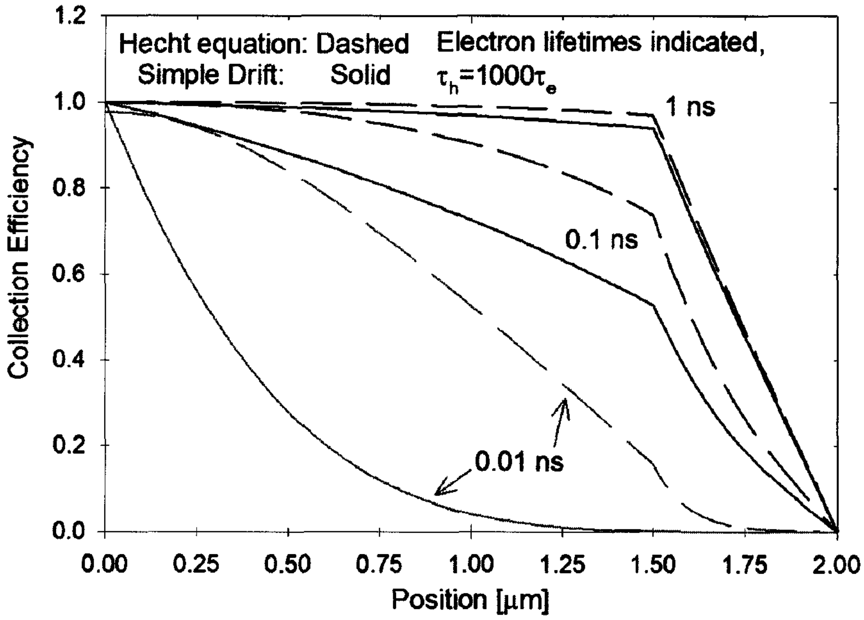

Figure 4.7: A comparison of collection using the Hecht model (dashed curve) and the Simple Drift model (solid curve) for carrier lifetimes varied over three orders of magnitude. Hole lifetimes are 1000 times larger than the electron lifetimes. The two models give similar results for long-lived carriers, and very different results for short-lived carriers. The following parameters are used to generate these curves: D = 2 μm, W = 1.5 μm ($N_A = 5 \times 10^{14}$ cm^{-3}), mobilities as in Table 2.1.

is generally known, either directly from the device manufacturer, or inferred from C-V measurements. The carrier concentration value is obtained by C-V measurements. Carrier mobilities and lifetimes are known approximately for the polycrystalline materials used in thin-film photovoltaics. External QE can be reconstructed if the reflection spectrum is known, as it generally is from direct measurements. After inputting all device parameters into the collection model, we can reconstruct a QE curve and compare this curve with an experimental QE curve, adjusting the model results by maintaining well-known parameters and varying less-well-known parameters. This work takes the approach that those parameters directly measured are considered well-known, that the carrier mobilities are well-known, and that the minority-carrier lifetimes are less-well-known. For each model, this only leaves a single ‘fitting parameter’—the electron lifetime.

Three CdTe absorbers prepared by close-spaced sublimation at the Materials Engineering Laboratory at CSU were used to test collection efficiency models. The absorber layers were nominally 2 μm thick. The devices were finished at the U.S. National Renewable Energy Laboratory with ZnTe:Cu/Ti back contacts by Gessert *et al.* [64]. Devices then had a portion of the Ti metallization removed by a chemical etch so that the transparent ZnTe was accessible for back-side illumination studies. In addition to its use as a transparent contact, ZnTe has also been suggested as a suitable material for back contacts in CdTe devices for another reason. The conduction band offset at the p-CdTe/ZnTe interface should act as an electron reflector, thereby minimizing back contact recombination [65]. Where ZnTe is intended as an electron reflector, an opaque metallic back contact is usually present behind the ZnTe layer since the electron-reflector benefits do not require back illumination. Capacitance measurements indicated actual absorber thicknesses of 1.65–1.75 μm and p-type carrier concentrations of 5–10 × 10^{14} cm^{-3}, as shown in Figure 4.8.

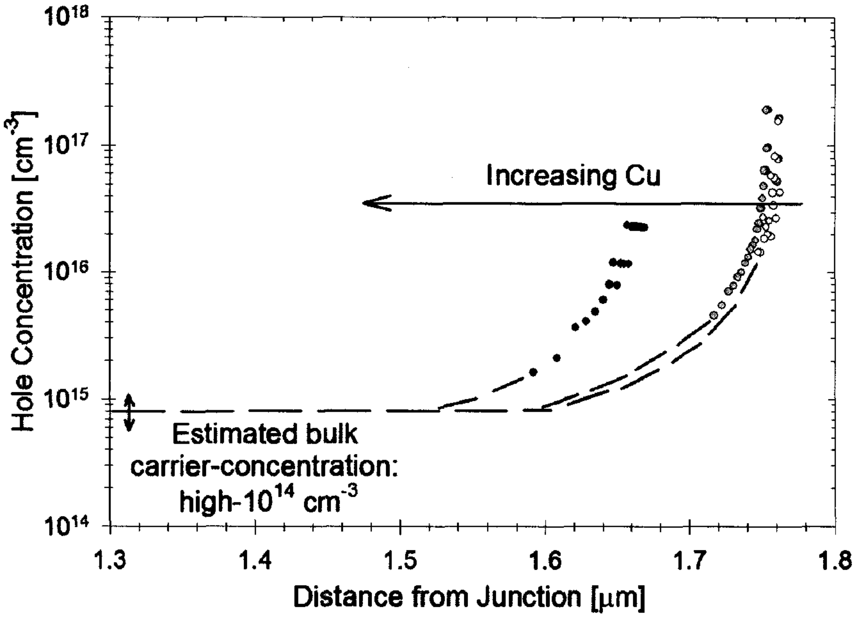

Figure 4.8: Capacitance measurements on the CSU devices indicate bulk carrier concentrations in the high-10^{14} cm^{-3} range, and absorber thicknesses of 1.65–1.75 μm.

The three cells studied differed in the amount of Cu which was allowed to diffuse into the device during formation of the back contact. Different temperatures were used in the back contact formation process: 240°C, 320°C, and 360°C. The device contacted at 320°C is referred to as containing "Optimal Cu", because it is empirically the best-performing device in the study. The device contacted at 240°C is said to contain "Low Cu", and the 360°C device is said to contain "High Cu". J-V curves from these three devices are shown in Figure 4.9.

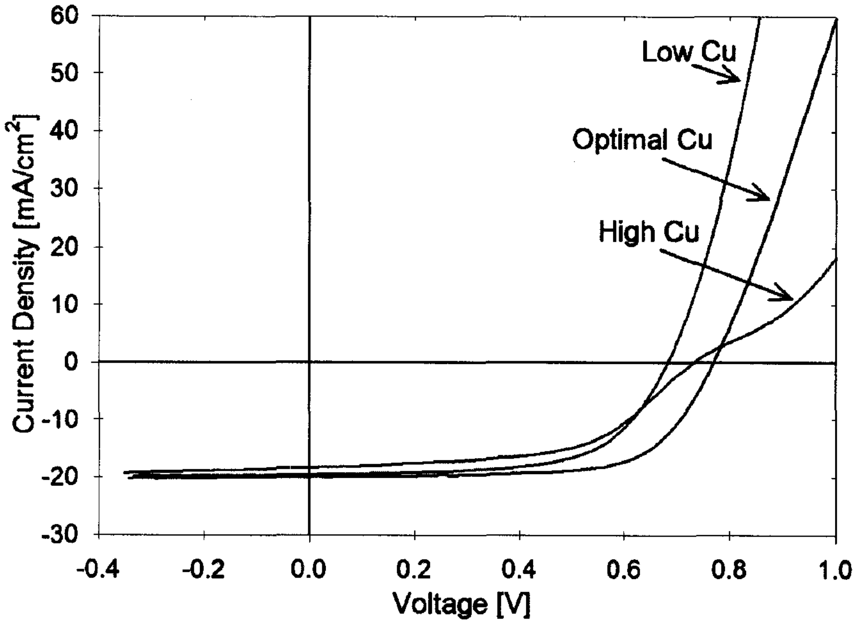

Figure 4.9: Room-temperature J-V curves measured on the CSU cells discussed in Section 4.4.

In Figure 4.10, the results of using the Simple Drift model to explore QE results are shown. For each of the three devices, experimental QE data with front- and back-illumination was plotted within a LabVIEW computer program. Well-known parameters and experimental reflection curves (front and back) were input, and Equation 4.13 was evaluated to generate front- and back-QE curves. Using only electron lifetime to adjust the model, the best fit to the experimental data was found visually. Since capacitance measurements left uncertainty in the value of the bulk carrier concentration present in the devices, two different values of p were used—8×10^{14} and 1×10^{15} cm^{-3}—to observe the sensitivity of results to this parameter. The lifetime determined with the two values of p

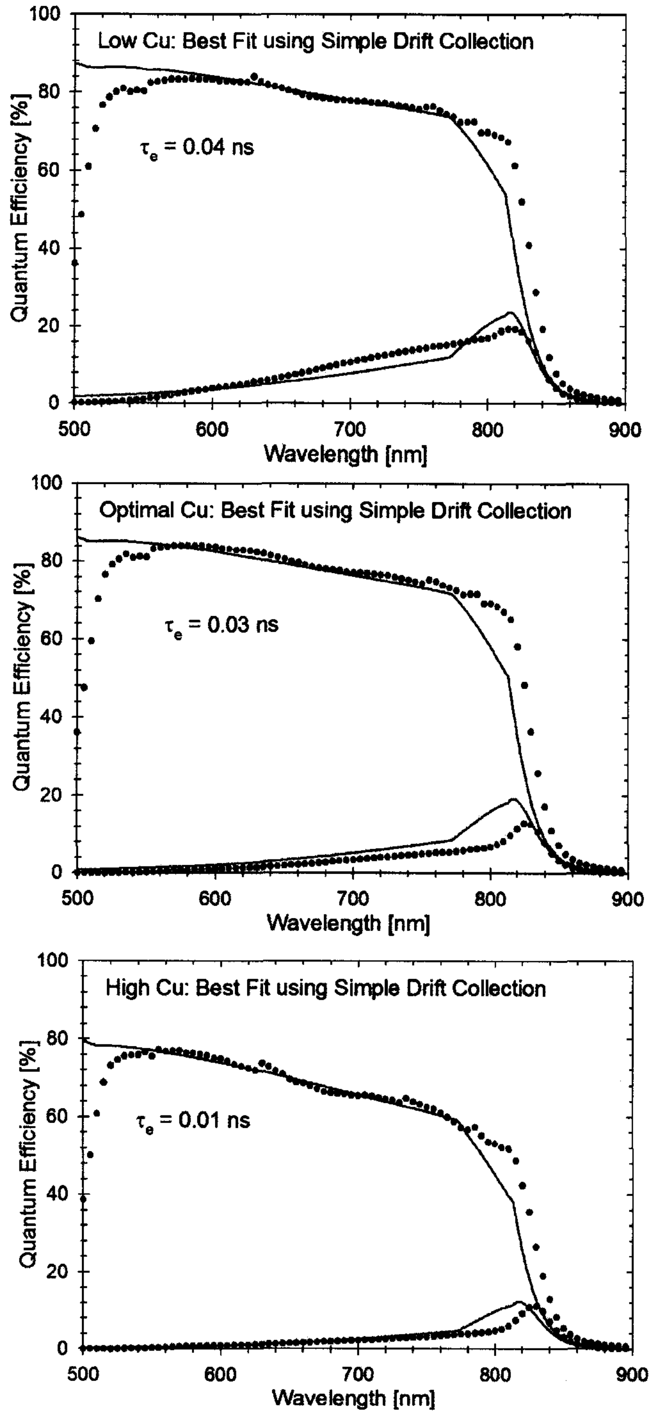

Figure 4.10: For three devices with varying amounts of Cu used in back-contact formation, the Simple Drift model was used to reproduce experimental results. Calculations are plotted with solid lines and experimental data with points. The model is able to account for experimental observations with a small range of realistic electron lifetimes. Identical results were obtained with two different assumed carrier concentrations, 8×10^{14} cm^{-3} and 1×10^{15} cm^{-3} (shown above).

Table 4.3: Summary of minority-carrier lifetime values for the CdTe solar cells studied, as determined from the collection models in this work. Results were unaffected by changes in carrier concentration within the range specified by C-V measurements shown in Figure 4.8.

p [cm^{-3}]	8×10^{14}	1×10^{15}
Low Cu	0.04 ns	0.04 ns
Optimum Cu	0.03 ns	0.03 ns
High Cu	0.01 ns	0.01 ns

were identical, as shown in Table 4.3, though slightly higher-quality fits were obtained with $p = 1 \times 10^{15}$ cm^{-3}.

Calculations result in a higher bandgap energy, by about 20 meV, than is evident from experimental data. The only bandgap information in the calculations is contained in the absorption coefficient approximations of Table 4.1, which agree well with published absorption coefficient results. The experimental curves also are affected by CdS absorption near 500 nm, which is not included in the models. Fits are rather sensitive to the lifetime parameter—that is to say, if $\tau_e = 0.03$ ns results in a good fit, then $\tau_e = 0.035$ ns will result in a noticeably poorer fit. Results are less sensitive to carrier concentration than to lifetime. Uncertainty about the exact functional form of the collection efficiency, however, limits the precision of lifetime determinations.

A trend of decreasing electron lifetime with increasing Cu is evident. This suggests that Cu may form a midgap recombination center in CdTe, a conclusion that will be revisited in Chapter 5. The electron lifetimes which resulted in good fits were shorter than electron lifetimes determined from TRPL measurements on similar devices by less than an order of magnitude. The model was able to accurately reproduce experimental results with a small range of electron lifetimes—0.01–0.04 ns for the range of low-Cu to high-Cu devices.

Chapter 5

Study of Spatial Variations in Quantum Efficiency

In previous chapters, quantum-efficiency measurements were used to identify properties of solar cell devices such as the presence of photoconductivity, band structure, and minority-carrier lifetimes. These techniques used "whole cell" QE measurements—meaning that results are assumed to apply to the entire device area. In this chapter, spatially-resolved quantum-efficiency measurements performed with the LBIC apparatus are used to examine properties that vary within devices on the millimeter-scale and shorter. LBIC measurements prove useful for studying the effects of a broad range of process steps on device uniformity and performance. The results of several such studies are reported here to emphasize the diverse information that is available from these measurements.

5.1 Light-beam-induced Current Apparatus

The LBIC apparatus as discussed in Section 2.2.3 is uniquely suited for measurements of photocurrent uniformity. The details of the apparatus and measurement technique were described in detail by Hiltner [22], though some important features of the experiment will be summarized here.

The major design criteria for the apparatus were: a spatially resolved QE measurement apparatus; diffraction-limited spot size for high-resolution measurements; real-time monitoring of light intensity for accurate QE results; and light intensities comparable to solar intensities. These features allow for study of nonuniform photocurrent collection unavailable in other apparatus. Contrast this with another spatially resolved photocurrent apparatus, the near-field scanning optical microscope (NSOM). NSOM is capable of photocurrent maps with higher resolution (since measurements are performed in the near-field regime), but these measurements have to date required high-intensity light ($\sim$ 100 suns) and so are not as closely related to real-world operating conditions as are LBIC measurements [66].

Three standard resolutions—low, medium, and high—are used to display LBIC data. Low-resolution measurements use a 100-μm spot with 50-μm steps between data points and a usual area of 5000 $\times$ 5000 μm. The output power of the laser diodes limits light intensity to 0.2 sun. Medium-resolution measurements use a 10-μm spot, with 5-μm steps between data points, a 500 $\times$ 500 μm area, one-sun intensity. High-resolution measurements use a 1-μm spot, 0.5-μm steps between data points, 50 $\times$ 50 μm area, and one-sun intensity. Examples of each of these three standard measurement resolutions on one CIGS device are shown in Figure 5.1

5.1.1 Representation of LBIC Data

The standard representation of a photocurrent map (photomap) is a two-dimensional plot which uses eight colors to represent different QE values. For purposes of aesthetics and consistency, the bounds of the color scale are chosen so that green is the dominant color in the photomap. Each color band represents an integer percent range of QE values. A common scheme for representation is a "2%" scale where, for example, the green color may represent areas where the measured QE is 78–80%. A photomap is shown on the left-hand side of Figure 5.2. Unless otherwise noted, the wavelength of illumination is 638 nm.

An alternative representation of LBIC data is the histogram form. Here, the 10,000+

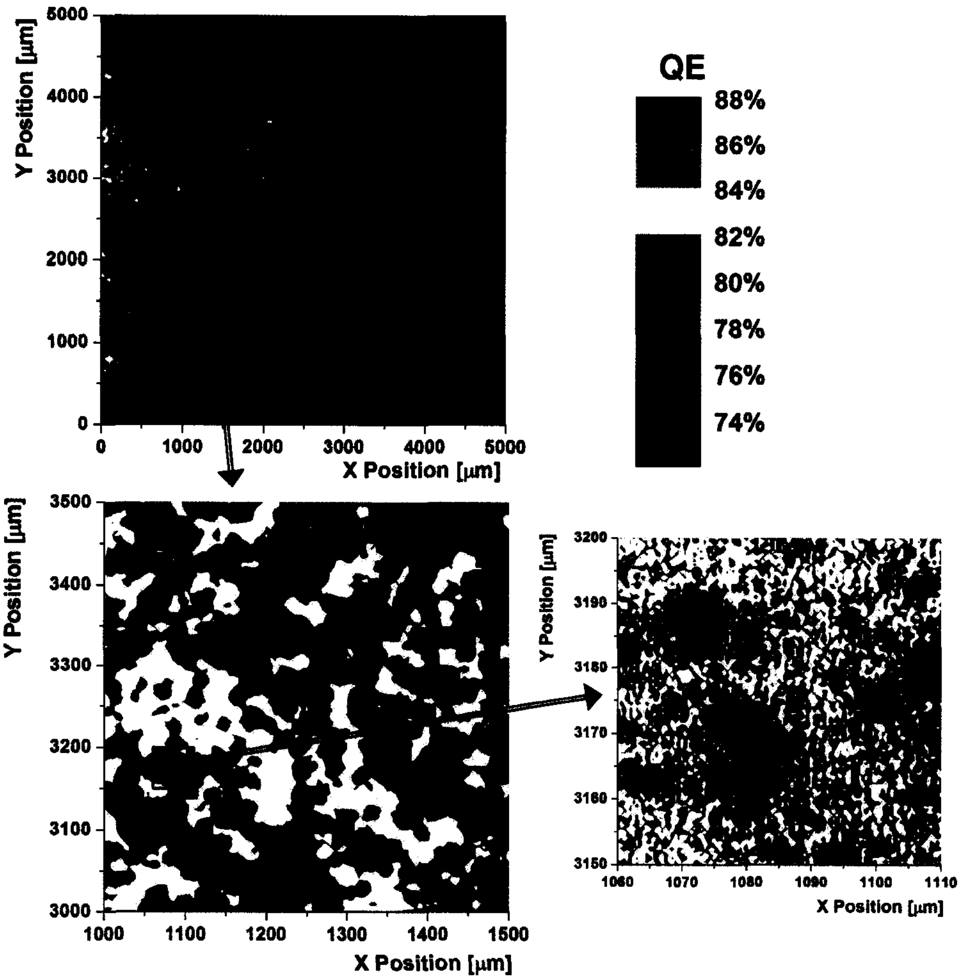

Figure 5.1: Three standard measurement resolutions are shown from the same CIGS device. An area of interest is identified within the low-resolution data (top), and investigated further with medium resolution (bottom left). High-resolution measurements with a diffraction-limited spot size investigate a still-smaller area (bottom right). In the data shown here, the chosen areas of interest are representative of the entire device, rather than pathological features.

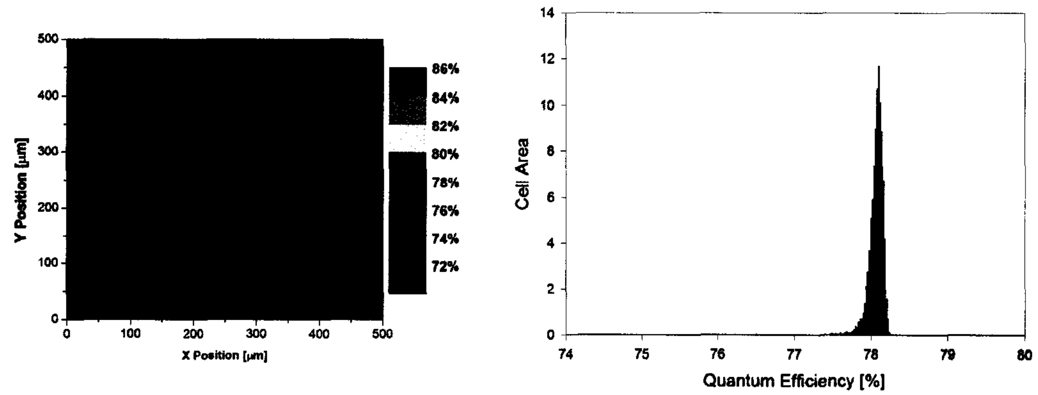

Figure 5.2: LBIC data is equivalently represented by a photomap (left) or a histogram (right).

points in a typical LBIC data set are binned according to their QE value. The result is usually a distribution that can be characterized by the mode and the full-width at half maximum (FWHM) of the peak. A high-photocurrent cell usually has a high (statistical) mode ($> 80\%$), a uniform device has a small FWHM value ($< 2\%$). The desired device has both a high mode and a small FWHM. Since non-idealities in a device usually decrease rather than increase photocurrent collection, the histogram distribution is generally asymmetric, with a longer tail on the low-QE side of the distribution. A example of such a histogram is shown on the right-hand side of Figure 5.2.

Note that in Figure 5.2 virtually the entire range of QE data shown lies between 77% and 79%, so that with careful choice of color scale the device represented could be made to appear more uniform (if green covered the range 77–79% rather than 78–79%). In this sense, histograms are a less ambiguous method of summarizing LBIC data than photomaps. On the other hand, photomaps are "easier to look at" and often convey information about device uniformity in a more straightforward manner. It is worth noting, however, that the aesthetic value of a photomap comes at the cost of some discarded information. The lesson is that one should use great care in plotting or viewing photomaps, that important information is not hidden from view.

In light of concerns that the conclusions a reader might draw about a cell's uniformity

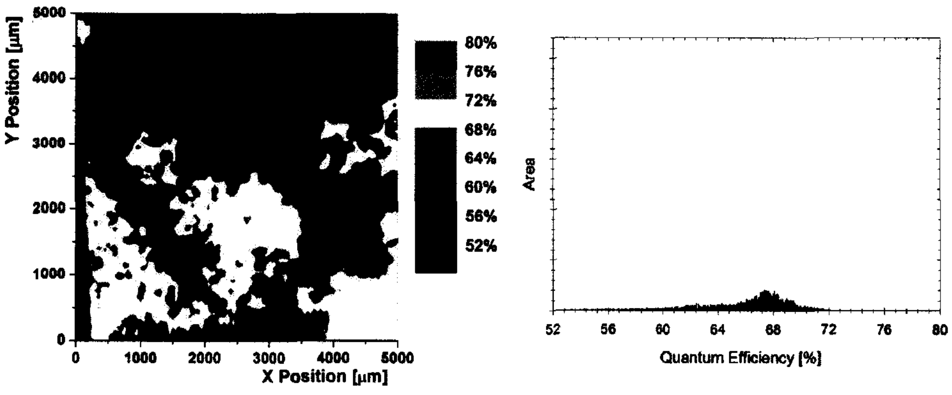

Figure 5.3: This CdTe device demonstrates tier-III device uniformity. Local QE ranges from 54–72%.

may be influenced by the scale chosen to plot the LBIC data, it is useful to categorize devices within three tiers of uniformity. Tier-III: Nonuniform devices vary by more than relative-20% across a one-mm distance scale, as shown in Figure 5.3. These large-scale nonuniformities are sometimes caused by a variation of a deposition parameter throughout the device area—such as layer thickness, or could be caused by a local shunt—which is easily recognizable by a funnel-shaped QE profile (Section 5.3). In general, tier-III devices suggest that some step in the fabrication procedure is poorly controlled, or that layers have degraded from their initial states (*e.g.* of composition) due to outside factors, usually heat, moisture, and age (often referred to collectively as “stress”). Tier-II: These devices are relatively uniform on the one-mm distance scale, but have some variations on the micron scale, as demonstrated in Figure 5.4. These devices require at least a 3% color scale for presentation. A histogram of the LBIC data shows a peak with FWHM of at least 3–5%. Tier-I: These devices are uniform on both the millimeter and micron distance scales. LBIC photomaps use a 2% or finer color scale for display. Histograms show a sharp peak with FWHM less than 3%. A tier-I device is shown in Figure 5.5. Even here, however, small local areas of reduced QE are not uncommon. The application of stress can cause a device to degrade from a tier-I device to a tier-II or tier-III device, as will be discussed in Section 5.5.

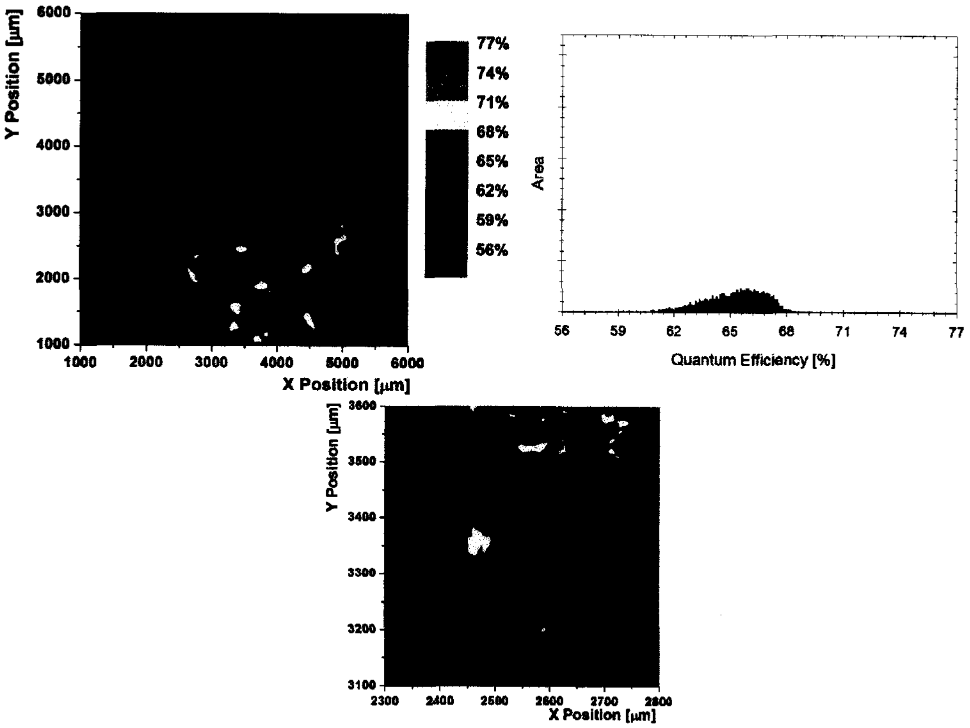

Figure 5.4: This CdTe device demonstrates tier-II device uniformity. Local QE ranges from 60–68%.

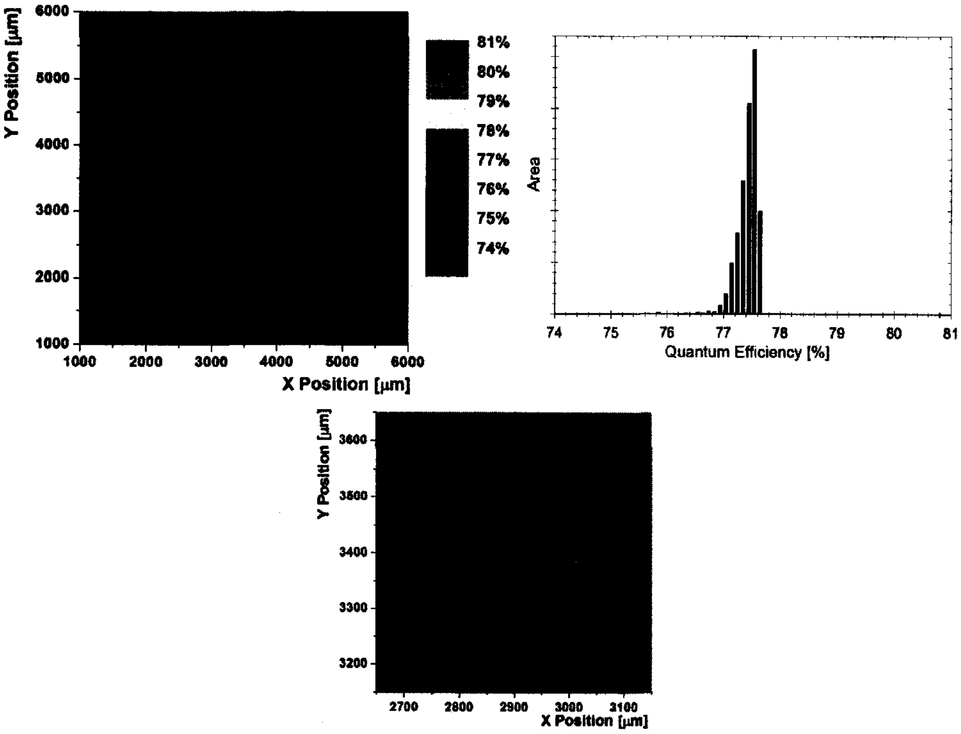

Figure 5.5: This CdTe device demonstrates tier-I device uniformity. Nearly the entire device has QE 77–78%.

5.2 Optical Variations

Optical features are one source of nonuniform photocurrent collection. Optical effects encompass all features which prevent absorption of light, including gridlines, scratches, and surface reflections. The reflection-monitor photodiode shown in the LBIC schematic (Figure 2.8) collects a fraction of specularly reflected light, allowing for a spatially-resolved reflection measurement. The fraction of reflected photons collected by the monitor photodiode is roughly 3% of the total reflection. Figure 5.6 shows an example of nonuniform photocurrent caused by optical nonuniformities in a crystalline silicon device. Areas of low photocurrent response are very well correlated with areas of high reflectivity. In this case, after the reflection measurements are scaled to account for the poor efficiency of collection of reflected photons, the electrical properties of the cell are quite uniform. That is to say, the internal QE is uniform, while the external QE is not.

In thin-film devices, reflection is much more uniform, so that nonuniform QE in CIGS and CdTe devices is usually caused by electrical effects. Figure 5.7 shows LBIC results and spatially-resolved reflection on a CIGS device. The front gridlines are apparent in the uncalibrated reflection photomap, but no other correlation is visible between areas of low photocurrent in the LBIC data and areas of high reflection. In this case, both internal and external QE are rather uniform.

5.3 Shunt-type Defects

Decreased shunt resistance harms device performance by reducing fill-factor. In some cases the shunt paths that cause these effects are localized and able to be identified with LBIC measurements. Common locations of such shunt paths are near (or under) a gridline, or around the perimeter of a cell. The classic signature of a shunt is a small feature which affects photocurrent collection over a large area, and an effect that is very nearly circular, as shown in Figure 5.8. The circular shape of shunt effects arises because the magnitude of the reduction of photocurrent depends on the lateral resistance between photocurrent

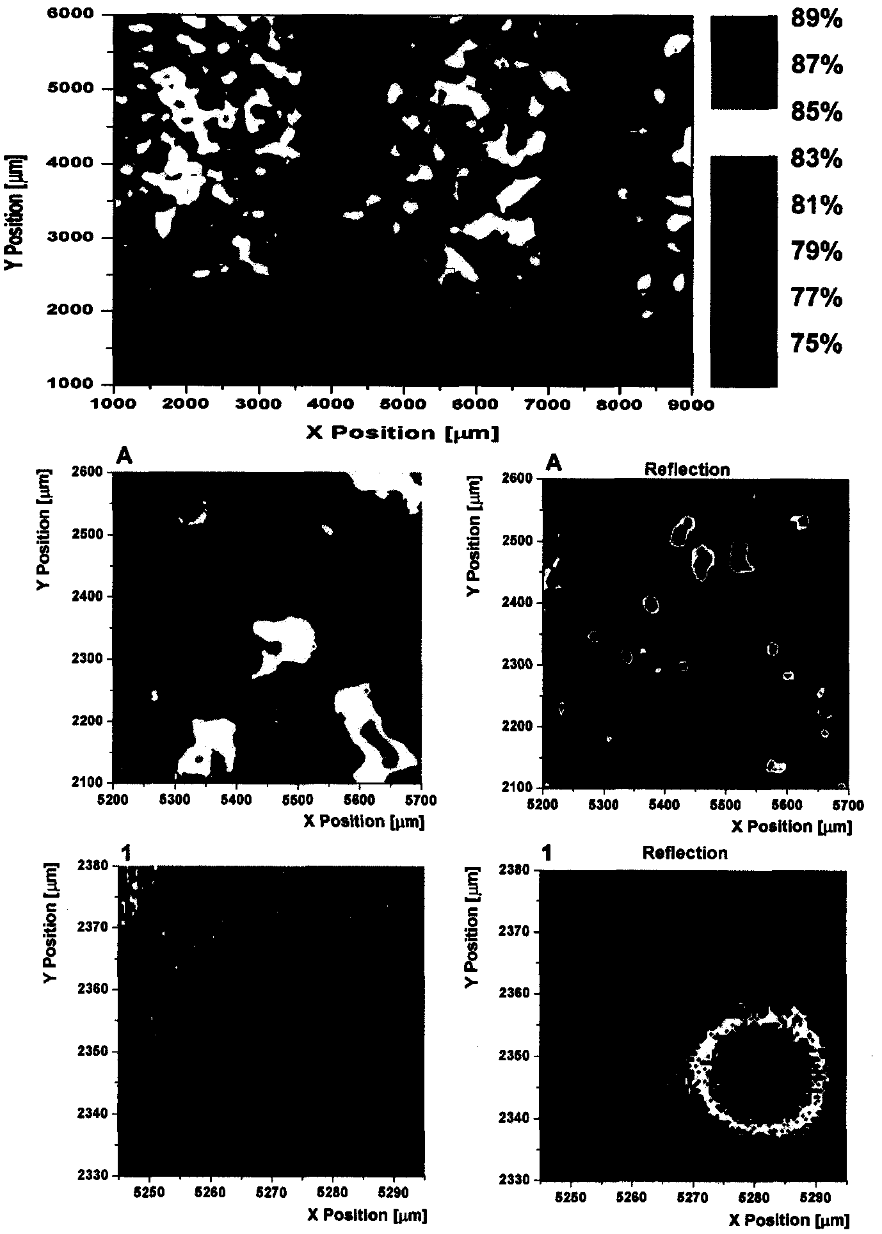

Figure 5.6: In a crystalline silicon device, optical effects are clearly a major cause of photocurrent nonuniformity. Spatially resolved reflection measurements show that reflection is high (right) where photocurrent is low (left). Areas in red in the reflection plots correspond to ~ 10% reflection from the surface.

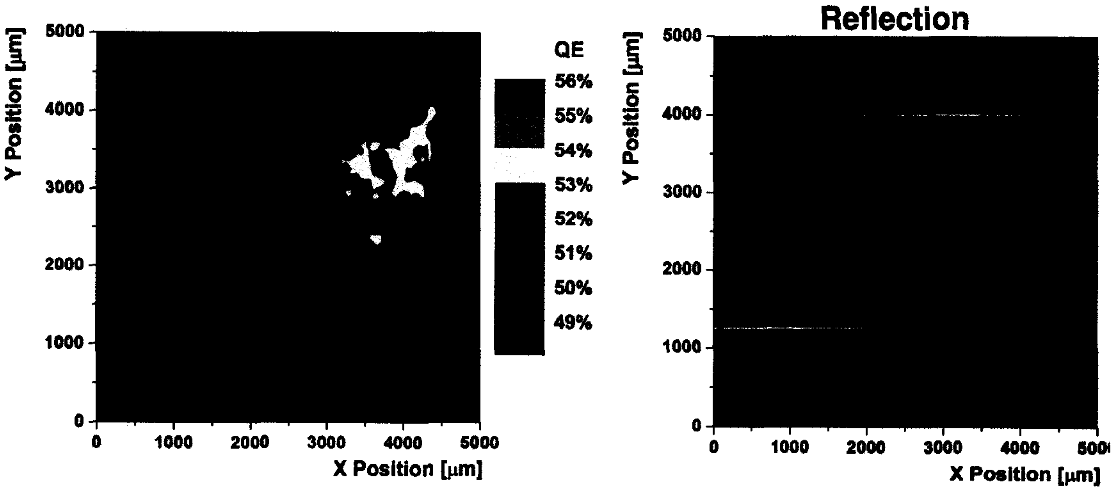

Figure 5.7: On this CIGS device, and on thin-film devices in general, optical effects are not a major cause of photocurrent variations. Here, aside from gridlines, there is no spatial correlation between reflection and photocurrent measurements.

generation and the location of the shunt, usually determined by the sheet resistance of the TCO layer. In the example shown in Figure 5.8, the effect is elongated slightly in the x-direction, parallel to the low-resistance grid lines.

In the course of LBIC studies on shunted cells, it became desirable to induce a shunt in an otherwise well-behaved device. One case where this is possible is in CIGS cells deposited on flexible (molybdenum or stainless-steel) substrates. By cutting such a device across a gridline with scissors, the cut gridline is often folded over into contact with the back contact, creating a shunt path in parallel with the junction. A sketch of this process is shown in Figure 5.9. LBIC results on such a device show extremely low photocurrent collection, and the size of the effect is strongly dependent on the series resistance between the localized shunt and the localized generation, as shown in the left-hand photomap of Figure 5.9. Subsequently, the gridline in this location was dissolved away with a cotton swab and acetone to remove the shunt path. The device was re-measured with the LBIC apparatus, and photocurrent had recovered considerably, as shown in the right-hand photomap of Figure 5.9.

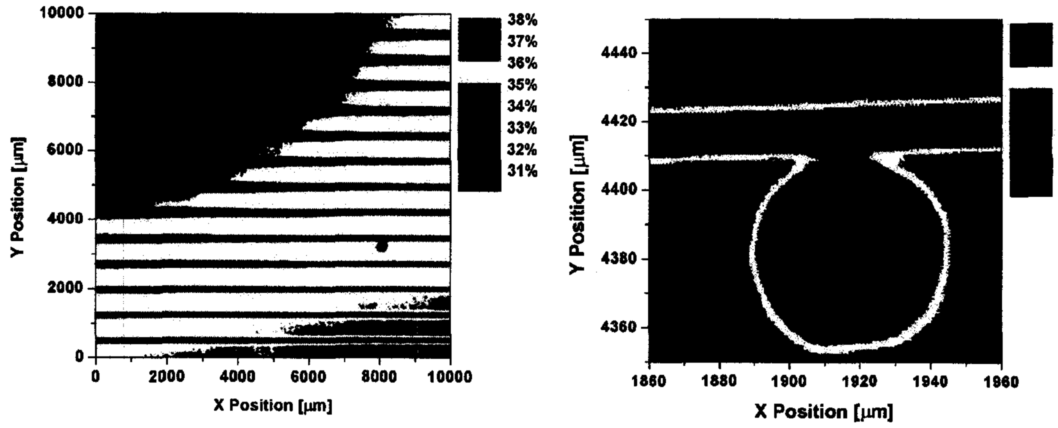

Figure 5.8: In this (non-thin-film) photovoltaic device, a small (50 μm diameter) shunt is located near a gridline. The effect of the shunt is to reduce photocurrent collection over a large area (2 cm dia.). The normally circular effect is slightly elongated in the x-direction due to the low-resistance grid lines. The circular nature of shunt-type effects holds true for thin-film devices as well.

5.3.1 High-resistance TCO Layers

One processing step that is used to prevent the formation of shunt-type defects is the inclusion of a high-resistivity TCO (HRT) layer. CdTe solar cells with HRT layers are more uniform (and better-performing) than devices without the high-resistivity layer [38]. Since the HTR layer is expected to improve solar cell uniformity, LBIC is well-suited to evaluate HRT effects.

Devices for a study on the effects of HRT layers were fabricated at the Colorado School of Mines (CSM) by vapor-transport deposition [67]. Some of the devices contained a single layer of SnO_2 as a front contact, while others contained a bilayer TCO: the standard SnO_2, plus an intrinsic SnO_2 layer (the HRT) between the low-resistance SnO_2 and the CdS layer. Figure 5.10 shows LBIC data from two devices, with and without an HRT layer. The device with the HRT layer shows better uniformity and higher photocurrent than the device without the HRT layer, demonstrated by photomaps and histograms.

The high-resistance layer likely improves uniformity and performance for two reasons. First, the high resistance layer reduces the shunt conductance through any pinholes which

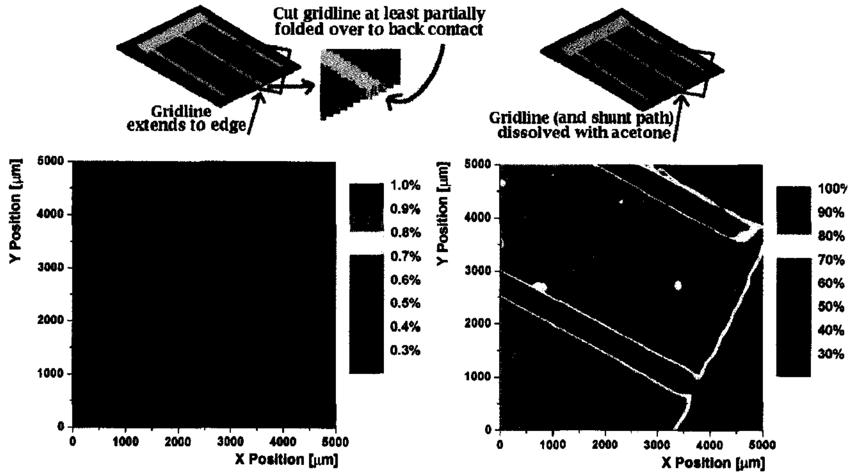

Figure 5.9: On a CIGS device deposited on a flexible substrate, a local shunt was created by cutting the device across a gridline. LBIC results showed that photocurrent was extremely low and strongly position-dependent. The offending area was rubbed with acetone to dissolve the shunt path and photocurrent recovered.

may be present in the thin CdS. Second, the high-resistance TCO isolates weak diodes and reduces their effects throughout the device as shown by Kanevce [68].

5.4 LBIC Bias Dependence

In the same way that whole-cell QE measurements can be performed in forward bias, with care, LBIC measurements can be performed at non-zero applied bias. This allows us to explore voltage-dependent collection with spatially-resolved techniques. Similarly to light-biased whole-cell QE measurements discussed in Chapter 3, care must be taken to subtract the DC component of the current (due to forward current) from the AC photocurrent. The electronics used in the measurement limit the range of measurement to below V_{OC} in most cases.

Two CIGS devices were measured which had J-V curves indicating different current collection at small forward biases, shown in Figure 5.11. These devices use ZnS buffer layers instead of CdS, resulting in a large conduction band offset relative to most CIGS devices. The intentional fabrication difference between these devices was gallium con-

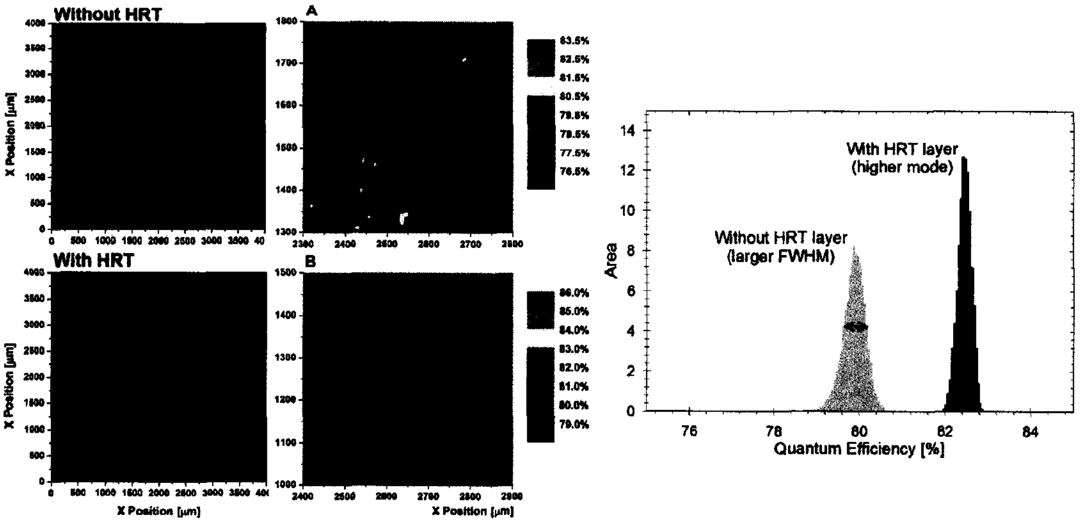

Figure 5.10: LBIC results show that the CdTe device with an HRT layer is more uniform, as demonstrated in the histogram plot. The HRT device has a higher mode value (its photocurrent performance is higher) and lower FWHM value (it is more uniform). Some physical damage due to probing the back contact is apparent in both devices.

tent [69]. The cell with the strongly distorted J-V curve has lower Ga content (therefore slightly lower absorber bandgap, and slightly larger conduction band offset) than the other cell. This results in a barrier to photogenerated electrons in the low-Ga device.

LBIC measurements were performed over a small range of biases (below V_{OC}), where there is a clear difference in J-V behavior. Between 0 mV and 200 mV the cell with the conduction band barrier shows voltage-dependent collection (Figure 5.11), while the "well-behaved" cell does not. The results from forward-biased LBIC measurements are shown in Figure 5.12. In the medium-resolution field of view, both devices are relatively uniform at 0 V. With increasing bias, the cell with the conduction band barrier shows strongly nonuniform collection effects. This suggests that the effects of conduction band barriers, such as those that occur here with a low-bandgap absorber and ZnS window layer are nonuniform.

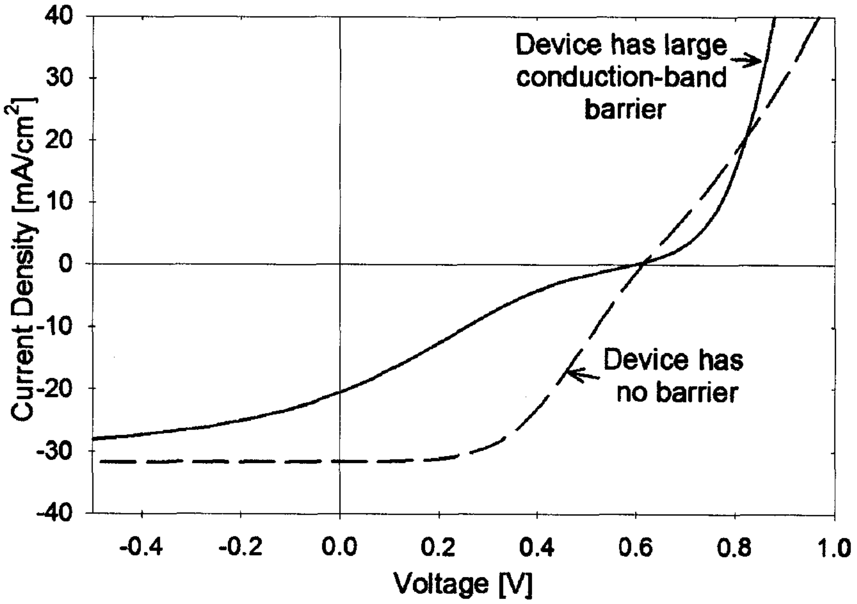

Figure 5.11: J-V curves of two CIGS devices indicate the presence of a conduction band barrier in one device (solid curve).

5.5 Degradation Tracking

Solar cell performance often degrades over time, in response to physical and chemical stresses. High temperatures such as those the device experiences during operation (as high as 60°C on a bright summer day) are a common cause of such deterioration. At high temperatures, the thermal kinetic energy increases the rate of diffusion of atoms throughout the semiconductor layers. As an example, one expected mode of degradation is for copper atoms which are desired at the back contact to diffuse along grain boundaries to the main junction, where they act as mid-gap recombination centers.

In Figure 5.13, low-resolution LBIC results are shown on a CdTe cell before and after periods of "stress" (here *stress* is defined as exposure to high temperature and light intensity), to simulate the degradation expected to occur after years of use in the field. The conditions of stress were 100°C, several suns light intensity, with the device held at short circuit.

Initially, the cell shown in Figure 5.13 is a tier-I device, with only 2–3 very small

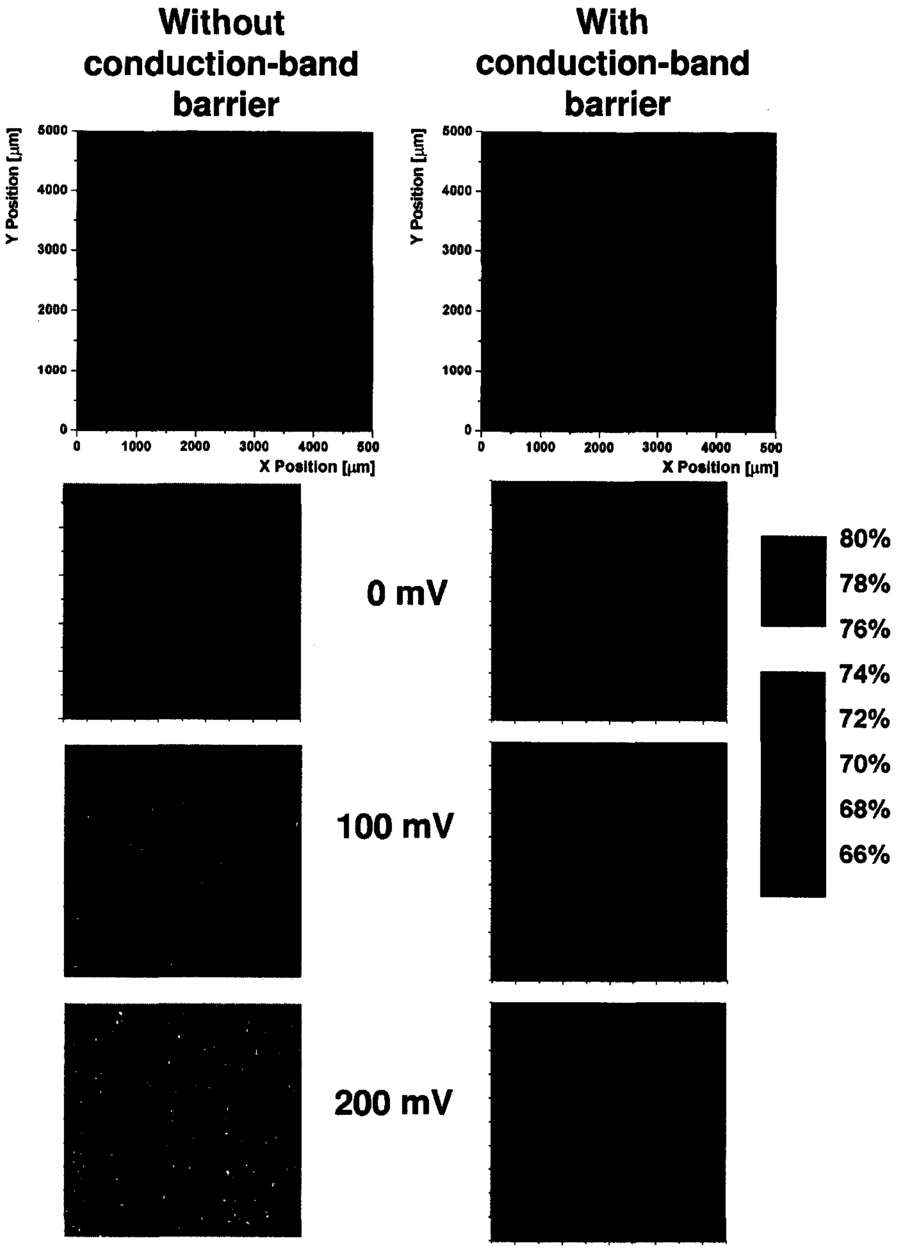

Figure 5.12: LBIC data on the two devices whose J-V curves appear in Figure 5.11. Low-resolution LBIC is shown (top) from the device without (left) and with (right) an electron barrier in the conduction band. Medium resolution data on these devices at 0 mV, 100 mV, and 200 mV in forward bias. These studies suggest that the magnitude of the electron barrier varies over the field of view.

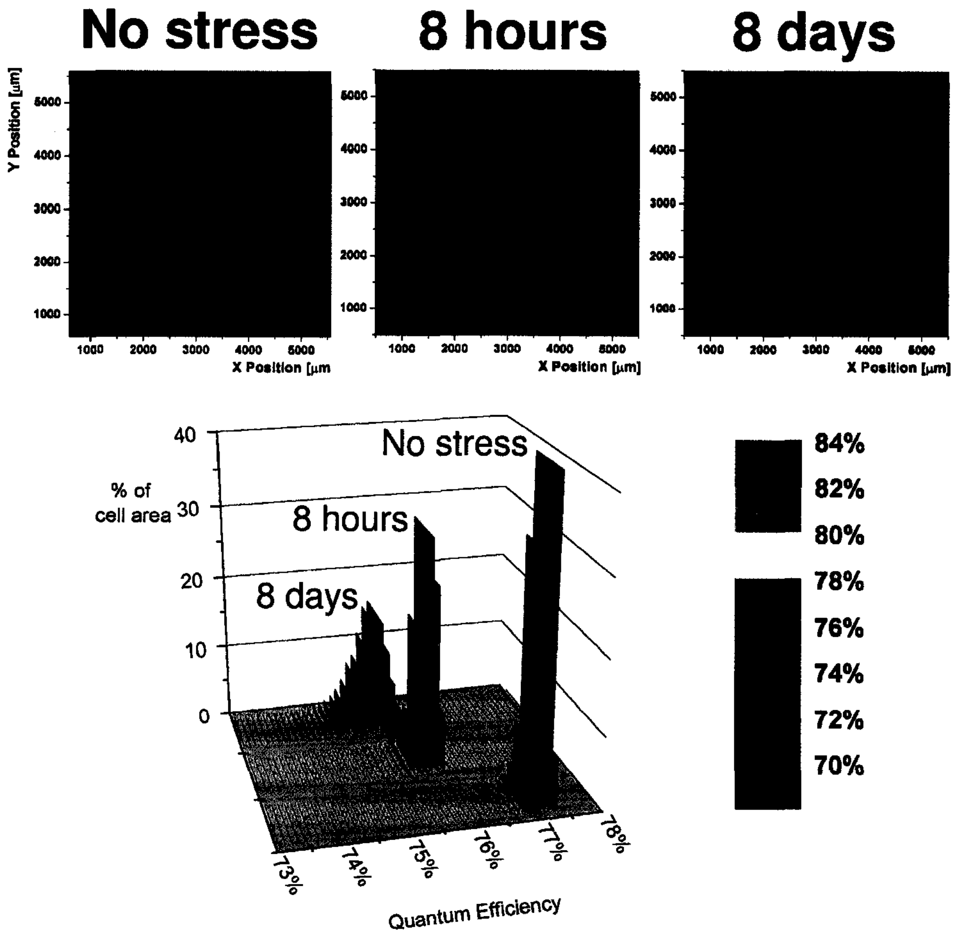

Figure 5.13: LBIC measurements on a CdTe cell show the effects of stress on photocurrent uniformity. Results shown are the initial uniformity (left), and uniformity after 8 hours and 8 days at 100°C under illumination and short-circuit conditions. Histograms show a reduction in overall QE, and a broadening of the QE distribution.

features visible (note the feature at [$x = 1000\ \mu$m, $y = 4500\ \mu$m]). After eight hours of constant high temperature and illumination, the device was re-measured. The histogram has shifted to lower QE and broadened slightly. The feature at [$x = 1000$, $y = 4500$] has become more pronounced and affects a larger area. After eight days of stress, the QE distribution has broadened further, and the device has changed from a tier-I device to a tier-II device. The 2–3 visible features in the initial data each affect a larger area and have been joined by dozens of additional small stress-induced features. In addition to offering insight on a particular mode of solar cell degradation, this study highlights the importance of fabricating cells which are initially uniform, since even small features grow during the lifetime of the cell.

5.6 Patterned Deposition of Cu in Back Contacts

An open question in the CdTe PV community is the role played by copper in the back contact of devices. It is empirically known that Cu is necessary for the formation of a good back contact. Copper is also believed to play a role in the degradation of devices, as Cu tends to diffuse along grain boundaries toward the metallurgical junction of the device. Devices were fabricated at First Solar, LLC as described in [70] and finished by Feldman *et al.* at the Colorado School of Mines (CSM) as described in [71]. These devices were fabricated by vapor-transport deposition and use 3.5–4 μm thick CdTe layers. A patterned deposition of 150-μm diameter Cu dots was used in the back contact formation step to attempt to isolate the effects of Cu from other effects which could cause device-to-device variations. LBIC data was acquired with two wavelengths: 638 nm and 788 nm, as shown in Figure 5.14.

Electroluminescence (EL) measurements were performed at CSM on the same device, and the results are shown in Figure 5.15. In an EL measurement the device is forward biased and a CCD is used to detect radiative recombination. It is seen that EL intensity is highest at the locations where copper was included in the back contact.

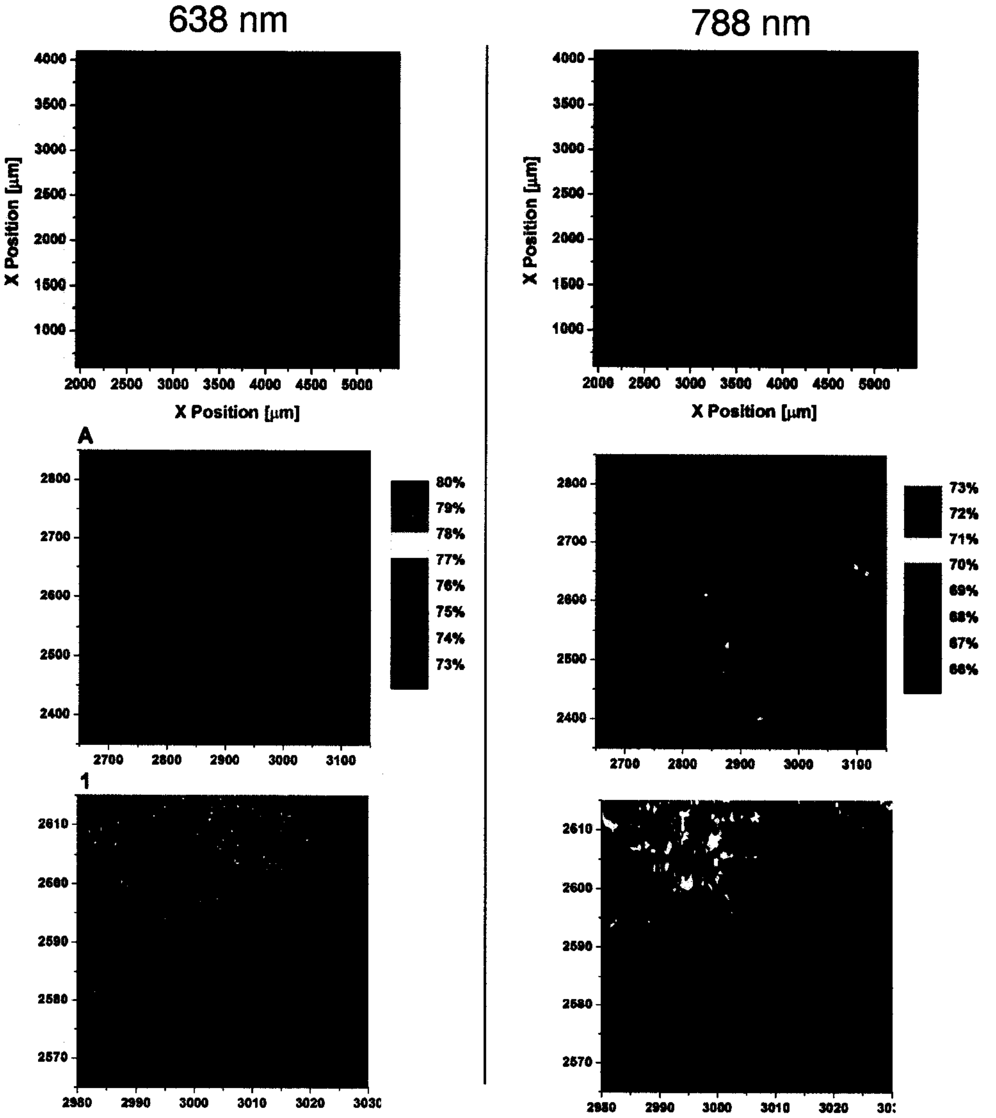

Figure 5.14: LBIC measurements on a CdTe device with patterned deposition of Cu used in the back contact formation process. Laser wavelengths used are 638 nm and 788 nm.

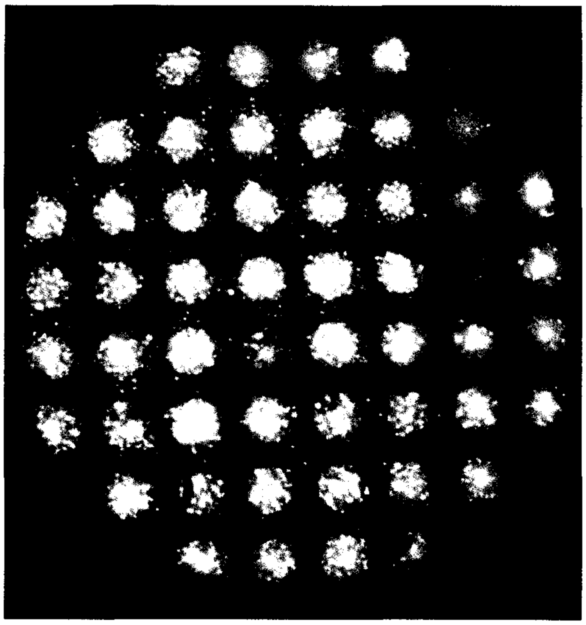

Figure 5.15: Electroluminescence measurements show higher EL signal—higher recombination—at locations where Cu was incorporated into the device. Electroluminescence measurements performed by Scott Feldman at CSM.

In contrast, LBIC measurements show that photocurrent from locations where Cu was used in the back contact is lower than areas where Cu was not used. This suggests that separate from its role in the formation of a back contact, Cu has a detrimental effect on photocurrent. The observed effect was more pronounced for deep-penetrating 788 nm light than for 638 nm light. This is attributed to an increase in density of Cu atoms as depth within the device increases. Photogenerated carriers which are generated deep in the device (*e.g.*, those generated by 788 nm photons) are more likely to interact with a Cu recombination center than those generated near the front of the device.

Through these measurements, a method of PV degradation was observed. Cu was shown to act as a recombination center in CdTe devices, an effect which should become more pronounced as Cu species migrate from the back contact towards the metallurgical junction, such as may occur with stress, recall Section 5.5. Immediately after fabrication of a device (with Cu), a strong gradient in the concentration of Cu exists from back to front in the absorber. As the cell ages and is subject to elevated operating temperatures, Cu atoms migrate towards the front of the cell and their negative effects worsen. Note that the effect of Cu on electron lifetimes deduced from the collection model studies of Section 4.4.3 (where additional Cu in CdTe devices decreased minority-carrier lifetimes) is consistent with this result.

5.7 Back-illumination Through Transparent Back Contacts

5.7.1 Why Use Transparent Back Contacts?

A novel device structure has been proposed and studied for CIGS and CdTe devices [72, 73, 74] which uses a transparent electrical contact at the back of the device as well as at the front. Some of these devices were explored briefly in the previous chapter, where back illumination was shown to be a useful tool for evaluating collection models. These devices could also possibly offer an advantage over traditional devices from a cost minimization point-of-view—one could use reflective surfaces to double the area of illumination—effectively doubling the device power output. In addition to these potential advantages, for the purposes of this dissertation, transparent back contact devices are interesting because they offer the opportunity to isolate diffusion-limited collection from collection within the SCR.

The two materials most often considered for use as a transparent back contact for CdTe solar cells are indium tin oxide (ITO) and ZnTe. The transparent back contact devices discussed in this chapter use ITO, and were fabricated at the Institute for Energy Conversion at the University of Delaware (IEC). In the previous chapter, devices from the Materials Engineering Laboratory at Colorado State University (CSU) were studied with "whole-cell" QE measurements. In this chapter we primarily focus on spatially-resolved QE measurements. The IEC devices have approximately 7-μm-thick CdTe layers, and were fabricated by vapor-transport deposition (VTD).

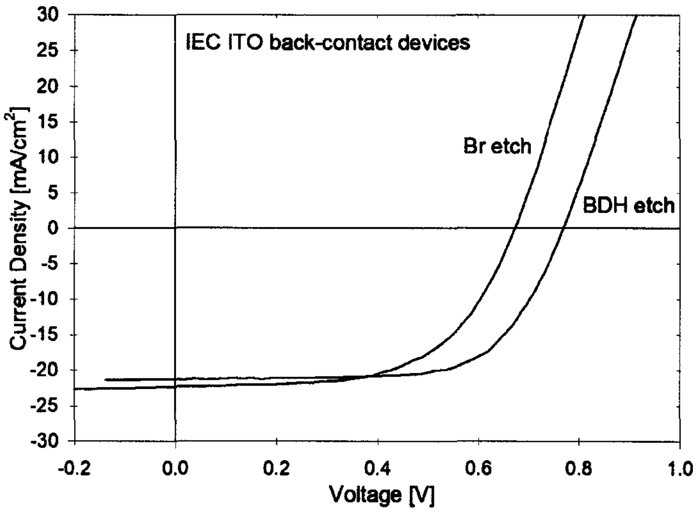

Figure 5.16: Current-voltage curves of representative devices on the two IEC substrates. Devices on the substrate which received the strong BDH etch prior to back contact formation have higher efficiencies, due to higher V_{OC}'s.

5.7.2 Device Fabrication

Two slightly differently processed substrates were supplied by IEC. The difference between the two substrates was the back surface preparation. One substrate received sequential etching in bromine in methanol, dichrol, and hydrazine hydrates (BDH) between CdTe deposition and back contact formation. This strong etch results in an approximately 10-nm-thick Te-rich CdTe layer, before the device is completed with 2 nm Cu, ITO, and a grid. The second substrate received a weaker etch in bromine in methanol (Br) which results in an approximately 1-nm-thick Te-rich CdTe layer. This substrate was finished in the same way as the BDH substrate. As shown in Figure 5.16, the BDH device was better performing, with the difference primarily in the voltage.

CdTe has high bandgap and electron affinity, and therefore it is difficult to form an ohmic contact between CdTe and a metal. Etches are used on the back of the absorber to create a Te-rich layer that can react with Cu (which is deposited next) to form p^+-Cu_2Te. The experimental variable, then, between the IEC devices is the process used for back contact formation. Since the BDH etch results in a thicker Te-rich layer (and a thicker p^+-

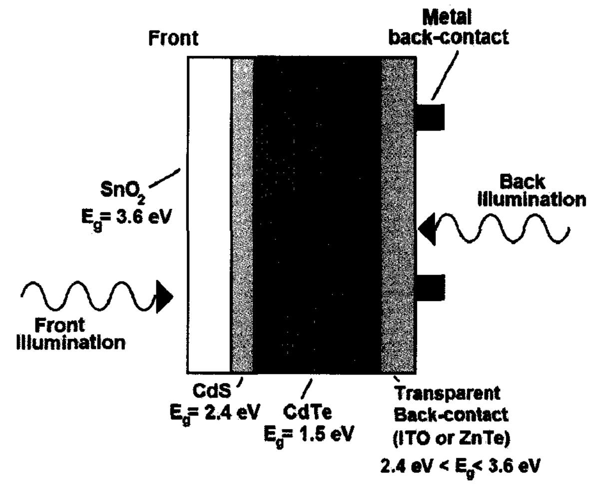

Figure 5.17: Schematic diagram for a transparent back contact CdTe device. Grids are present on the back for current collection. The glass superstrate on the front (left-hand side) is not shown here.

Cu_2Te layer), the back contact barrier interferes less with the front (main-junction) barrier, and voltage is improved relative to the weaker etch, as seen in Figure 5.16. A likely cause of the voltage difference between the two devices is that the poor back contact in the Br-etched device creates a wider *back-barrier* space-charge region (SCR) which overlaps to a greater extent with the front barrier SCR. This lowers the front barrier in the Br-etched device and, consequently, V_{OC}.

Traditional CdTe devices use a thick metallic back contact, so that electrical contact to the back of the device can be made by directly probing the device. The ITO used as the back contact material in these devices is too delicate to directly probe, so these devices are fabricated with a metal in the form of grid fingers for making electrical contact to the back of the device, as shown in Figure 5.17.

These devices were studied with standard QE techniques, and also with the LBIC technique from both the front and the back sides. In the LBIC studies, a range of wavelengths spanning the CdTe bandgap was used. This allowed for investigation of local QE behavior for both strongly absorbed and weakly absorbed photons.

5.7.3 BDH-etched Device

BDH: Front-side LBIC

Measurements with illumination incident on the front side of a device are the standard use of LBIC. Figure 5.18 shows the result of front-side measurements on a 7-μm-thick BDH-etched IEC device (higher voltage in Figure 5.16) with the 638-nm laser. This measurement probes only the front portion of the device, since the penetration depth for this wavelength is about 0.2 μm. For wavelengths between 825 nm and 855 nm, the penetration depth of the illumination increases rapidly from $\sim$ 2 μm to $\sim$ 30 μm. In Figure 5.19, results from the same areas as in Figure 5.18 are shown for a range of wavelengths approaching the CdTe bandgap.

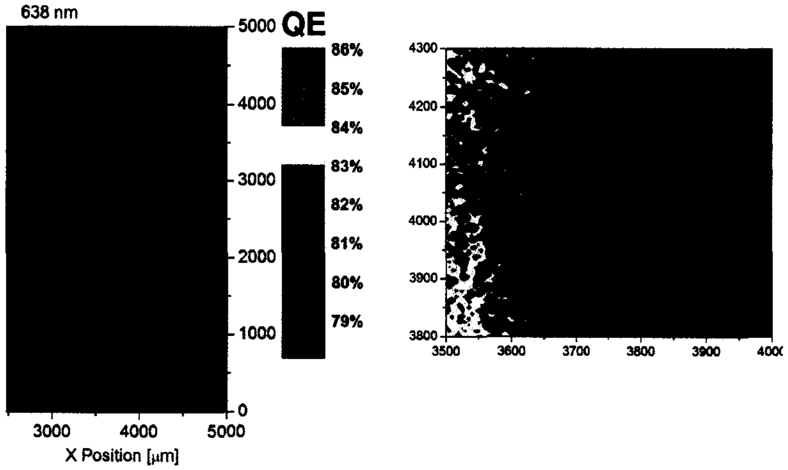

Figure 5.18: Front-side LBIC is shown on a device from IEC with BDH etch. The laser wavelength used is 638 nm, which is absorbed very close to the front of the device. A 1% color scale is used to display the mid-resolution data, so as to accentuate the nonuniformity of the photocurrent. The square region outlined in the left-hand photomap was investigated with a smaller (10 μm) spot, results are shown in the right-hand photomap, which indicates many features 10 μm in diameter.

The near-bandgap light used for the measurements in Figure 5.19 penetrates deep into the device and interacts with the back contact. Note that the magnitude of QE progressively decreases as the wavelength approaches the CdTe bandgap. Back contact features are readily visible in Figure 5.19. In the low-resolution data, an area of increased response covers

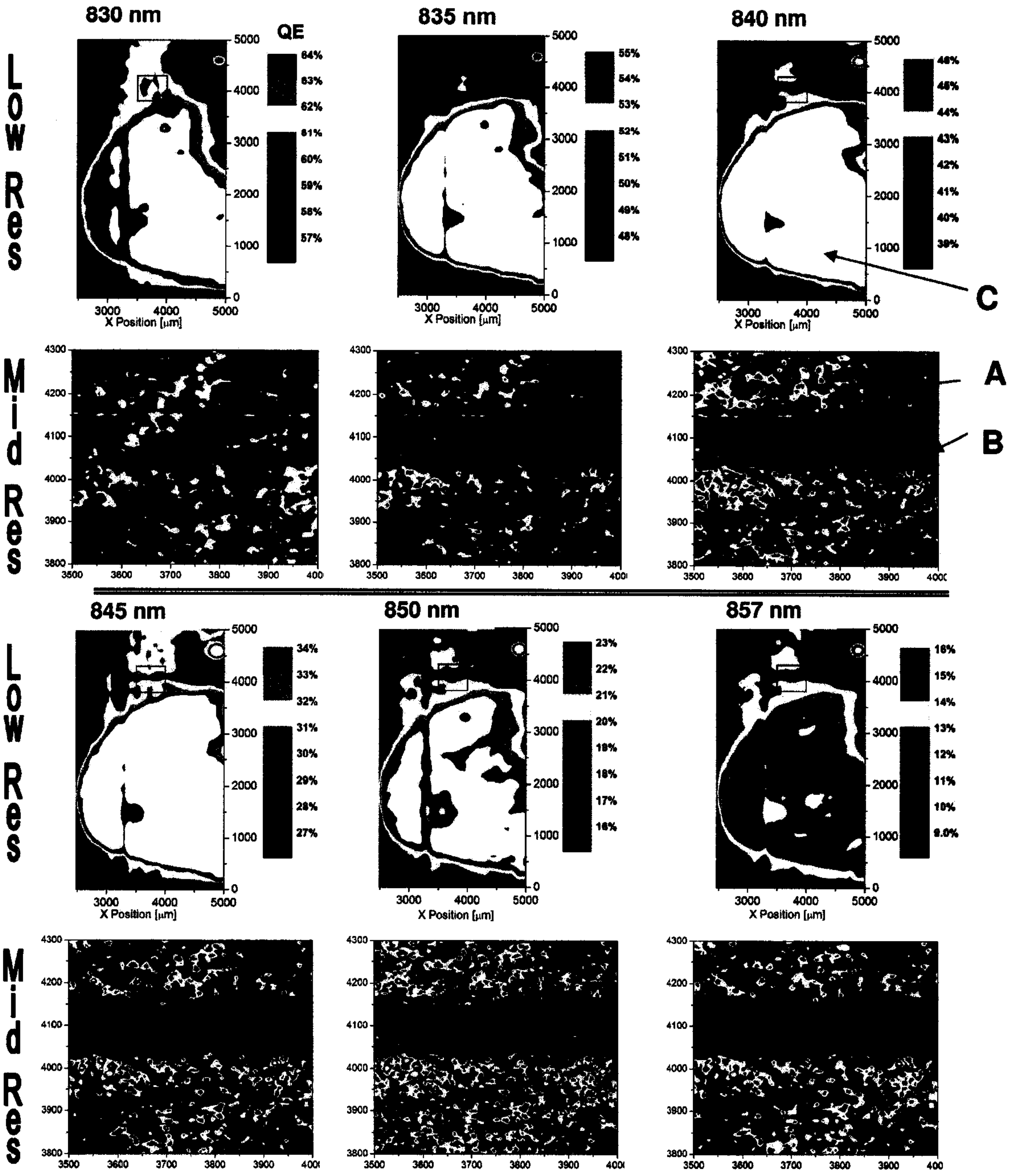

Figure 5.19: Front-side LBIC is shown on a device from IEC with BDH etch. The areas shown here are identical to the areas shown in Figure 5.18. The laser wavelengths used are 830, 835, 840, 845, 850, and 857 nm. These wavelengths penetrate deep into the device and interact with the back-contact. As previously, a 1% color scale is used to display the mid-resolution data, so as to accentuate the nonuniformity of the photocurrent. Although these measurements use front illumination, features at the back contact are apparent. The different conditions present at *A*, *B*, and *C* are discussed in the text.

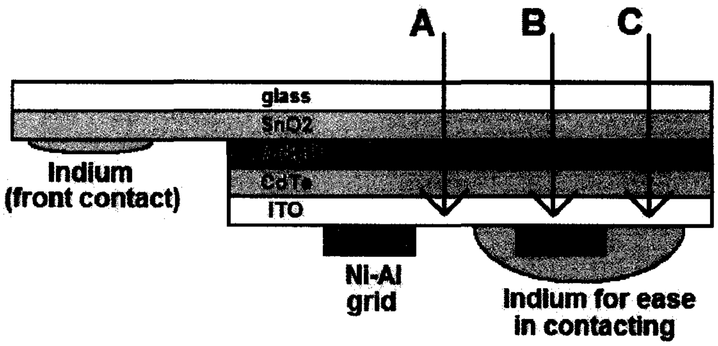

Figure 5.20: Device schematic of an IEC device during LBIC measurement. A pad of indium is used for making electrical contact to the back of the device without damaging the device. Long-wavelength light transmitted through the device encounters three different interface at the back depending on position; A: CdTe/ITO/Air, B: CdTe/ITO/Ni-Al grid, C: CdTe/ITO/Indium.

the bottom two-thirds of the measurement area. In the mid-resolution data, a back-side grid line becomes clearly apparent by 840 nm. Both of these features are explained by considering reflections within the device at the back contact. Figure 5.20 shows a device schematic that explains the differences between the positions labeled *A*, *B*, and *C* in Figure 5.19 for the long-wavelength front-illumination data.

When measuring devices with delicate or difficult-to-contact back contacts such as this device (where tiny grid lines make contacting difficult) a small (5 mm^2) pad of indium metal is used to facilitate electrical contact to the back of the device as shown. For traditional devices, where the back contact material is a metal (opaque), this has no effect on measurements other than to reduce contact resistances—which are parasitic series resistances. In devices with transparent back contacts, photons encounter a position-dependent interface at the back of the device. At position *A* from Figure 5.20, photons which are not absorbed by CdTe encounter first a CdTe/ITO interface where they may be reflected or transmitted, then an ITO/Air interface where they may again be reflected or transmitted. At position *B*, photons encounter first the CdTe/ITO interface, then an ITO/Ni grid interface, which will reflect a different fraction of incident photons back into the device for collection. At position *C*, an ITO/In interface is encountered with still different transmission/reflection properties. These effects are not observed with 638-nm light (Figure 5.18) because those

Table 5.1: Indices of refraction for thin-film CdTe [75], air, ITO [76], and the Ni/Al grid [77] at 830 nm.

Layer	n
CdTe	3.0
Air	1.0
ITO	1.8
Ni (thin film)	~ 2.5

higher-energy photons do not reach the back of the device.

The indices of refraction for relevant materials are shown in Table 5.1. For light incident normally from a medium with refractive index n into a medium with refractive index n', the fraction of intensity reflected is given by

$$R = (\frac{n' - n}{n' + n})^2 \tag{5.1}$$

if the magnetic susceptibilities $\mu \simeq \mu'$ [78]. The photons at positions A, B, and C in Figure 5.20 all see a CdTe/ITO interface, so this interface should play no role in the position dependent LBIC response from the back contact. At position A, however, the ITO/Air interface has reflectivity $R = (\frac{1-1.8}{1+1.8})^2 \simeq 8\%$, while at position B, where photons are incident on the back-side grid finger, the ITO/Ni interface has reflectivity $R = (\frac{2.5-1.8}{2.5+1.8})^2 \simeq 3\%$. Unknown properties of the ITO/Ni interface (such as some incorporation of Ni into the ITO film) may have further reduced reflection from the interface. We should expect then, that front-side QE will be reduced at the position of back-side grid fingers for deep-penetrating photons, since fewer photons will be reflected back into the device. This is easily seen in the mid-resolution data of Figure 5.19. The 830-nm data at top left shows only a small effect over the grid finger since most of these photons do not penetrate all the way through the 7-μm-thick CdTe layer. As the wavelength is increased, reduced collection over a grid line becomes clearly apparent. This effect is somewhat counter-intuitive since one might expect decreased local series resistance near a grid line to improve collection, but for the deep penetrating photons the reflection of photons is apparently much more important.

The same effect is likely to be responsible for the increased collection seen in the lower two-thirds of the low-resolution data. This area corresponds to the location of the indium pad that is used to aid in contacting the back of the device. At these locations, corresponding to position C from Figure 5.20, photons encounter an ITO/In or ITO/Air/In interface and are reflected back into the device, apparently with a much higher reflection probability than at the ITO/Ni interface. Note that this effect is less pronounced for the extremely weakly absorbed photons with $\lambda = 857$ nm, since these photons would require several thicknesses of 7-nm-thick CdTe for full absorption.

BDH: Back-side LBIC

Figure 5.21 shows LBIC data on the back side of the same device discussed in Section 5.7.3. The orientation of the photomaps has changed with respect to the presentation of front-side data, but the two measurements investigated the same general area of the device. The grid lines are visible here as well, this time for the usual reason of grid shading. The grids are not sharply defined because the laser spot size used here is larger than the grid width and step size. On the perimeter of the device, response is greatly increased outside the semiconductor area. This is due to photons which enter the glass through the scribe lines and are reflected to the front of the cell. The increased response then, is due to front-, not back-illumination.

A large circular region of decreased response is seen in the upper right corner of Figure 5.21. Although this feature was located very near to the edge of the area studied with front illumination, there was ‘no sign of it’ in that data.

In Figure 5.22, back-illumination data with near-bandgap wavelengths is given. Figure 4.5 identified some common features present in back-side QE curves. Here we explore only the near-bandgap portion of the QE curve with LBIC. As in whole-cell QE data, LBIC results taken from the back side peak near $\lambda = 830$ nm. Longer wavelengths give less response for the same reason as in front-side QE data—the photon energy is not high enough

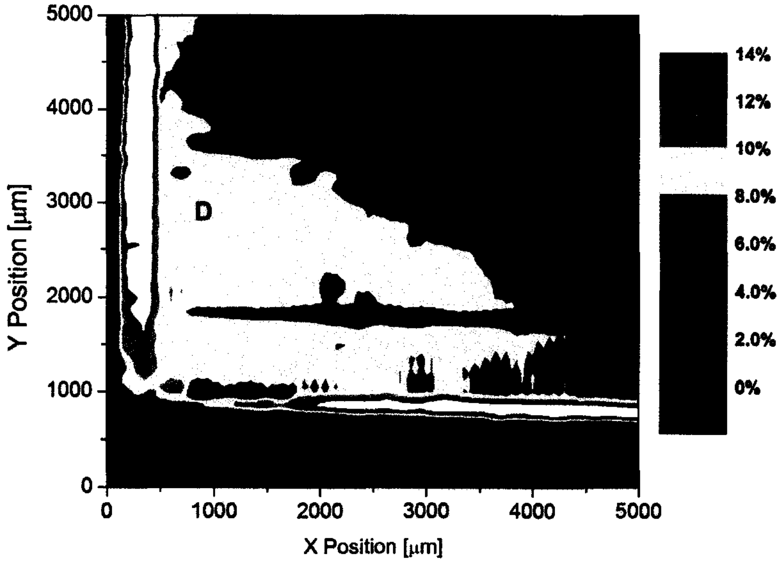

Figure 5.21: Back-side 638-nm LBIC is shown on a device from IEC with BDH etch. The 638-nm photons are absorbed readily by the CdTe, so carriers are generated close to the back surface of the device. These carriers rely on diffusion for collection, resulting in low QE. The areas of high response on the perimeter of the device correspond to scribe lines on the substrate. Some photons enter the glass through the scribe lines and are absorbed at the front of the device, where collection is higher. Note the locations of three points of interest *D*, *E*, and *F*.

to excite electron-hole pairs.

Consider the positions *D*, *E*, and *F* in Figure 5.21. Position *D* is in a well-behaved region of the cell, far from the strong feature at *F*. Position *E* is in the transition region between the well-behaved region and the localized feature, and position *F* is centered on the feature. A plot of local QE at these three positions is shown in Figure 5.23. At position *D*, the peak in the back-side QE is apparently at $\lambda < 830$ nm, with a QE peak height close to 50%. At position *F*, the peak occurs near $\lambda = 830$ nm with peak height less than 40%. Position *E* is clearly an intermediate case. The collection model used in Chapter 4 can explain this effect. If the edge of the space-charge region is farther away from the back contact of the cell, the peak in back-side QE will shift to longer wavelengths (since electrons are more easily collected if they are generated nearer to the space-charge edge), and the peak height

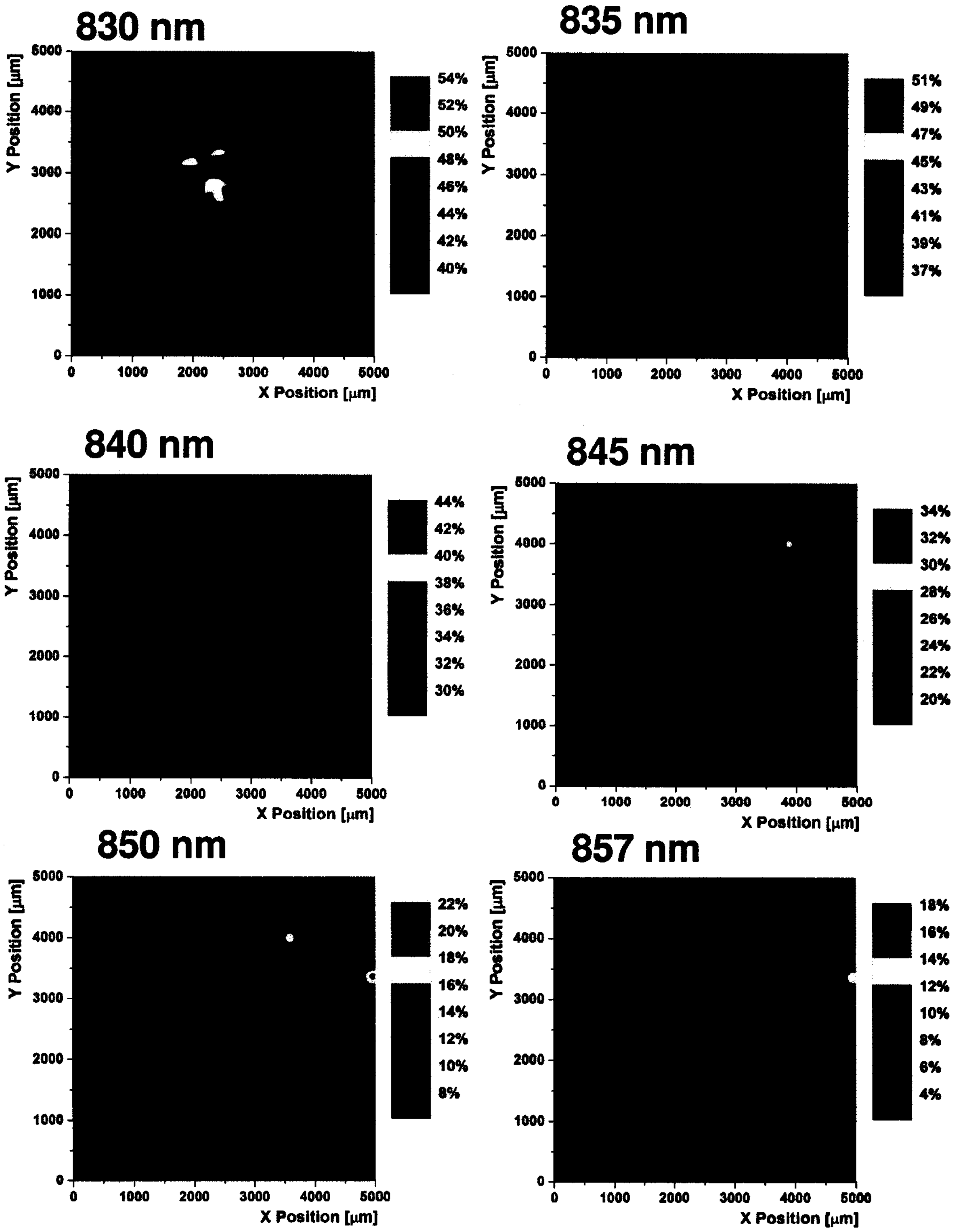

Figure 5.22: Back-side LBIC is shown on a device from IEC with BDH etch, with laser wavelengths 830, 835, 840, 845, 850, and 857 nm. Here grids appear for the usual reason of grid shading.

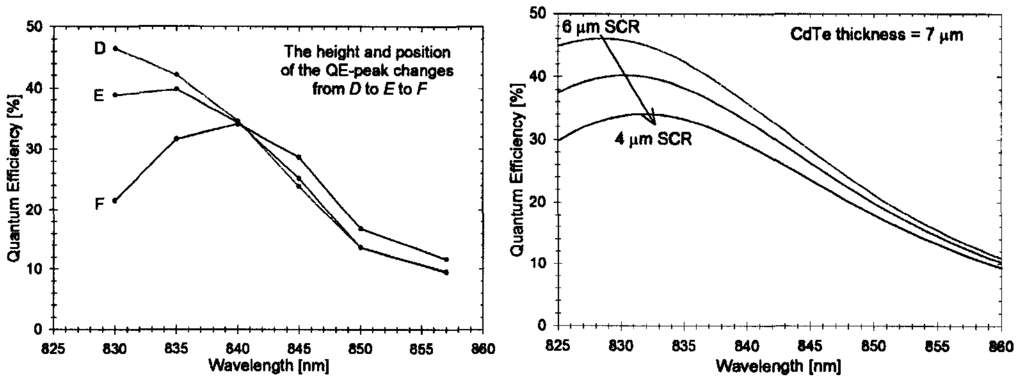

Figure 5.23: Left: Back-side LBIC measurements from the three positions, *D*, *E*, and *F* identified in Figure 5.21. Right: Results from Chapter 4 suggest that a narrowing of the depletion width in the device from position *D* to *E* to *F* could cause the effect at left.

will be reduced. In the Simple Drift model, for a 7-μm-thick absorber, a reduction in the space-charge width from 6 μm to 4 μm reduces the peak height by 10% and increases the peak wavelength by over 5 nm, just as is seen in Figure 5.23.

A possible explanation for the locally changed depletion width comes from examining the back contact formation process. A poor back contact (*i.e.*, one where the p^+-Cu_2Te layer is thin, absent, or not p^+), will have a space-charge region that overlaps with (to personify: is in competition with) the space-charge region from the main junction. This *competition* will push the space-charge edge toward the front of the device and cause the feature seen in the back-side QE data. A possible cause of the locally poor back contact could be a contaminant that inhibited etching. This reduced space-charge width explanation also explains why the feature was not prominent in the front-side data, since the front portion of the device's band structure would be largely unchanged by this effect.

5.7.4 Br-etched Device

Br: Front-side LBIC

Front-side LBIC measurements on an IEC device which received a weak Br etch are shown in Figures 5.24 and 5.25. The Br-etched device has a thinner Te-rich layer, and overall poorer back contact than the BDH-etched device. This device has poorer V_{OC} than the BDH-etched device. The results shown in Figures 5.24 and 5.25 are analogous to the results in Section 5.7.3. As expected, the Br-etched device shows similar back-reflection effects in the front-illuminated data as did the BDH device. The uniformity of the photocurrent response to front-side illumination is similar to that in the BDH-etched device. The BDH-etched devices have slightly higher photocurrent, though the difference is within the range of device-to-device photocurrent variations between devices on the same substrate.

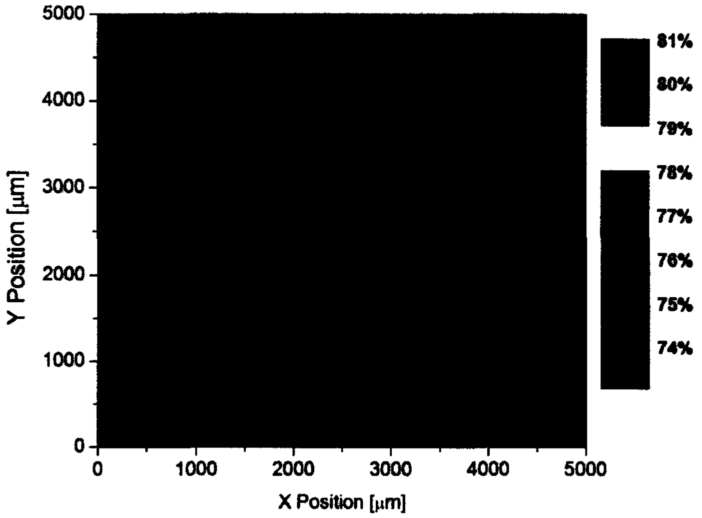

Figure 5.24: Front-side LBIC is shown on a device from IEC with a weak Br etch. The laser wavelength used is 638 nm, which is absorbed very close to the front of the device.

Br: Back-side LBIC

Back-side LBIC data on the Br-etched devices (Figures 5.26 and 5.27) is noticeably less uniform than on the BDH-etched devices, with the exception that on this device there is not a large-scale feature as there is on the BDH device. The thin Te-rich layer that results from the weak Br etch is likely more susceptible to spatial nonuniformity (*i.e.* areas where the etch resulted in no Te-rich layer at all) than the strong BDH etch. The resulting changes

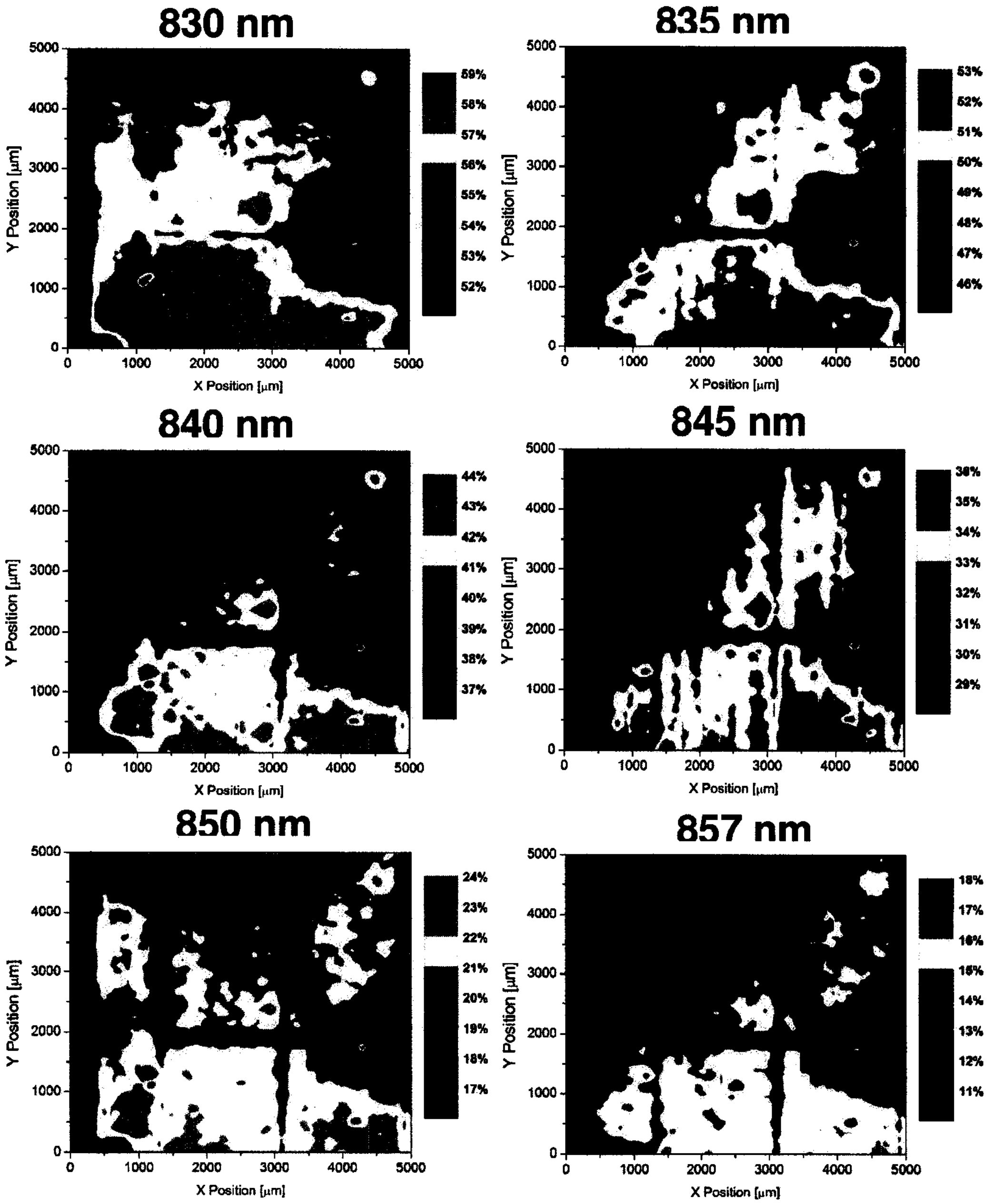

Figure 5.25: Front-side LBIC is shown on a device from IEC with a weak Br etch. The areas shown here are identical to the areas shown in Figure 5.24. Laser wavelengths are 830–857 nm.

in collection efficiency due to spatially nonuniform composition account for the decreased uniformity observed. In Figure 5.26 we once again see high response at the perimeter of the cell, where back-side light transmitted through a scribe line are reflected to the front of the cell, where collection is high.

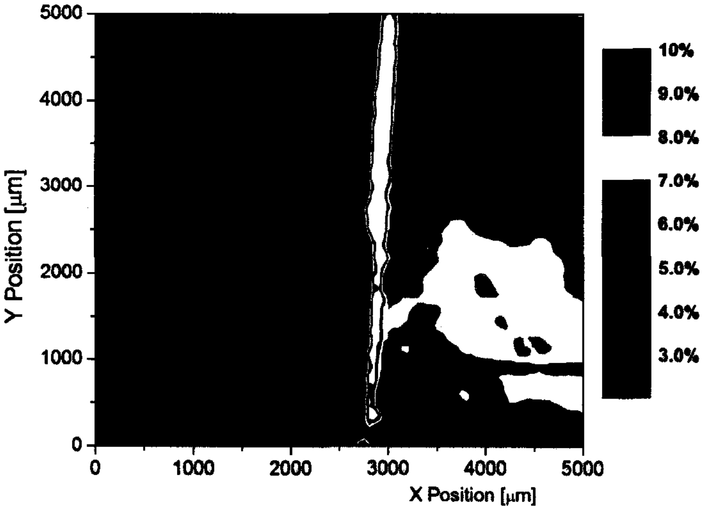

Figure 5.26: Back-side 638-nm LBIC is shown on a device from IEC with a weak Br etch.

5.7.5 Summary of IEC Device Studies

The CdTe devices treated with a strong BDH etch to create a 10-nm-thick Te-rich layer outperformed devices which received a weaker etch in terms of J-V performance and QE uniformity. Open-circuit voltages of the BDH devices were approximately 100 mV higher than the Br-etched devices, resulting in power conversion efficiencies of 10–11%, compared with 8–9% for the Br-etched devices. Little difference was apparent in the uniformity of the devices using front-side illumination, although the unusually thick absorber (7 μm for these devices, whereas 2–4 μm is typical) may have masked nonuniform collection effects which originate at the back contact. This is supported by the observation that with back-side illumination, the lower-voltage Br-etched devices were less uniform

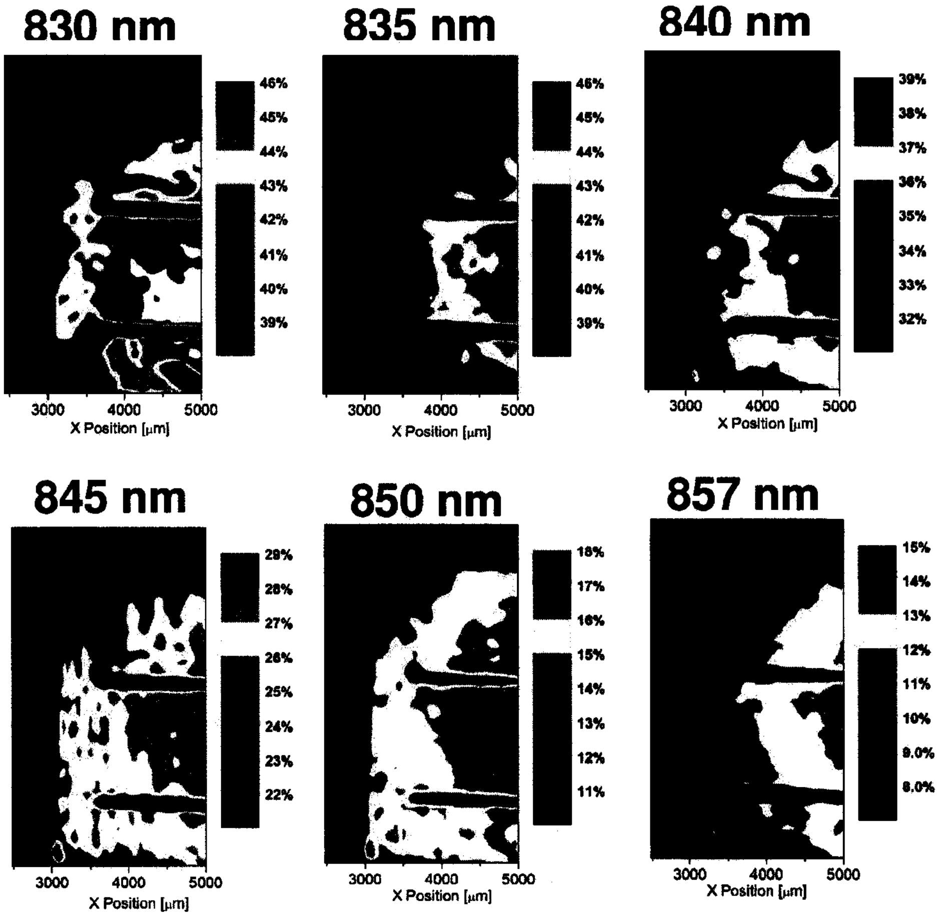

Figure 5.27: Back-side LBIC is shown on a device from IEC with a weak Br etch. Laser wavelengths are 830–857 nm.

than the BDH-etched devices. It is likely that if the absorber were thinned, the same trend would be seen with front-side LBIC. The caveat to the observed trend in uniformity is that a large-scale feature was only observed in the BDH device, though this may be anecdotal and not a characteristic problem of the BDH etch.

5.8 Utility of an LBIC Apparatus for Industrial R & D

The LBIC apparatus described here was designed to extend the state-of-the-art of spatially-resolved QE measurements to very high resolution. The apparatus allows interesting physics to be explored on small-scale samples. The author is often asked about the appropriateness of such an apparatus in an industrial R & D setting. My answer is that spatially-resolved QE is a useful tool and a worthwhile endeavor in an industrial setting, but that the 1 μm resolutions achieved with the apparatus at CSU are likely not worth the cost and effort for most industrial purposes.

My recommendation instead, is an apparatus with spatial resolution the order of 10 μm or 100 μm. In my experience analyzing results obtained with the CSU LBIC device, I estimate that 95% of all interesting results which come from LBIC measurements (and there are many such results), can be achieved using laser spot sizes of 10 μm and greater. The carefully aligned optics and high resolution motion control necessary for diffraction-limited spot sizes add significant cost to an LBIC system, which could be avoided with less stringent resolution requirements. As an alternative setup, one configuration I recommend is the use of a collimated laser beam which is sampled in real time for calibration, much like in the CSU system. The beam is incident at $\sim 45^\circ$ on a mirror which can be tilted on two axes, such that the reflected beam can trace out a cone as the mirror orientation is adjusted. Arbitrarily large areas could be scanned with such a device by placing the sample farther from the movable mirror. Such an apparatus would be advantageous in an industrial setting, since uniformity could be assessed on several area scales, from 1 cm^2 samples up to 1 m^2 modules.

Chapter 6

Conclusions

6.1 Interpretation of Device Physics with QE Measurements

Quantum-efficiency measurements, along with current-voltage measurements, can be tremendously informative about the operation of thin-film solar cells. The traditional use of QE measurements is to identify photon losses—such as those due to CdS absorption or deep penetration—and to determine the absorber bandgap. In this dissertation I have identified various additional information that can be determined with careful QE measurements.

In Chapter 3, it was shown that accurate quantum-efficiency measurements require the cell to be as near to operating conditions as possible. Under non-ideal conditions, such as in the dark, measurements from the CdS region of the spectrum ($\lambda < 500$ nm) and the E_g region of the spectrum (λ near λ_{gap}) are affected by changing space-charge in the CdS window layer due to photoconductivity. At zero bias, the most pronounced effect of light bias is to increase the collection efficiency of long-wavelength photons due to a widening of the space-charge region. In forward bias, forward current can be modulated by an oscillating probe beam absorbed in the CdS, which can cause misleading results. Not only is it important to be aware of these details for measuring accurate QE curves, it is also instructive that when careful attention to the results of nonstandard QE measurements, information about layer properties and band structure is often revealed.

Photocurrent collection models were investigated in Chapter 4. Any effect seen with quantum-efficiency measurements can be attributed to a change in carrier generation or carrier collection (or both). Several collection models were investigated and compared including those used in literature (perfect SCR collection model, and Hecht model) and one which comes from very simple assumptions (Simple Drift model). The Simple Drift model was able to fit a range of experimental data with reasonable values of minority carrier lifetimes together with inputs from experiments (carrier concentration/depletion width, absorber thickness, reflection) and literature (carrier mobilities). Comparisons of model predictions with experimental results showed that increasing amounts of copper in the back contact process is correlated with decreasing minority carrier lifetime, suggesting that copper serves as a recombination center in CdTe absorbers.

The light-beam-induced current apparatus (LBIC) was discussed in Chapter 5. LBIC is uniquely suited to study nonuniform carrier collection in solar cells and can offer a diverse range of information. Three standard "tiers" of uniformity were identified for categorizing LBIC results, based on the width of LBIC histograms. Spatially-resolved reflection measurements were used to identify areas where photocurrent is reduced by optical effects such as nonuniform reflection. The identification of shunts which affect large areas was discussed, including one case where a shunt was intentionally created then removed, and the corresponding LBIC results in the two cases. The role of high-resistivity TCO layers in mitigating nonuniformities was experimentally confirmed. Other applications including bias-dependent measurements and tracking of local degradation with stress were studied. A study of patterned deposition of copper in CdTe back contacts allowed for direct measurement of the effect of Cu on photocurrent. Together with electroluminescence measurements, this re-confirmed the role of copper as a recombination center in CdTe.

Devices with transparent back contacts were also investigated with the LBIC apparatus in Chapter 5. These devices could someday have practical application where reflections can make use of the back surface of a PV module. For the purposes of this dissertation, such devices allow for separation of drift current and diffusion current. Some of these devices were used to investigate the spatial uniformity of space-charge widths with varying back contact processes. A device which received a strong chemical etch as part of the back contact process showed better back-side photocurrent uniformity than a similar device which received a weaker etch. It is likely that in a device with a thinner absorber, these effects would also be observed in front-side photocurrent uniformity measurements. With the aid of the simple-drift collection model from Chapter 4, the cause of one feature was tentatively identified as a weak back contact which pushed the edge of the space-charge region towards the front of the device.

6.2 Implications

The goal of this work has been to further the understanding of thin-film photovoltaics, so that the manufacture of high-quality, low-cost photovoltaic modules is possible. Using standard- and spatially-resolved QE measurements, our understanding of various aspects of these device has been improved. Some conclusions that may be of immediate interest to the PV community include: 1—Photoconductivity in CdS layers affects devices in predictable ways, and when photoconductivity is present, accurate measurements require DC light bias of at least 0.1 sun. 2—Minority-carrier lifetimes may be inferred from collection models which reproduce experimental QE results. Lifetime values determined in this way are consistent with photoluminescence lifetimes in other published results, though not equal since non-radiative recombination dominates in the CdTe devices studied. Results are most reliable when back-side QE data is available as an additional constraint on the model. 3—LBIC measurements can offer a wide range of device-physics information. In particular it was shown here that HRT layers at the front of the device improve device performance by increasing uniformity, and the role of Cu as a recombination center was doubly confirmed. The utility of LBIC for tracking stress-induced degradation was presented. Virtually every electrical variation that can occur in a solar cell device can occur in a nonuniform fashion, and can often be detected with the LBIC apparatus. 4—LBIC measurements on transparent back contact devices indicate that back contact formation steps play an important role in device uniformity, and this is likely to be even more true in devices with thin absorbers.

Bibliography

[1] B. Podobnik. *Global Energy Shifts: Fostering Sustainability in a Turbulent Age*. Temple University Press, Philadelphia, 2006.

[2] P. Berinstein. *Alternative Energy: Facts, Statistics and Issues*. Oryx Press, Westport, CT, 2001.

[3] W. S. Peirce. *Economics of the Energy Industries*. Preager, Westport, CT, second edition, 1996.

[4] Nathan Lewis. Global energy perspective. URL `http://nsl.caltech.edu/energy.html`. accessed 5/13/2007.

[5] Tops in pollution: Great Smoky Mountains. *New York Times*, Sept. 24 2002.

[6] N. Bakalar. Standards: even approved amount of Ozone is found harmful. *New York Times*, Feb. 28 2006.

[7] R. E. Smalley. Future global energy prosperity: the terawatt challenge. *MRS Bulletin*, 30:412–417, 2005.

[8] J. R. Petit, J. Jouzel D. Raynaud, N. Barkov, J. Barnola, I. Basile, M. Benders, J. Chappellaz and. M. Davis, G. Delaygue, M. Delmotte, V. Kotlyakov, M. Legrand, V. Lipenkov, C. Lorius, L. Pépin, C. Ritz, E. Saltzman, and M. Stievenard. Climate and atmospheric history of the past 420,000 years from the Vostok ice core, Antarctica. 399:429–436, 1999.

[9] J. Hansen, L. Nazarenko, R. Ruedy, M. Sato, J. Willis, A. Del Genio, D. Kock, A. Lacis, K. Lo, S. Menon, T. Novakov, J. Perlwitz, G. Russell, G. Schmidt, and N. Tausnev. Earth's energy imbalance: confirmation and implications. *Science*, 308: 1431–1435, June 2005.

[10] T. R. Karl and K. E. Trenberth. Modern global climate change. *Science*, 302:1719–1723, 2003.

[11] Intergovernmental Panel on Climate Change. In *Climate Change 2007: The Physical Science Basis, Summary for policymakers*, 2007.

[12] Raymond Chang. *Essential Chemistry*, chapter 22, page 657. McGraw-Hill, 1996.

[13] D. M. Chapin, C. S. Fuller, and G. L. Pearson. A new silicon p-n junction photocell for converting solar radiation into electrical power. *J. Appl. Phys.*, 25(5):676–676, May 1954.

[14] V. Parente, J. Goldemberg, and R. Zilles. Comments on experience curves for PV modules. *Prog. Photovoltaics*, 10:571–574, 2002.

[15] M. A. Green. Green energy visions: Personal views on the future of photovoltaics. In *Proceedings of the 3rd World Conference of Photovoltaic Energy Conversion*, pages OPL–02, 2003.

[16] A. Shah, P. Torres, R. Tscharner, N. Wyrsch, and H. Keppner. Photovoltaic technology: the case for thin-film solar cells. *Science*, 285:692–698, 1999.

[17] S. Hegedus and A. Luque. *Handbook of photovoltaic science and engineering*, chapter 1, pages 1–43. Wiley, England, 2003.

[18] D. Eaglesham. Scalable, manufacturable, TF-on-glass: from $1.59/W to $1/W. presented at 2007 MRS Spring Meeting, 4/11/2007, San Francisco, CA.

[19] J. Byrne, L. Kurdgelashvili, D. Poponi, and A. Barnett. The potential of solar electric power for meeting future US energy needs: a comparison of projections of solar electric energy generation and Arctic National Wildlife oil production. *Energy Policy*, 32: 289–297, 2004.

[20] J. A. Turner. A realizable renewable energy future. *Science*, 285:687–689, 1999.

[21] S. M. Sze. *Physics of Semiconductor Devices*. Wiley-Interscience, New York, second edition, 2003.

[22] J. F. Hiltner. *Investigation of spatial variations in collection efficiency of solar cells*. PhD thesis, Colorado State University, Spring 2001.

[23] J. F. Hiltner and J. R. Sites. Local photocurrent and resistivity measurements with micron resolution. In *Proceedings of 28th IEEE PVSC*, 2000.

[24] J. F. Hiltner and J. R. Sites. High resolution laser stepping measurements on polycrystalline solar cells. In *Proceedings of the 16th European Photovoltaic Solar Energy Conference*, 2000.

[25] J. Martín, C. Fernández-Lorenzo, J. A. Poce-Fatou, and R. Alcántara. A versatile computer-controlled high-resolution LBIC system. *Prog. Photovoltaics*, 12:283–295, 2004.

[26] J. Carstensen, G. Popkirov, J. Bahr, and H. Föll. CELLO: an advanced LBIC measurement technique for solar cell local characterization. *Sol. Energy Mat. Sol. Cells*, 76:599–611, 2003.

[27] T. E. Furtak, D. C. Canfield, and B. A. Parkinson. Scanning light-spot analysis of the carrier collection in liquid junction solar energy converters. *J. Appl. Phys.*, 51(11): 6018–6021, 1980.

[28] K. Lehovec and A. Fedotowsky. Scanning light spot analysis of faulty solar cells. *Sol. St. Elect.*, 23:565–576, 1980.

[29] P. H. Mauk, H. Tavakolian, and J. R. Sites. Interpretation of thin-film polycrystalline solar cell capacitance. *IEEE Trans. Elect. Devices*, 37:422–427, 1990.

[30] AMPS. *A Manual for AMPS-1D*. The Center for Nanotechnology Education and Utilization, Pennsylvania State University, University Park, PA 16802. URL `http://www.cneu.psu.edu/amps/default.htm`. accessed 5/13/07.

[31] M. Gloeckler, A. L. Fahrenbruch, and J. R. Sites. Numerical modeling of CIGS and CdTe solar cells: setting the baseline. In *Proc. 3rd World Conf. Photovoltaic Energy Conversion*, pages 491–494, 2003.

[32] M. Gloeckler. *Device physics of Cu(In,Ga)Se$_2$ thin-film solar cells*. PhD thesis, Colorado State University, Summer 2005.

[33] X. Wu. High-efficiency polycrystalline CdTe thin-film solar cells. *Solar Energy*, 77: 803–814, 2004.

[34] D. Rose, F. Hasoon, R. Dhere, D. Albin, R. Ribelin, X. Li, Y. Mahathongdy, T. Gessert, and P. Sheldon. Fabrication procedures and process sensitivities for CdS/CdTe solar cells. *Prog. Photovoltaics*, 7:331–340, 1999.

[35] A. D. Compaan. Photovoltaics: clean power for the 21st century. *Sol. Energy Mat. Sol. Cells*, 90:2170–2180, 2006.

[36] A. D. Compaan, A. Gupta, J. Drayton, S-H. Lee, and S. Wang. 14% sputtered thin-film solar cells based on CdTe. *Phys. Stat. Sol.*, 241:779–782, 2004.

[37] B. E. McCandless and K. D. Dobson. Processing options for CdTe thin film solar cells. *Solar Energy*, 77:839–856, 2004.

[38] S. D. Feldman, L. Mansfield, T. R. Ohno, V. Kaydanov, J. D. Beach, and T. Nagle. Non-uniformity mitigation in CdTe solar cells: The effects of high-resistance transparent conducting oxide buffer layers. In *Proc. 31st IEEE Photovoltaic Specialist Conf.*, pages 271–274, 2005.

[39] P. Paulson and V. Dutta. Study of in situ CdCl$_2$ treatment on CSS deposited CdTe films and CdS/CdTe solar cells. *Thin Solid Films*, 370:299–306, 2000.

[40] V. Fthenakis. Life cycle impact analysis of cadmium in CdTe PV production. *Renewable and Sustainable Energy Reviews*, 8:303–334, 2004.

[41] M. Contreras, K. Ramanathan, J. AbuShama, F. Hasoon, D. Young, B. Egaas, and R. Noufi. Diode characteristics in state-of-the-art ZnO/CdS/$CuIn_{1-x}Ga_xSe_2$ solar cells. *Prog. Photovoltaics*, 13:209–216, 2005.

[42] R. Bhattacharya, M. Contreras, B. Egaas, R. Noufi, A. Kanevce, and J. Sites. High efficiency thin-film $CuIn_{1-x}Ga_xSe_2$ photovoltaic cells using a $Cd_{1-x}Zn_xS$ buffer layer. *Appl. Phys. Lett.*, 89:253503, 2006.

[43] H. W. Schock and R. Noufi. CIGS-based solar cells for the next millenium. *Prog. Photovoltaics*, 8:151–160, 2000.

[44] William Shafarman and Lars Stolt. *Handbook of photovoltaic science and engineering*, chapter 13, pages 567–616. Wiley, England, 2003.

[45] D. K. Ferry. *Semiconductor Transport*. Taylor & Francis, New York, 2000.

[46] Keith Emery. *Handbook of photovoltaic science and engineering*, chapter 16, pages 701–752. Wiley, England, 2003.

[47] S. S. Hegedus and W. N. Shafarman. Thin-film solar-cells: device measurement and analysis. *Prog. Photovoltaics*, 12:155–176, 2004.

[48] M. Gloeckler and J. R. Sites. Apparent quantum efficiency effects in CdTe solar cells. *J. Appl. Phys.*, 95:4438–4445, 2004.

[49] M. Köntges, R. Reineke-Koch, P. Nollet, J. Beier, R. Schäffler, and J. Parisi. Light induced changes in the electrical behavior of CdTe and Cu(In,Ga)Se_2 solar cells. *Thin Solid Films*, 403-404:280–286, 2002.

[50] S. Hegedus, D. Ryan, K. Dobson, B. McCandless, and D. Desai. Photoconductive CdS: how does it affect CdTe/Cds solar cell performance? In *Proc. of Mat. Res. Soc. Symp. Proc.*, volume 763, pages 447–452, 2003.

[51] B. McCandless and R. Birkmire. Influence of window and absorber layer processing on device operation in superstrate thin film CdTe solar cells. In *Proc. 28th IEEE Photovoltaic Specialist Conf.*, pages 491–494, 2000.

[52] A. O. Pudov. *Impact of secondary barriers on $CuIn_{1-x}Ga_xSe_2$ solar-cell operation*. PhD thesis, Colorado State University, Spring 2005.

[53] I. L. Eisgruber, J .E. Granata, J. R. Sites, J. Hou, and J. Kessler. Blue-photon modification of nonstandard diode barrier in $CuInSe_2$ solar cells. *Sol. Energy Mat. Sol. Cells*, 53:367–377, 1998.

[54] T. Nakada and M. Mizutani. Improved efficiency of $CuIn_{1-x}Ga_xSe_2$ thin film solar cells with chemically deposited ZnS buffer layers by air-annealing - formation of homojunction by solid phase diffusion-. In *Proc. 28th IEEE Photovoltaic Specialist Conf.*, pages 529–534, 2000.

[55] D. Albin, J. Tuttle, G. Mooney, J. Carapella, A. Duda, A. Mason, and R. Noufi. A study on the optical and microstructural characteristics of quaternary $CuIn_{1-x}Ga_xSe_2$ polycrystalline thin films. In *Proc. 21st IEEE Photovoltaic Specialist Conf.*, pages 562–569, 1990.

[56] T. Myers, S. Edwards, and J. Schetzina. Optical properties of polycrystalline CdTe films. *J. Appl. Phys.*, 52(6):4231–4237, 1981.

[57] S. Miyajima, H. Sakuragi, and M. Matsumoto. Extraction of mean free path of charge carriers in CdZnTe crystals from measured full-energy peaks. *Nucl. Instr. and Meth. in Phys. Res. A*, 485:533–538, 2001.

[58] W. Krühler. Amorphous thin-film solar cells. *Appl. Phys. A*, 53(1):54–61, July 1991.

[59] L. A. Kosyachenko. Problems of efficiency of photoelectric conversion in thin-film CdS/CdTe solar cells. *Semiconductors*, 40:710–727, 2006.

[60] S. Hegedus, D. Desai, and C. Thompson. Voltage dependent photocurrent collection in CdTe/CdS solar cells. *Prog. Photovoltaics*, 2007. In Press.

[61] W. Metzger, D. Albin, D. Levi, P. Sheldon, X. Li, B. Keyes, and R. Ahrenkiel. Time-resolved photoluminescence studies of CdTe solar cells. *J. Appl. Phys.*, 94(5):3549–3555, Sept. 2003.

[62] A. Morales-Acevedo. Can we improve the record efficiency of CdS/CdTe solar cells? *Sol. Energy Mat. Sol. Cells*, 90:2213–2220, 2006.

[63] Y. Bai, J. Phillips, and A. Barnett. Identifying the recombination losses that limit V_{OC} in thin silicon solar cells by bifacial spectral response measurements. In *Proc. 24th IEEE Photovoltaic Specialist Conf.*, pages 1429–1432, 1994.

[64] T. Gessert, A. Mason, P. Sheldon, A. Swartzlander, D. Niles, and T. Coutts. Development of Cu-doped ZnTe as a back-contact interface layer for thin-film CdS/CdTe solar cells. *J. Vac. Sci. Technol.*, 14(3):806–812, May/Jun 1996.

[65] Jun Pan. *Impact of lifetime variations and secondary barriers on CdTe solar-cell performance*. PhD thesis, Colorado State University, Summer 2007.

[66] S. Smith, P. Zhang, T. Gessert, and A. Mascarenhas. Near-field optical beam-induced currents in CdTe/CdS solar cells: Direct measurement of enhanced photoresponse at grain boundaries. *Appl. Phys. Lett.*, 85:3854–3856, 2004.

[67] J. Kestner, S. McElvain, C. Wolden, S. Kelly, T. Ohno, L. Woods, and R. Ribelin. Vapor transport deposition and characterization of polycrystalline CdTe solar absorbers. In *Proc. of Mat. Res. Soc. Symp. Proc.*, volume 763, page B5.22.1, 2003.

[68] A. Kanevce. *Anticipated performance of $Cu(In,Ga)Se_2$ solar cells in the thin-film limit*. PhD thesis, Colorado State University, Fall 2007.

[69] J. R. Sites and T. J. Nagle. In *Proc. 31st IEEE Photovoltaic Specialist Conf.*, pages 199–204, 2005.

[70] R. Harju, V. Karpov, D. Grecu, and G. Dorer. Electron-beam induced degradation in CdTe photovoltaics. *J. Appl. Phys.*, 88(4):1794–1801, August 2000.

[71] S. D. Feldman, R .T. Collins, V. Kaydanov, and T. R. Ohno. Effects of Cu in CdS/CdTe solar cells studied with patterned doping and spatially resolved luminescence. *Appl. Phys. Lett.*, 85(9):1529–1531, 2004.

[72] T. Nakada, Y. Hirabayashi, T. Tokado, D. Ohmori, and T. Mise. Novel device structure for Cu(In,Ga)Se_2 thin film solar cells using transparent conducting oxide back and front contacts. *Solar Energy*, 77:739–747, 2006.

[73] A. Tiwari, G. Khrypunov, F. Kurdzesau, D. Bätzner, A. Romeo, and H. Zogg. CdTe solar cell in a novel configuration. *Prog. Photovoltaics*, 12:33–38, 2004.

[74] D. Desai, S. Hegedus, B. McCandless, and D. Ryan. Transparent ZnTe:Cu contacts for bifacial characterization of CdTe solar cells. In *Proc. of Mat. Res. Soc. Symp. Proc.*, volume 865, pages 405–410, 2005.

[75] D. Schubert, M. Kraus, R. Kenklies, C. Becker, and R. Bicknell-Tassius. Composition and wavelength dependence of the refractive index in $Cd_{1-x}Mn_xTe$. *Appl. Phys. Lett.*, 60(18):2192–2194, May 1992.

[76] S. Laux, N. Kaiser, A. Zöller, R. Götzelmann, H. Lauth, and H. Bernitzki. Room-temperature deposition of indium tin oxide thin films with plasma ion-assisted evaporation. *Thin Solid Films*, 335:1–5, 1998.

[77] P. Johnson and R. Christy. Optical constants of transition metals: Ti, V, Cr, Mn, Fe, Co, Ni, and Pd. *Phys. Rev. B*, 9(12):5056–5070, June 1974.

[78] J. D. Jackson. *Classical Electrodynamics*. John Wiley and Sons, Inc., New York, third edition, 1999.